

GL-TR-90-0058

4

AD-A223 113

Broadband Studies of Seismic Sources at Regional and Telesismic Distances Using Advanced Time Series Analysis Methods

Z. A. Der
M. R. Hirano
K. A. Ziegler
R. H. Shumway

ENSCO, Inc.
Signal Analysis and Systems Division
5400 Port Royal Road
Springfield, Virginia 22151-2388

February 1990

Scientific Report No. 1

APPROVED FOR PUBLIC RELEASE; DISTRIBUTION UNLIMITED

GEOPHYSICS LABORATORY
AIR FORCE SYSTEMS COMMAND
UNITED STATES AIR FORCE
HANSCOM AIR FORCE BASE, MASSACHUSETTS 01731-5000

DTIC
ELECTE
JUN 13 1990
S B D
GA

90 65 12 135

SPONSORED BY
Defense Advanced Research Projects Agency
Nuclear Monitoring Research Office
ARPA ORDER NO 5299

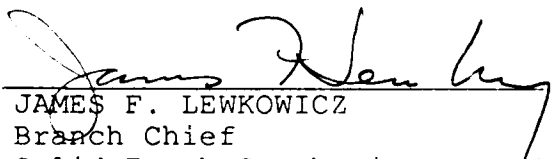
MONITORED BY
Geophysics Laboratory
AFOSR-89-0330

The views and conclusions contained in this document are those of the authors and should not be interpreted as representing the official policies, either expressed or implied, of the Defense Advanced Research Projects Agency or the U.S. Government.

This technical report has been reviewed and is approved for publication.



JAMES F. LEWKOWICZ
Contract Manager
Solid Earth Geophysics Branch
Earth Sciences Division



JAMES F. LEWKOWICZ
Branch Chief
Solid Earth Geophysics Branch
Earth Sciences Division

FOR THE COMMANDER



DONALD H. ECKHARDT, Director
Earth Sciences Division

This report has been reviewed by the ESD Public Affairs Office (PA) and is releasable to the National Technical Information Service (NTIS).

Qualified requestors may obtain additional copies from the Defense Technical Information Center. All others should apply to the National Technical Information Service.

If your address has changed, or if you wish to be removed from the mailing list, or if the addressee is no longer employed by your organization, please notify GL/IMA, Hanscom AFB, MA 01731-5000. This will assist us in maintaining a current mailing list.

Do not return copies of this report unless contractual obligations or notices on a specific document requires that it be returned.

A theoretical statistical framework for a novel methodology for seismic source imaging and inversion was developed. The general algorithms, based on the concepts of F-K analysis using generalizations of both Capon's and Shumway's statistics, were derived for both body waves and surface waves. The associated algorithms were programmed and tested on synthetic data and were shown to be applicable to the problems of decomposition of complex spatial contributions of sources and superpositions of various source types, depth estimation and localization. Tests of these algorithms also provided valuable insights into some of the problems associated with time domain waveform modeling methods, as they are currently being practiced, and ways to eliminate them. Body wave imaging was applied to deconvolved teleseismic P wave data from two Kazakh explosions and showed that they were indeed shallow events. Application of the same technique to the El Golfo earthquake gave a source depth estimate of 14 km, close to but different from the previous estimate of 10 km obtained by other methods. Imaging of surface waves also appears promising, but we had problems with inaccurate or totally wrong absolute timing on some of the data we retrieved from CSS.

The application of the adaptive optimum filtering technique of Shen (1979) to site-equalized teleseismic P waves was shown to be a promising way of enhancing the S/N ratio of such data at seismic arrays. The multi-channel deconvolution method, as applied to teleseismic data, was implemented in an X-windows environment to facilitate further testing and evaluation.

TABLE OF CONTENTS

SECTION	PAGE
Introduction.....	1
Application of Multichannel Deconvolution and Spectral Factorization Concepts to Regional Seismic Array Data.....	5
General Remarks.....	5
Theoretical Considerations.....	6
Events With Identical Green's Functions and Mechanisms.....	10
Events With Identical Sets of Green's Functions and Different Mechanisms.....	12
Events with Differing Green's Functions.....	13
Analyses of Data From Quarry Blasts.....	14
Site Equalization Processing.....	30
Joint Deconvolution of Telesismic and Regional Data.....	37
Broadband Imaging of Seismic Sources Source Inversion.....	41
General Remarks.....	41
Motivation for Frequency Domain Inversion.....	41
Methods for Seismic Imaging.....	48
Applications of the Formalism to Various Seismological Problems.....	50
Simulation Results.....	54
Testing the Consequences of "Average Fit" in the Time Domain..	54
Simulating a Fault.....	61
Separating the Compressional and Double Couple Contributions From Surface Waves.....	63
Data Analyses.....	66
Imaging Selected Nuclear Explosions at the Kazakh Test Site.....	66
Analysis of the August 7, El Golfo Earthquake.....	68
Analyses of Surface Waves From Kazakh Nuclear Explosions.....	74
Adaptive Filtering Studies.....	76
General Remarks.....	76
Teleseismic P Waves From Kazakh Recorded at EKA.....	77
Western Norway Earthquakes Recorded at NORESS.....	82



	DTIC COPY INSPECTED 6
Distribution For GRA&I <input checked="" type="checkbox"/> TAB <input type="checkbox"/> Unannounced <input type="checkbox"/> Classification	Distribution/ Availability Codes Avail and/or Special
Dist A-1	[]

SECTION	PAGE
Future Work.....	85
Conclusions	86
References.....	89
Appendix A. Source Imaging: Statistical Theory.....	A-1
Appendix B. Implementation of Multichannel Deconvolution in the X Windows Environment.....	B-1

INTRODUCTION

Observed seismic signals are superimposed on background noise, their waveforms depend on the characteristics of the source. They are also subject to distortion by various propagation effects, and distortion by the near source and recording site structures. In nuclear monitoring we need to discriminate nuclear explosions from earthquakes, estimate yields and determine other parameters of interest. Clearly, this requires sophisticated processing of seismic signals for reducing the effects of the noise and signal distortions and to extract in some systematic objective fashion the source parameters we need to know.

At the initial stages of the VELA Uniform project (1960-1970) a considerable amount of work was devoted to the application of various statistical time series processing methods to seismic recordings, mostly with the objective to reduce the S/N ratio. Such work soon led to disillusionment, however, because many predictions with regard to the improvements in detectability and the reduction of noise could not be realized. Moreover, the state-of-art of computing was not advanced enough for the large-scale application of such methods, computers were slow, had limited memory and computer time was expensive. Thus, improvements in S/N ratio of the order of 4-6 dB were hardly considered to be worthwhile. It is also evident now that many of the early assumptions applied in designing digital processing schemes were not correct, most notably the assumptions of the perfect signal coherence and the stationary background noise. Such problems lead to the virtual abandonment of sophisticated seismic signal processing methods in nuclear monitoring research, while the development continued in exploration seismology, underwater acoustics and other fields.

In addition to the shortcoming in digital processing schemes for seismic data, it was not possible to model the seismograms and predict the complexities of the signals adequately, or alternatively, to invert the seismograms for source parameters. For the application of advanced signal processing methods, on the other hand, we need realistic and accurate signal models. The algorithms for realistic forward modeling of seismic waveforms were developed more recently, and these require the speed and efficiency of modern computers. The development of such algorithms brought with it an almost totally deterministic approach to seismic modeling and interpretation that often disregarded its inherent limitations and the random nature of data. In treating seismic data the only quasi-statistical methods in routine use today are array beaming and F-K methods. Source inversion consists mostly of direct modeling in which the waveforms of raw recordings are fitted with deterministic models. Limitations of this approach are now quite apparent: modeling is only effective at low frequencies; also the fact that most raw seismic data have a very limited bandwidth led to ambiguities in the inversion for source parameters. It appears that presently there exists no comprehensive and objective theory for broadband source inversion.

It appears that there is a need to merge modern ideas and methods of signal processing, estimation theory, and seismic modeling with the purpose of improving our capability of source identification, location and detection. Development of new approaches to this problem in seismology is timely because of the advances in computer technology and theoretical advancements in other fields. This report presents results and ideas along these lines, and illustrates that such approaches can be fruitful. Since the seismic sources, propagation effects, and signal-to-noise ratios can be best described as complex functions of frequency, and since the inversion problem is linear and thus easier to solve in the frequency domain, most of our processing is done in the frequency domain; although

excursions into the time domain are necessary to interpret deconvolution results and verify some of the basic structures of signals, such as spectral factorability.

The report consists of several sections of varying content. The first major section describes the application and extension of the multi-channel spectral factorization ideas to regional data. First, we describe a test that applies joint deconvolution of regional and teleseismic data. Following this, we present results for regional Pn and Lg arrivals recorded at NORESS. We demonstrate that the concept factorability of signal spectra into site and source response factors is applicable for these phases. Subsequently, we explore some applications of such concepts for event grouping with respect to location, source time functions and refined azimuth estimation. Central to such techniques are the ideas of inter-event and inter-site transfer functions and coherences.

Following the application of spectral factorability, we explore the possibilities of new methods of source inversion, stated in terms of extensions and generalizations, of some known F-K analysis algorithms (*Capon, 1969, Shumway, 1988*). Theoretical background and derivations of such concepts are presented in Appendix A at the end of this report. Specific applications to teleseismic body and surface waves are given in the main body of the text.

In order to test these concepts, fairly extensive simulations were performed on synthetic data. Such testing was also necessary in order to debug the computer codes and explore the stability and inherent limitations of such methods and compare them to other techniques. In doing this, we found that standard time domain waveform modeling methods often do not fit the waveforms closely enough to support the conclusions stated (such as source finiteness effects and source depths estimates accurate to a few kilometers)

and that the information contained in the seismograms in various frequency bands is not effectively and uniformly utilized. Simulations using synthetic data from point sources showed that the imaging concepts we derived are sound. Good source images were also obtained from both body and surface waves. Imaging of simulated faults indicated that the method is suitable for analyzing complex sources.

Following this, we have applied the imaging methods to several Kazakh nuclear explosions with the objective to define the source depth. The results showed that these sources must be located at depths less than 5 km. Applying the same method to the long period P waves from the El Golfo earthquake, gave a mid-crustal, 14 km depth that is not far removed from a previous 10 km estimate. Imaging Kazakh sources with surface waves was less successful, mostly because of demonstrable timing errors in the data sets we acquired.

We conclude the report with some results of optimum filtering of teleseismic data at EKA. These results show that a combination of site-equalization methods with noise-adaptive filtering can be an effective means for increasing the signal-to-noise ratio of both regional and teleseismic data.

Appendix A contains particulars of the imaging theory and Appendix B describes a straightforward implementation of the multi-channel deconvolution method in the X-windows environment. This implementation opens the way for larger scale testing of this technique on teleseismic data.

**APPLICATION OF MULTI-CHANNEL DECONVOLUTION
AND SPECTRAL FACTORIZATION CONCEPTS
TO REGIONAL SEISMIC ARRAY DATA**

GENERAL REMARKS

Obtaining source information from regional recordings is very important in nuclear monitoring because of the concern about small, decoupled nuclear explosions possibly hidden in conventional firing patterns of quarrying operations. Thus far, little progress has been made, and practically no work done, in extracting information from regional waveforms by coherent processing, although spectral expressions of multiple firing sequences have been discovered (*Willis, 1963; Baumgardt and Ziegler, 1988*). The disadvantage of the spectral and cepstral methods is that the phase information in the signals is discarded and that the modulation patterns depend on the similarity in the waveforms from the various individual shots making up the firing sequence. The advantages of such methods are that they are robust and do not otherwise depend on the details of propagation. In this paper we shall discuss the general problem of regional waveform analysis and show how investigating the spectral structure of the data may help in recovering source information, in addition to that obtainable by other methods of analysis.

A general conclusion that may be drawn from attempts of computing synthetic seismograms of regional arrivals such as *Pn*, *Pg*, *Sn*, and *Lg* and comparing them to real data is that it is quite impossible to compute Green's functions with sufficient precision to reproduce such high frequency waveforms in any detail. The reason is that we do not have detailed knowledge of the geological structures that determine the waveforms, and even if we had such knowledge, we simply do not know how to compute synthetic seismograms

for such complicated structures. While it is possible to obtain synthetic seismograms for long period and some standard short period seismograms that match observed waveforms in considerable detail, for regional seismograms the best we can hope for is to match the overall characteristics of wave envelopes and relative phase amplitudes. Details of individual waveforms for various events and recording sites vary so much, even for closely spaced sensors at small arrays, that it is hard to see any visual similarity between the raw waveforms.

Will it ever be possible to derive source related information from the detailed waveforms of regional seismograms if we accept the fact that we shall never know the Green's functions? The answer to this question, based on the work to be presented below, is a qualified yes; although the possibilities seem to be limited due to the extreme variability of regional waveforms with source mechanism and the positions of the sources and receivers.

THEORETICAL CONSIDERATIONS

Before we review the results of our data analyses, it is necessary to describe some expected spectral characteristics of regional seismic arrivals in the light of elementary seismological theory. Let us examine the general spectral structure of seismic arrivals in an arbitrary, heterogeneous anisotropic medium. The problem is completely frequency-separable in the frequency domain as seen by transcribing some known equations (*Aki and Richards, 1980; p. 53*)

$$F_j^i(\omega) = \left[\sum_{p,q} M_{pq}^i(\omega) \cdot G_{pq}^i(\omega) \right] \quad (1)$$

into the frequency domain. M are the components of the moment tensor and G are derivatives of Green's functions (they will be called Green's functions for simplicity in this paper) associated with them. The index i is for the given source and j is for the sensor. In this expression the component index used by *Aki and Richards (1980)*, which is always vertical in this paper, was dropped and the summation over moment tensor components is explicitly indicated, rather than implied by repetition of indices, in order to avoid confusion since other indices will be repeated in some expressions in this paper. This structure is equivalent to a multi-channel filtering problem in which we can consider a seismogram as a result of either of the following equivalent operations:

- a) Filtering the source inputs for each component of a moment tensor with filters corresponding to the Green's functions.
- b) Filtering the Green's functions with the six independent components of the moment tensor.

It is advantageous sometimes to look at the problem using the second interpretation since, as we pointed out above, we shall probably never know the Green's functions and any information we gain from the seismograms should depend only on the coherence relationships among the various seismograms. The relationship (1) is too general to be of much use, unless something is known about the spectral terms and factors in this expression. First of all, we know that the moment tensor components generally have a short time response relative to the length of the regional seismograms, since most seismic sources we consider are of short duration. Moreover, we have to exploit the spectral structures of seismograms to be discussed below and may also invoke the principles of reciprocity before we can derive any useful information from regional waveforms.

It has been shown that for short period teleseismic P waveforms originating from sources in limited regions (such as nuclear test sites) the spectra of individual short period sensors can be adequately described in terms of the factorability condition (*Filson and Frasier, 1972; Der et al, 1987*)

$$F_j^i(\omega) = S^i(\omega) R_j(\omega) \quad (2)$$

where R and S are the site and source factors and F is the Fourier transform of a P wave from the source i and observed at site j . The R are strongly dependent on the azimuths (slowness vectors) of the arrivals; thus, this equation is valid only for limited source regions. We have been successful in estimating the R and S and interpreting S for the teleseismic case based on the assumption that the site factors can be reduced by beaming over sites and that the Green's functions are otherwise simple, and can be enhanced by the same process (*Der et al, 1987*).

Fortunately, Green's functions for teleseismic short period P waves can be described in terms of a few rays, such as P , pP and sP and possibly a few multiple reflections in the crust near the source, all having the same slownesses, and thus the source waveforms can be interpreted in terms of a few phases. This is not generally the case for regional arrivals which contain a large number of multiple reflecting rays in the various crustal layers and involving various values of slownesses, even though a single regional phase tends to be associated with a limited range of slownesses. Therefore, even if we could separate the source and site terms, they could not be interpreted simply; for example, " pP " would have different delays for the various rays. Alternatively, considering the regional arrivals as complex superpositions of high frequency higher normal mode wavetrains, does not allow easy interpretation in terms of source characteristics.

The factorability condition given above suggests a more useful form for the structures of regional seismograms as recorded at arrays:

$$F_j^i(\omega) = \left[\sum_{p,q} M_{pq}^i(\omega) G_{pq}^i(\omega) \right] R_j(\omega) \quad (3)$$

In this expression we have factored the seismogram into spectral factors consisting of the moment tensor spectra, factors G appropriate to the source region location and source mechanism and finally, the site factors R that depend only on the type of wave we are analyzing and the sensor location.

The rest of this paper will be devoted to the examination of the properties of such factors and testing of the validities of relationships of this form for various types of regional data. The form of relationships given above includes the simple factorability Equation (2) as a special case. We must point out that despite the fact that factoring matrices of seismograms works for array recordings of teleseismic signals (*Filson and Frasier, 1972*), there is no reason to believe *a priori* that such factorizations and associated methodologies will work for regional phases which are very complex superpositions of rays or modes, depending on one's preferred way of interpreting them. Any such factorization must be tested and verified by observation prior to any attempts to use them in data processing schemes.

We use the term "coherent processing" in this paper for techniques that exploit the generalized factorability condition as defined above. This is somewhat different from the usual definition coherent processing techniques, such as beaming and F-K analyses routinely applied to regional signals at seismic arrays (*Mykkeltveit et al, 1983; Ingate et al, 1985; Kvaerna and Mykkeltveit, 1986*), which basically depend on the assumption of

complete signal similarity. These processes and the regional array layouts were optimized for signals coming from arbitrary directions using the concept of averaged signal coherences vs sensor distances and are applied only at inter-sensor distances and frequencies where the site effects can be neglected. However, if they satisfy equations of the forms (1) and (2), regional signals across a regional array are much more "coherent," in a more general sense, if we analyze regional arrivals from limited source regions. Let us consider now a few special cases of Equation (2):

Events With Identical Green's Functions and Mechanisms

This is the most commonly studied case, and numerous simulations of spectral modulations due to various spatio-temporal patterns of ripple-firing implicitly assume the similarity of single shots. At a given regional array far removed from the source region, the seismograms at the individual sensors can be written as

$$F_j^i(\omega) = s^i(\omega) H_j(\omega) \quad (4)$$

where the $s(\omega)$ are the source functions for a given event and the $H(\omega)$ are common combinations of the products of moment tensors and Green's functions for all events. A commonly observed phenomenon for numerous shots is that the spectral modulation is the same for all regional arrivals (*Baumgardt and Ziegler, 1988*) even as seen at several regional arrays. This implies a purely temporal modulation, such as implied above, without any spatial structure for the source. Scenarios involving combined temporal-spatial shot configurations of shots can easily be simulated and are actually being applied for vibration control in quarrying operations (*Anderson and Stump, 1989*).

Equation (4) above implies that the waveforms of events conforming with this model will be *coherent* at common sensors of an array. Thus, we can compute the inter-event coherence

$$C = \frac{|P_{ij}|}{\sqrt{P_{ii} P_{jj}}} \quad (5)$$

between two events which should have a high value in the case of low background noise. Central to this idea is the estimation procedure for the power spectral components P . These must be computed by some smoothing procedure such as smoothing the dot products of the signal Fourier transforms denoted as vectors f such that

$$P_{ij}(\omega) = \sum_s \overline{f_i(\omega) f_j^*(\omega)} \quad (6)$$

where the overbar denotes spectral smoothing, the star denotes complex conjugation and the summing of smoothed products is performed over sensors. Smoothing can be accomplished in various ways: by actually smoothing the spectra, by averaging over shorter time windows, or some combination of the two. In our case, we use the combination of spectral smoothing and averaging over array sites. The equivalent time-bandwidth product (TBWP) of the result can be computed by multiplying together the spectral averaging bandwidth B , the total time length T of the data used for each array site and the number of array sites N . In any coherence measurement some decision must be made concerning the bandwidth to be used. High TBWP implies high stability of the coherence results; with a given amount of data this can be traded off against the resolution in spectral detail (*Bendat and Piersol, 1966; Shumway, 1988*). In the case discussed here we can assume that the waveform differences are associated with different effective source

functions, i.e., firing sequences. These normally have very short time durations. Generally, the amount of smoothing that can be applied in coherence calculations depends on the time length of the impulse response of the transfer function between the two time series. As a rule of thumb, one can smooth over a bandwidth of $1/T_i$ where T_i is the duration of such an impulse response. This implies that heavy spectral smoothing may be applied in the calculation of C above if the differences in waveforms are mostly due to different firing sequences. For further discussions of the particulars of coherence calculations we refer the reader to *Shumway (1988, pages 70-73)*.

Alternatively, this form of inter-relationship implies the existence of a transfer function that can transform events one from the other with a filter of relatively short impulse response. This does not imply waveform similarity, however, although coherence and waveform similarity are often mistakenly interchangeable.

Events With Identical Sets of Green's Functions and Different Mechanisms

In such cases, the waveforms of individual events generally will not be coherent in the sense of Equation (5), and the spectra of the superpositions of individual shots with different mechanisms will not be modulated in any easily predictable fashion. A possible scenario of such a situation in quarry blasting is a mix of shots, some of which may be applied to a vertical rock face (shear source) and some buried under a horizontal surface, with both kinds of shots being close to the surface at roughly the same depth.

Nevertheless, as long as the six Green's functions are common to a set of events, any seven will be coherent if the multiple coherence is computed for them, where we may test the possibility of reconstructing the i -th time series from the rest (*Bendat and Piersol*,

1966). We believe that this is a worst case scenario, since some of the independent G will not contribute significantly to the waveforms, and some may correlate well; thus, only a few may be important. In such cases, multiple coherences with lesser numbers of events may attain values significantly different from zero. No matter how complex the source mechanisms may be, it will be possible to "calibrate" parts of a quarry with a small number of events, and the high multiple coherences will identify all subsequent events in that quarry. In this study we shall not present any multiple coherence results.

Events With Differing Green's Functions

This is analogous to testing outputs of several different systems with independent random inputs for coherence, where most of these should test as not being significantly different from zero. This case covers all events with different depths and at different locations. If all S s are different, then none of the single and multiple coherences between that event and the events at a "calibrated" quarry will be high. This may be the case for events at a quarry and a hidden decoupled nuclear explosion at a significantly greater depth or an earthquake near a quarry. The lack of coherence could be used as a criterion for such events. Given the fact that decoupled nuclear explosions have to be buried deeper than conventional explosives in standard quarrying procedures, and that the effective mechanisms for the two types of events will no doubt be different, it does not seem to be very easy to mix the two types of explosions in order to hide testing that could not be revealed by some kind of coherence analysis.

ANALYSES OF DATA FROM QUARRY BLASTS

Our data comes from NORESS recordings of events, listed in Table I, identified as quarry blasts at the Titania mine and two Estonian mines named E1 and E4. We have also looked at one event at the Blasjo dam site. We do not know about the location accuracy of these events or the reasons, other than location, for their association with any particular mine. The locations of these events are shown in Figure 1.

In order to apply any of the ideas above, we must first verify the applicability of the factorability condition for any data set. We have applied the multi-channel deconvolution technique described by *Shumway and Der (1985)* and *Der et al (1987)* to two data sets: the *Pn* arrivals from this group of Titania mine blasts and the *Lg* arrivals from a set of mine blasts in Estonia at mine E4.

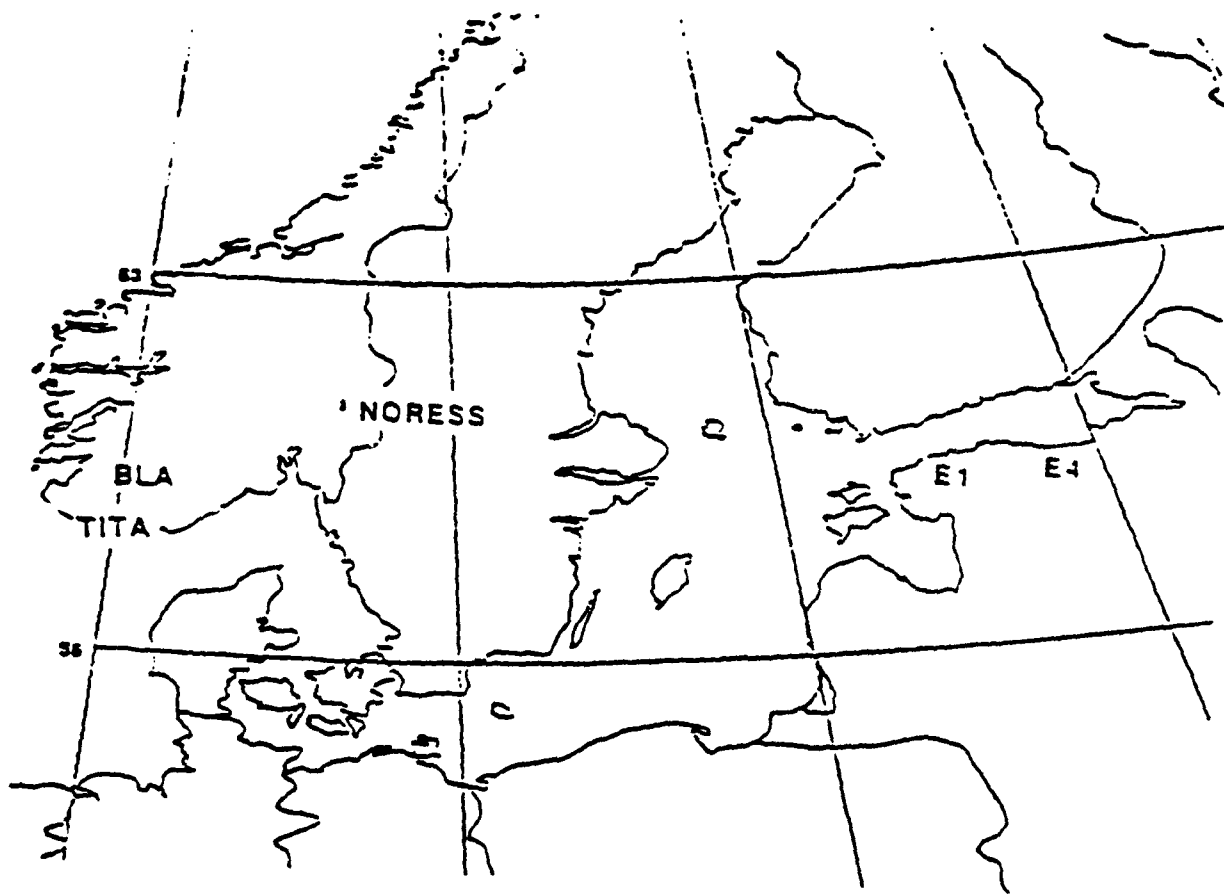


Figure 1. Map of Scandinavia with the location of NORESS and the mines studied.

Table I - LIST OF "TITANIA" AND "ESTONIA" EVENTS

Event	Date	Origin Time	Latitude	Longitude	Magnitude
Titania 1	14 Feb 86	14:13:24.9	58.3	6.4	2.7
Titania 2	14 Feb 86*	17:54:10.6	58.3	6.4	2.3
Titania 3	07 Jan 86	14:14:28.9	58.3	6.4	2.2
Titania 4	17 Jan 86#	14:11:01.5	58.3	6.4	2.7
E4-1	19 Jan 88	11:55:35.0	59.3	27.2	2.5
E4-2	20 Jan 88	12:23:06.0	59.3	27.2	2.5
E4-3	21 Jan 88	11:25:30.0	59.3	27.2	2.4
E4-4	26 Jan 88	09:55:37.0	59.3	27.2	2.4
E4-1	19 Jan 88	11:50:50.0	59.3	24.4	2.5
E4-2	21 Jan 88	12:53:23.0	59.3	24.4	2.2

* Probably removed from or not at the same part of quarry.

Reference event (unmodulated).

Starting with the Pn data from the Titania mine, let us assume initially that all these events had the same source mechanism and/or location and test the idea that the differences in waveforms are totally attributable to differences in firing sequences, i.e., the factors S are common for all the events. Inspecting the spectra of mine blasts from the Titania mine in Norway at NORESS, it can be observed that some have strongly modulated spectra, while some others have quite smooth spectra (Figure 2) for all phases, Pn , Pg , Sn and Lg . This points to a common, *temporal* modulation for each event, rather than to a pattern imposed by the spatial configuration of charges (and possibly also combined with some temporal sequence of explosions) since in the latter case we should see different modulation patterns for the various regional phases which possess notably different phase velocities. Although the lack of modulation does not rule out some very complex spatio-temporal modulation patterns of the source (although these must be quite unlikely), such that the

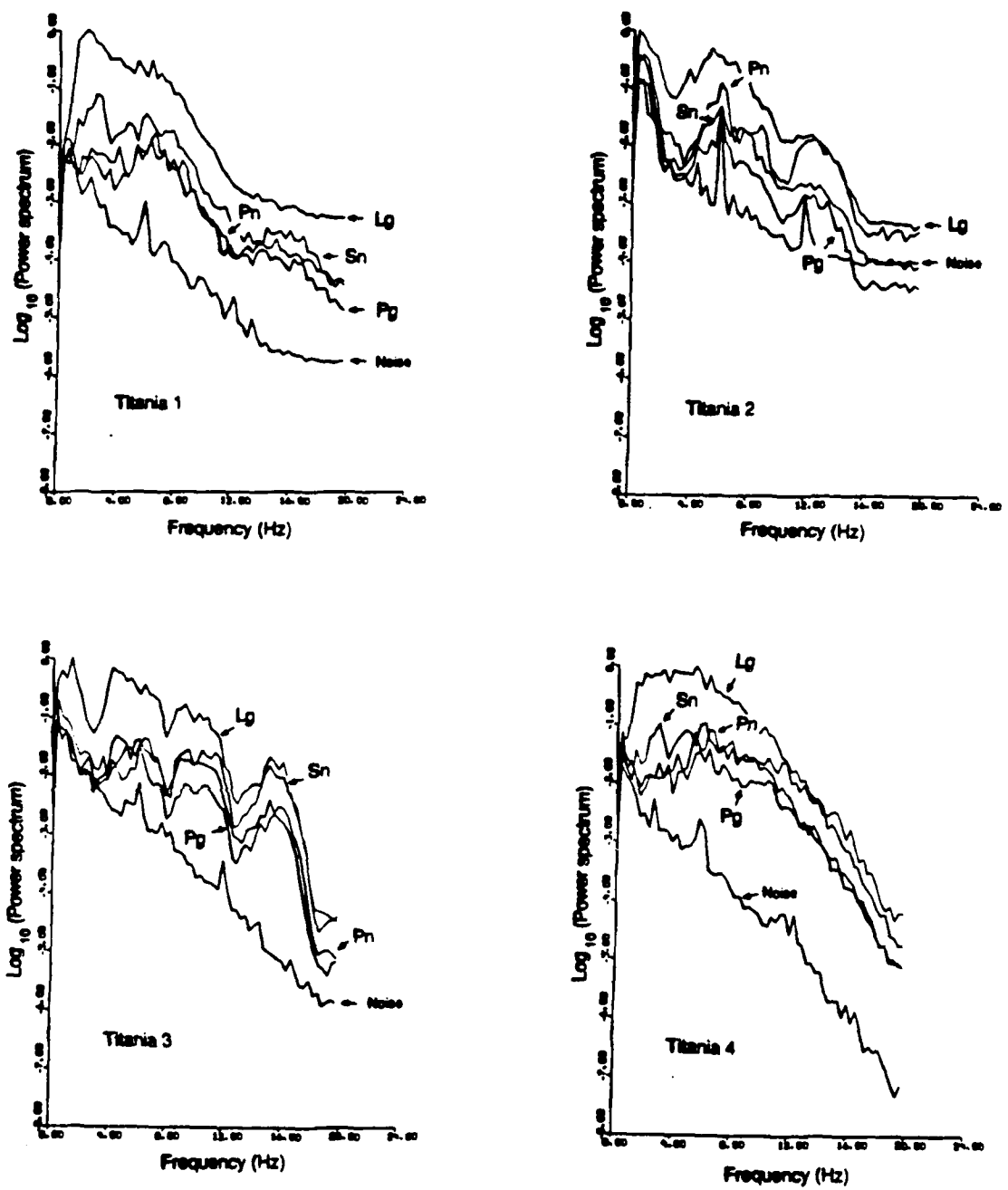


Figure 2. Spectra for various regional arrivals from the titania mine as recorded at NORESS. Event Titania 4 shows no evidence of spectral modulation.

spectral manifestations of it are suppressed, it is reasonable to assume that the spectrally unmodulated quarry blasts have simple impulsive source time functions or very small delays while the modulated ones have been ripple-fired. The *Lg* phases of the Estonia mine blasts are somewhat noisy and the S/N ratio is only good below 4 Hz (Figures 3 and 4).

The decomposition of data into source and site factors is not totally unique (*see Der, 1987*), but by successfully reconstructing the complete set of original waveforms from the much smaller set of estimated source and site spectral factors, we verified that the data has the spectral structure described by Equation (2). Figures 5 and 6 show some representative examples of these reconstructions, all of which are of similar quality within each set. Typically, the correlation coefficients between the pairs of original and reconstructed traces were near or above 0.8, which is not as good as in the teleseismic case, but still respectable considering the high signal frequencies we utilize here. Note that the waveforms are quite different at the various sensors for the same event and for the various events at the same sensors. Joint deconvolution of the Titania events and the Blasjo event did not result in acceptable reconstructions, showing that an azimuth difference of 10° is too large for using the same site factors. In all the work we present in this paper we have used 12 sensors of NORESS roughly evenly distributed over the area of the array.

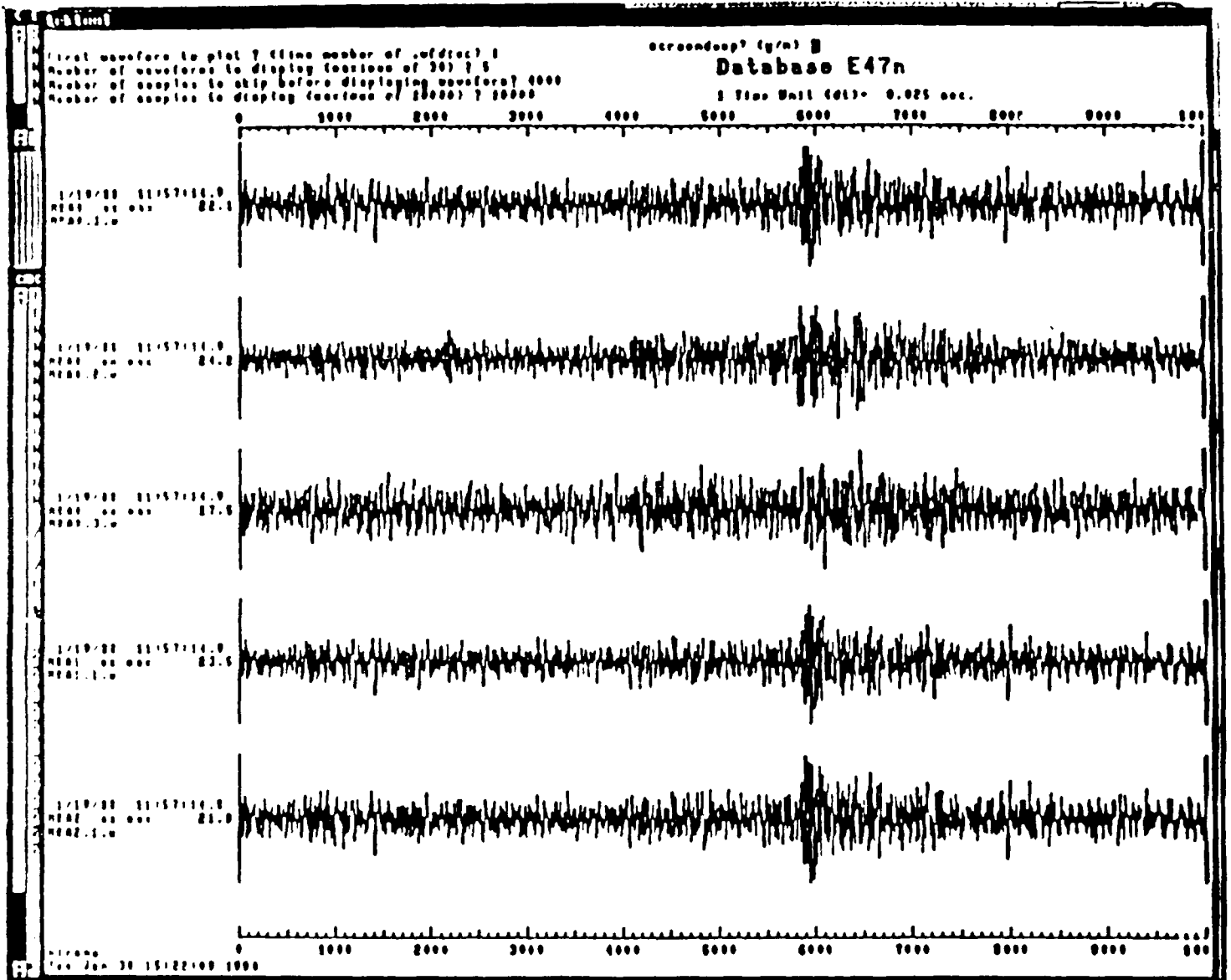
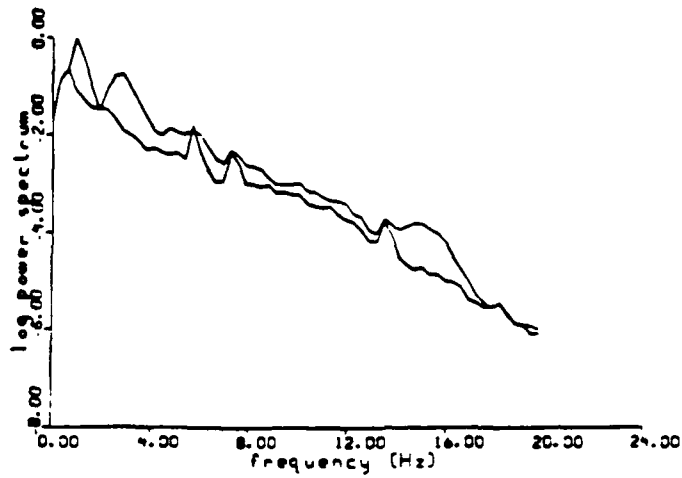


Figure 3. A representative example of an Estonia mine explosion recording. While the Lg phases are well above the noise, the rest of the phases are buried in the noise.

Lg spectrum- Estonia mine blast E47n



Lg spectrum- Estonia mine blast E49n

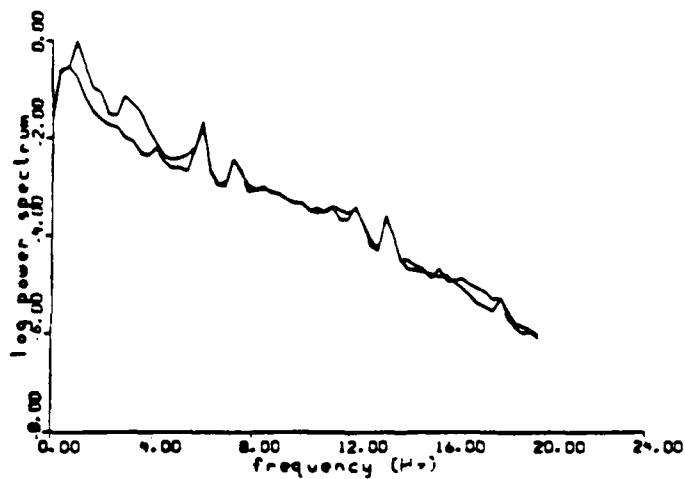
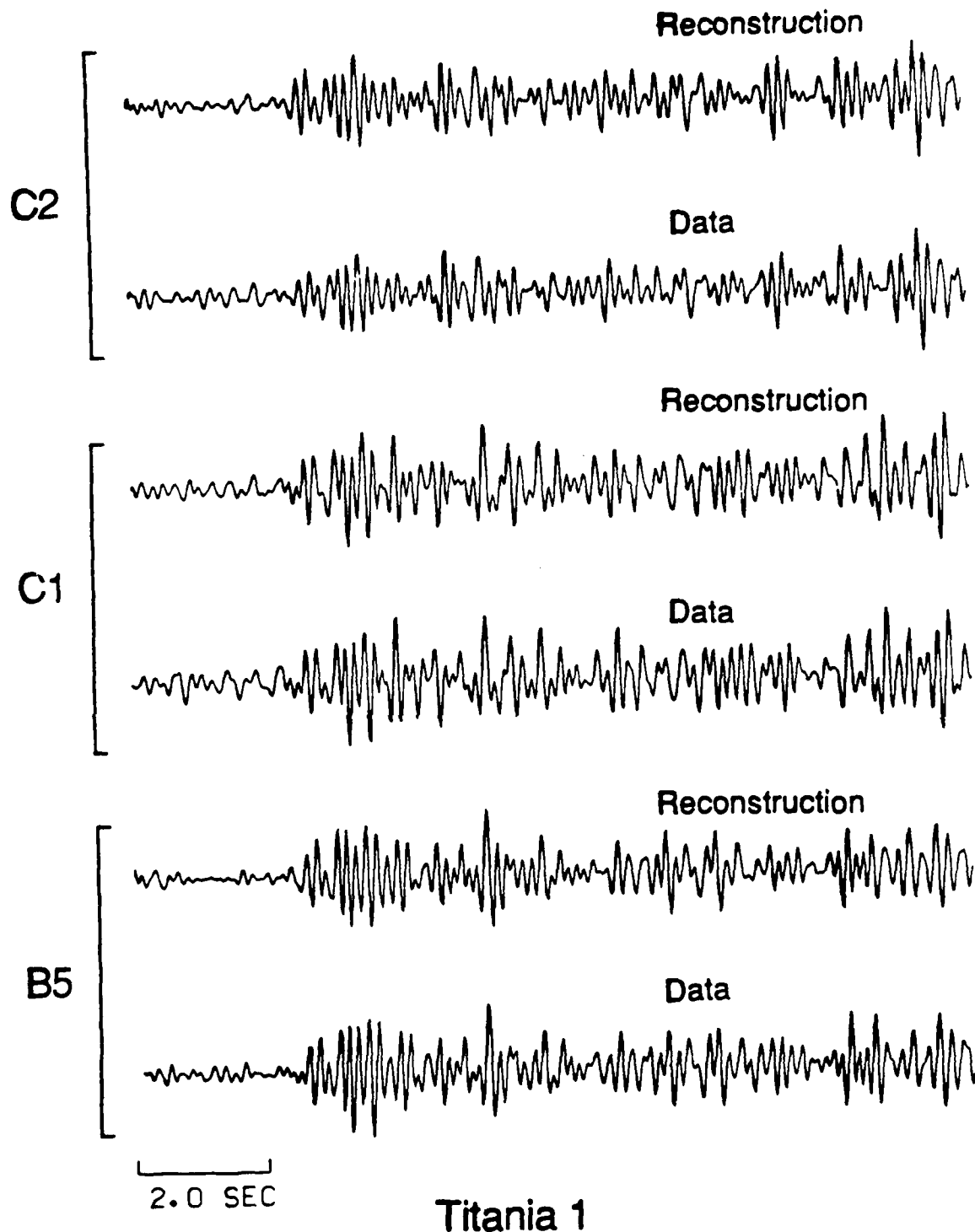
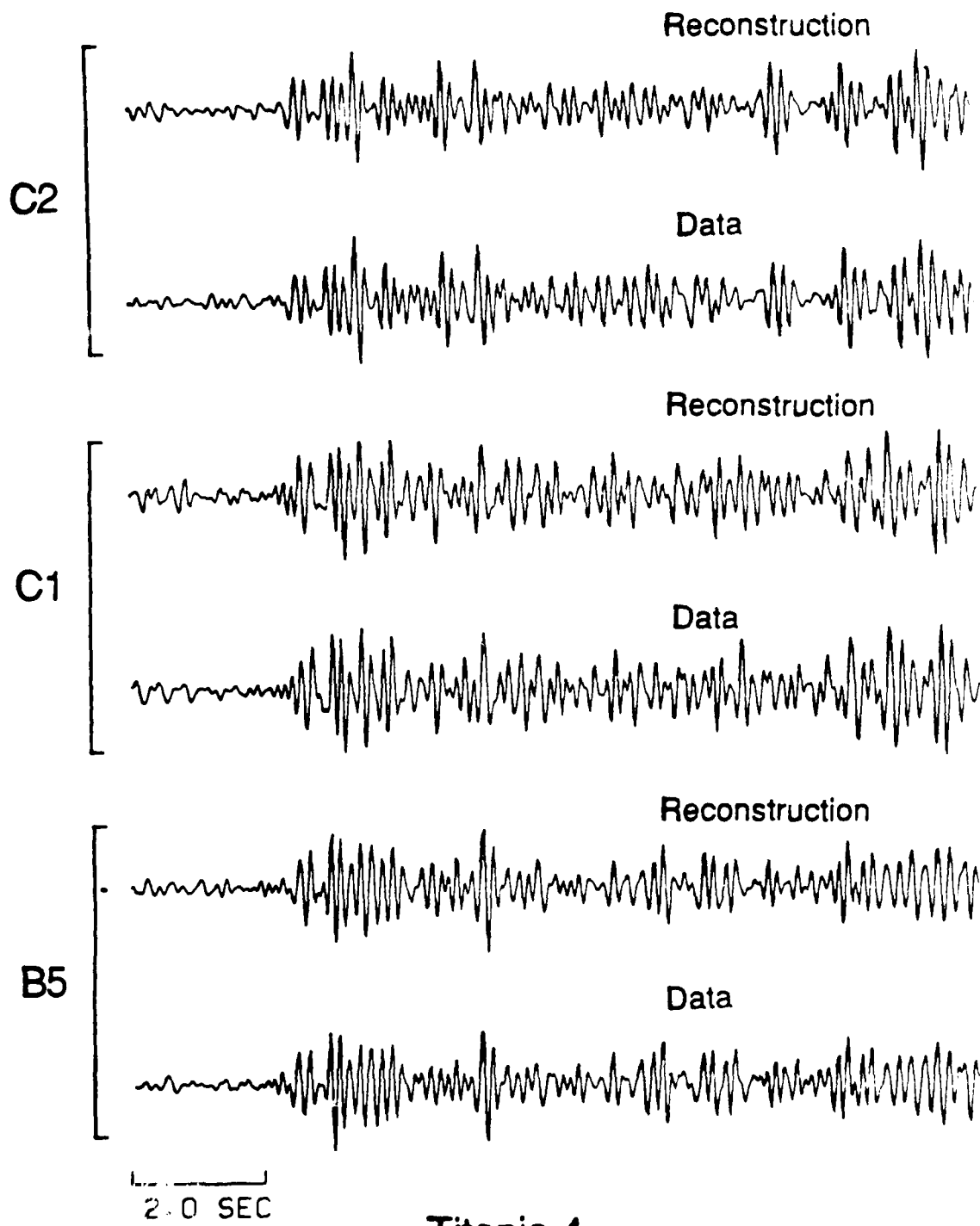


Figure 4. Representative signal and noise spectra of some of the Lg phases originating from Estonia mine events. Only the Lg phases have good S/N ratios, the rest of them are buried in the noise background.



Titania 1

Figure 5 (a). Selected reconstructed and data traces of Pn arrivals from the Titania 1 event.



Titania 4

Figure 5 (b). The same for the Titania 4 event.

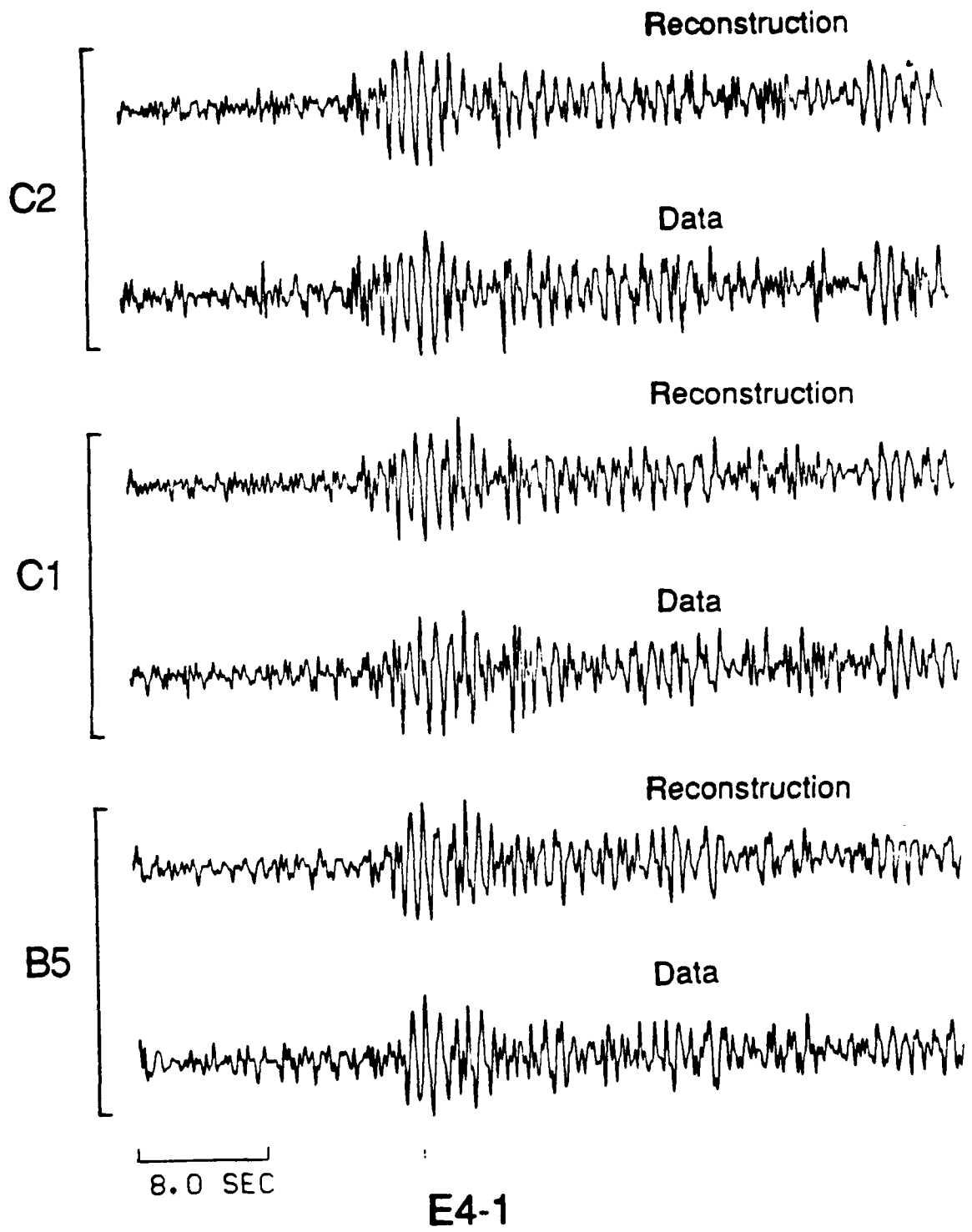


Figure 6 (a) Selected reconstructed and data traces of Lg arrivals from the E4-1 event.

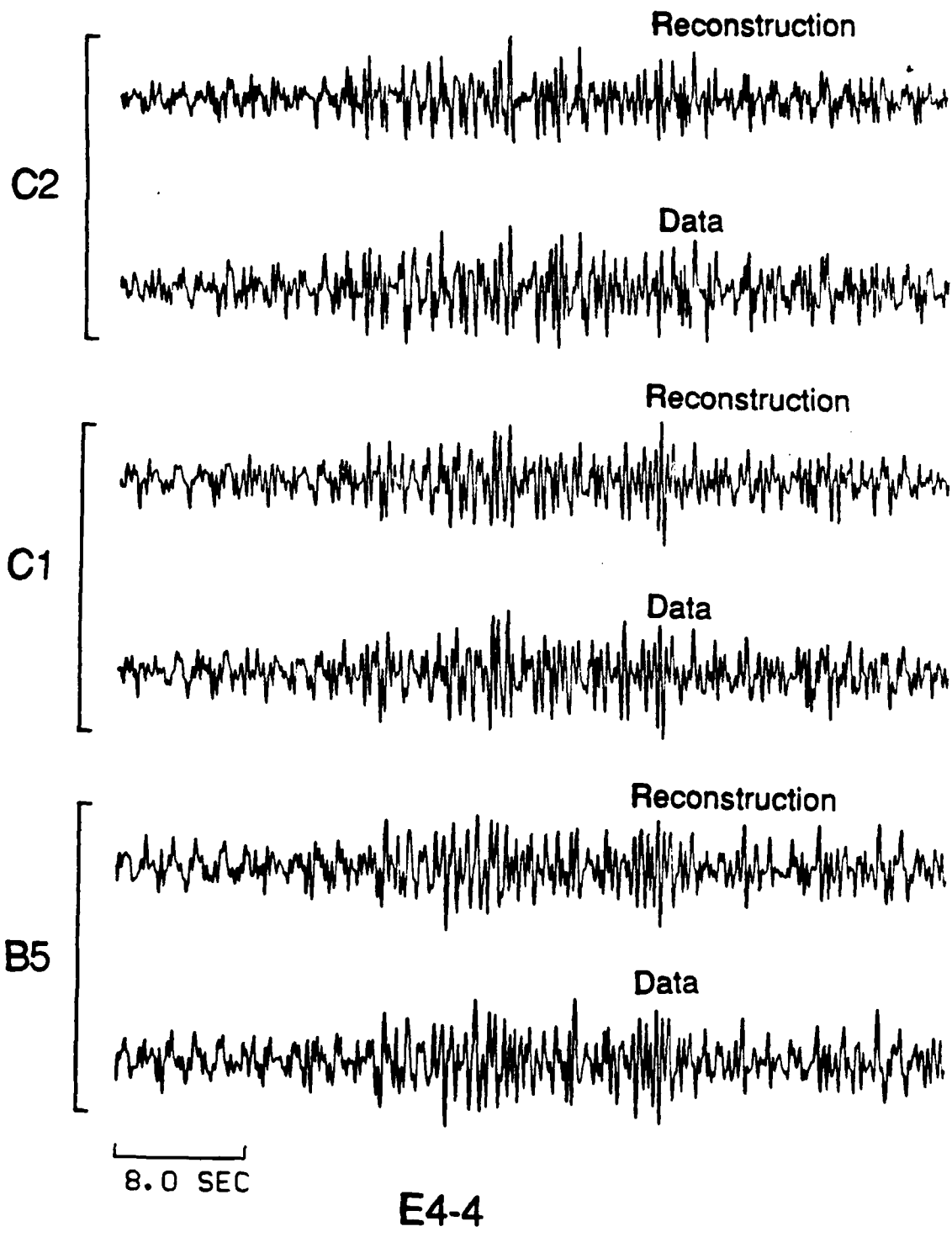


Figure 6 (b) The same for the E4-4 event

Let us compute now the inter-event coherences according to Formulas (5) and (6) above for P_n phases from several pairs of these events in which one of the events is the relatively unmodulated one. The results show that the pairs Titania4-1 and Titania4-3 (Figure 7) show relatively high average coherences, indicating nearly identical source mechanism and/or location; while the pair Titania4-2 has low coherence, indicating that Event Titania3 has probably a different mechanism or location. Although the S/N ratio was the lowest for Event 2, this coherence still seems to be too low for a coherent signal. The TBWP for these coherences was 120.

Let us hypothesize now that the unmodulated event, Titania4, is a simple one, a single shot. Consequently, the time domain impulse response of the moving average (MA) filter that can transform the waveforms of this event to those of the Titania1 must be a band limited representation of the firing sequence. Therefore, we decided to design a Wiener filter to transform P_n waveforms of Event Titania4 into those of Event Titania1 at all sensors of NORESS. Prior to applying this technique, we wanted to ensure that the traces processed are as free as possible from background noise and other distortions of the spectrum by applying a common, minimum phase band pass filter to all traces of both events that emphasized the energy and flattened the spectra in the 3-15 Hz frequency band where the signal-to-noise ratio was higher.

Computation of time-domain MA type filters can be easily accomplished by several well known algorithms using widely available computer codes (*Marple, 1987*). Time domain design is convenient because we want to limit the length of the filter. The P_n arrivals were lined up for both events, windowed and tapered, and the auto and cross-correlation functions needed by the filter design algorithms were computed by ensemble-averaging these correlation functions over sites. The ensemble-averaging of correlation

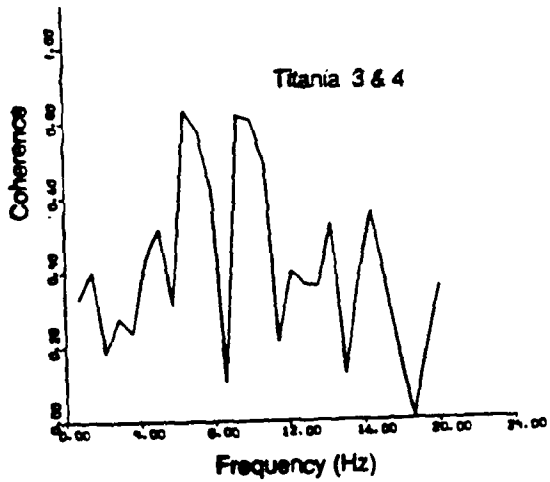
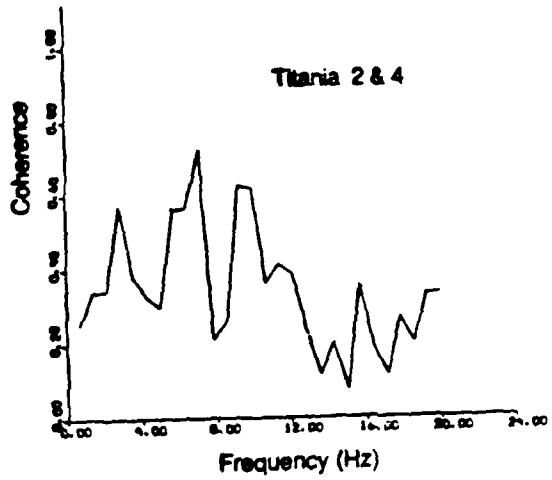
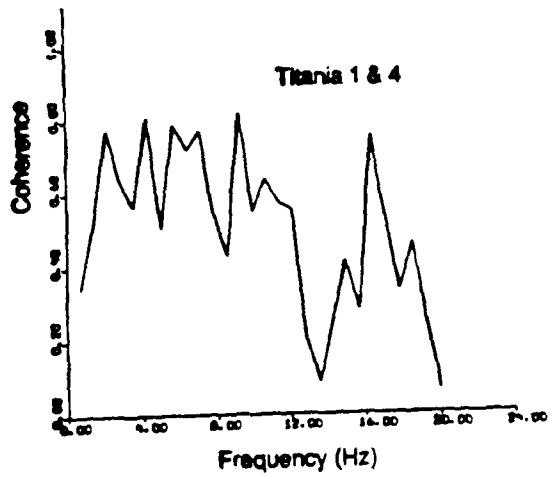


Figure 7. Interevent coherences for Pn arrivals from the Titania mine. While based on the average signal-to-noise ratios most coherences should be well above .75, the lower values indicate, for some events, that the signals themselves must be much less correlated. The degrees of freedom for these coherences was about 120.

functions over common sites suppresses the effects of the site functions and much reduces those of the ambient noise. The length of the portion of the cross-correlation function with the highest amplitudes gave a good indication of the maximum length of the ripple-firing sequence, since the time length of the large amplitudes in this function cannot exceed this length. For the cases discussed, this upper limit is roughly of the order of 0.5 seconds. The compound correlation functions constitute the inputs to the Levinson algorithm used for the computation of the cross-equalizing Wiener filter consisting of 31 weights.

Subsequently, the filter was applied to the simple event to derive waveforms of the complex events at all sites. A set of traces showing the representative improvement between the two events at common sensors are shown in Figure 8. Note that the original waveforms are much more different for the two events and how the waveforms became more similar. Nevertheless, the increase in the time domain correlation coefficients was only modest, from 0.59 to 0.75 for the first pair, and 0.49 to 0.57 for the second. This indicates that either we need a longer filter or that the event pairs are too far from each other; in either case, we cannot attribute the waveform difference entirely to the source time functions. The same method did not work at all for the pair Titania4-2.

We have also applied the cross-equalization for the whole wavetrains, consisting of all the regional arrivals of Events Titania4-1. The processing resulted in a spectacular increase of the correlation coefficients between the two events from .08 to .65 over the whole set of sensors, again confirming that the waveforms of these events are closely related.

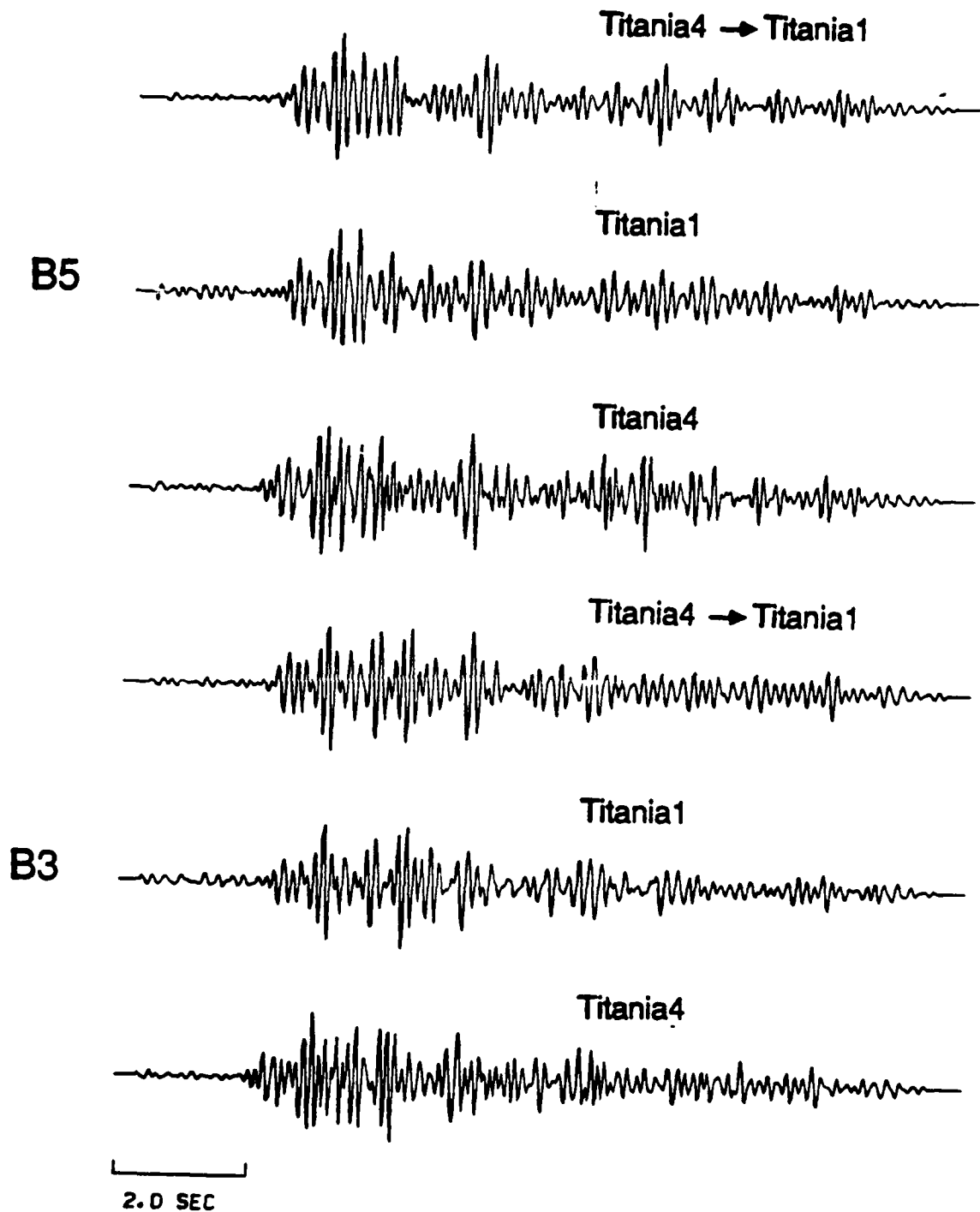


Figure 8 (a) Wiener filtering results for transforming the Pn phases of event Titania 4 into those of event Titania1.

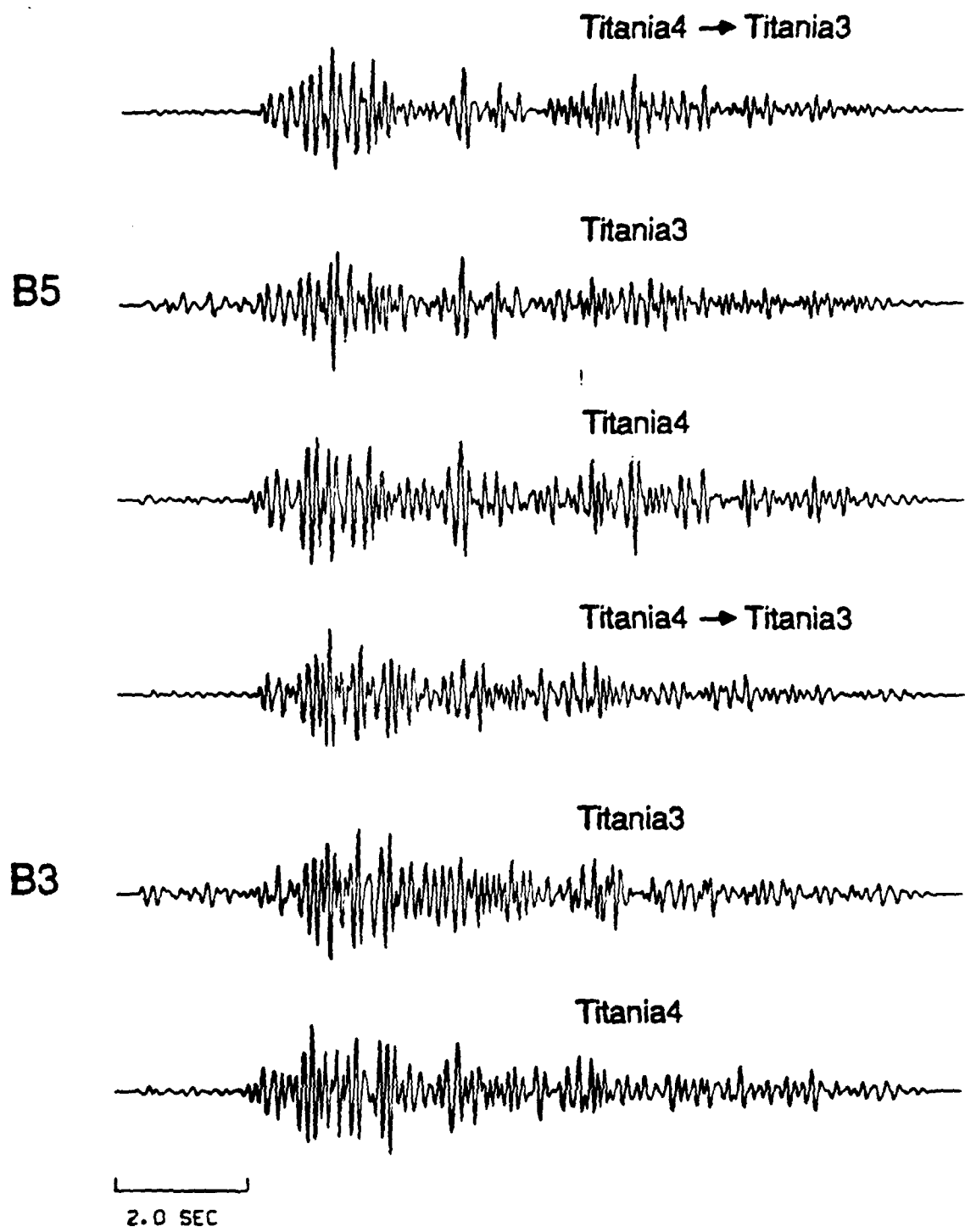


Figure 8 (b) Wiener filtering results for transforming the Pn phases of event Titania 4 into those of event Titania 3.

Having established that such techniques may be suitable for identifying groups of events with nearly identical mechanisms and/or locations, we shall examine the nature of relative inter-site transfer functions for the same event. We know that such transfer functions exist, and that they are consistent from event to event. Otherwise we would not be able to jointly deconvolve and reconstruct all these events. It would be desirable if the transfer functions would be simple, similarly to the inter-event transfer functions for the coherent event pair, because then relative displacement over distances of the order of the NORESS diameter would not destroy the inter-event coherence (applying the principles of reciprocity). In that case, the lack of coherence among events in a limited source region observed at an array would be mostly due to differences in source mechanisms.

Unfortunately, this is not the case. We have tried to design short, 31 point, time domain filters for equalizing P_n waveforms at sensors D1 and D5 for the suite of four events, but they essentially failed to produce even remotely similar waveforms. Thus, the inter-site transfer functions are generally complex, with very long time domain impulse responses. Applying the reciprocity argument, this implies that a comparably small displacement in the location of a source would totally destroy the waveform similarity, assuming that the source region and the NORESS site are similar in the degree of inhomogeneity in structure.

Site Equalization Processing

A major problem in locating regional events is that the first arrivals are often small and buried in noise and that most phases are emergent, without clearly defined arrival times. Azimuths estimated from F-K analyses are often not very accurate, since the site

effects tend to destroy the plane wave character of the signals, thus broadening the main lobes of array response patterns. There are conflicting demands of keeping the array apertures small for ensuring signal similarity and increasing the directional resolution of the arrays. The fact that the site transfer functions are consistent, albeit not simple, still leaves open the possibility of utilizing this internal consistency for refining the estimation of *relative* azimuths among closely spaced events. If the forms of the inter-site transfer functions do not change much with small azimuth changes, except for some small time shifts, then such a property could be exploited. To test this idea we have band-pass filtered the four Titania events to emphasize the band with the maximum signal-to-noise ratio, between 3-10 Hz. Subsequently, we have taken the frequency domain site factors derived from the multi-channel deconvolution calculations and multiplied the Fourier transform of trace D1 with the site factor of D5 and vice versa. This is basically an inter-correlation technique applied to the broadband site (rather than event) equalization. The resulting spectra were then multiplied in the frequency domain and transformed back into the time domain, as described by the formula

$$\Phi(t) = F^{-1} \left| d_1(\omega) R_5(\omega) (d_5(\omega) R_1(\omega))^* \right| \quad (9)$$

to view the cross-correlation function. In this expression the d 's are the Fourier transforms of the traces and the R 's are the site transfer functions. The results for three of the events are shown in Figures 9 and 10; Event 2 was too noisy and was left out. In inspecting these figures, we must point out that the results of cross-equalization do not have to look like normal seismograms, with clearly defined phases. In multiplying with the complex site factors, we essentially perform a circular convolution with considerable wraparound effect. Figure 8 demonstrates that the site-equalized trace waveforms indeed became quite similar. Any small shifts in the peaks do not seem to be associated with noise or mismatch since all

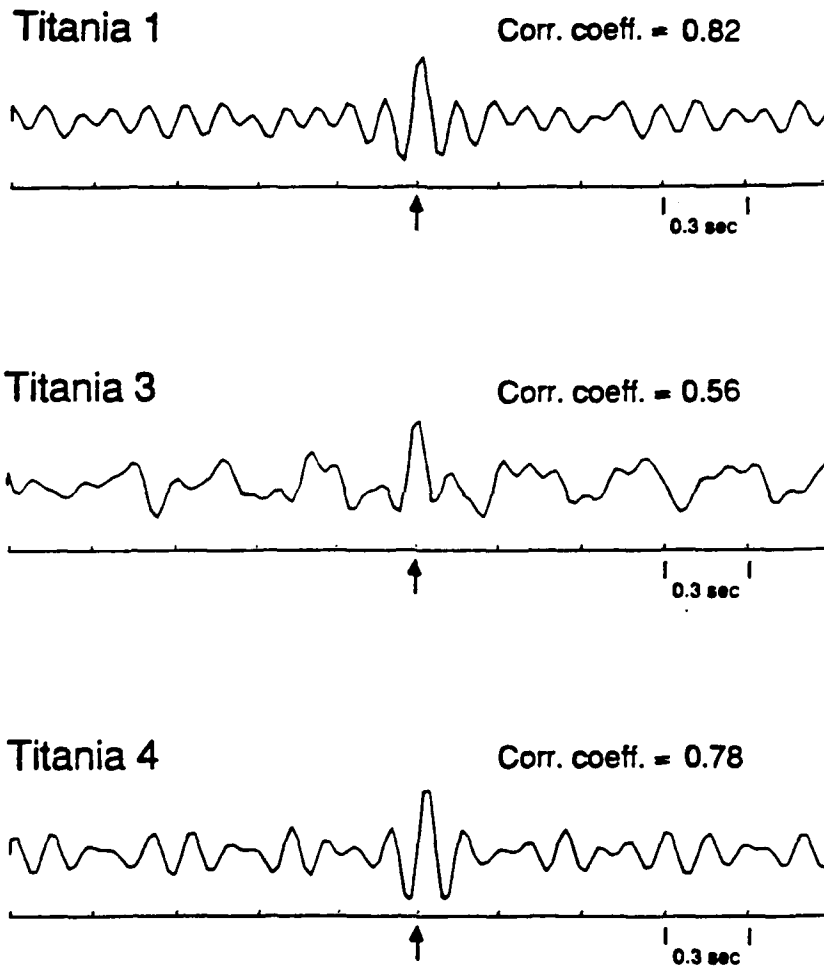


Figure 9. Cross correlations of the site equalized traces of Pn between sensors D1 and D5 for selected Titania events.

Titania1

D5→D1



D1→D5



1.5 sec

Titania3

D5→D1



D1→D5



1.5 sec

Titania4

D5→D1



D1→D5



1.5 sec

Figure 10. Site equalized Pn traces for selected Titania events.

cross-correlation functions for this set of events have a well defined, single maximum with little ambiguity in the time of the maximum.

The same process was repeated with the recordings of *Lg* phases from quarry blasts in Estonia as recorded at NORESS. Applying the process to four E4 mine events, we obtained good trace equalizations, with all correlation peaks lined up at zero lag. Using four events from E4 and two from E1 mines in a joint site-equalization process, we have found that the efficiency of the inter-site equalization drastically deteriorated as indicated by the decrease in the correlation coefficients between equalized traces (Figure 11). The correlation peaks are still generally at the same times, but one of the peaks (for Event E2) is shifted in time. The decrease in site-equalization efficiency may be attributed to the fact that mines E4 and E1 are too far from each other to have identical site functions at NORESS. The waveform similarity is not even visible for this set (Figure 12).

Given the fact that the waveforms become quite similar after applying some cross-equalization treatment to the outputs of a pair of sensors located at the extremities of a small array for events in some limited source areas (not the two Estonia mines together), it may be not justifiable to limit the sizes of regional arrays to a few kilometers. It appears that regional signals from limited source regions are actually "coherent," in the sense of a broader definition of this term, over much larger distances between sensors. Clearly, the maximum array diameters dictated by the average waveform correlation properties (*Mykkeltveit et al, 1983; Der et al, 1988*) do not apply here. It could be fruitful to test and develop similar techniques using data from small arrays larger than NORESS.

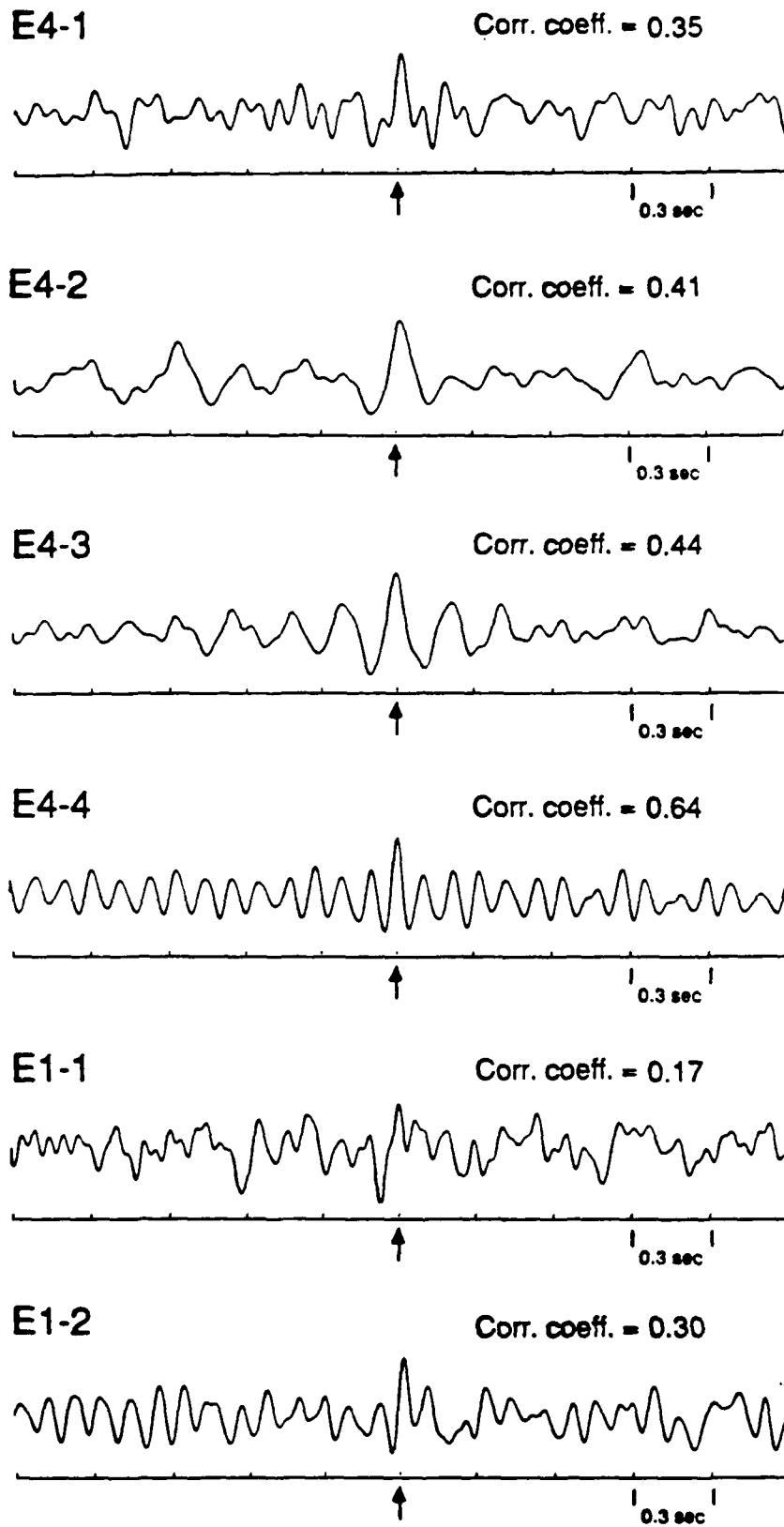


Figure 11. Cross correlations of the site-equalized traces of Lg between sensors D1 and D5 for selected events at the Estonia mine E4.

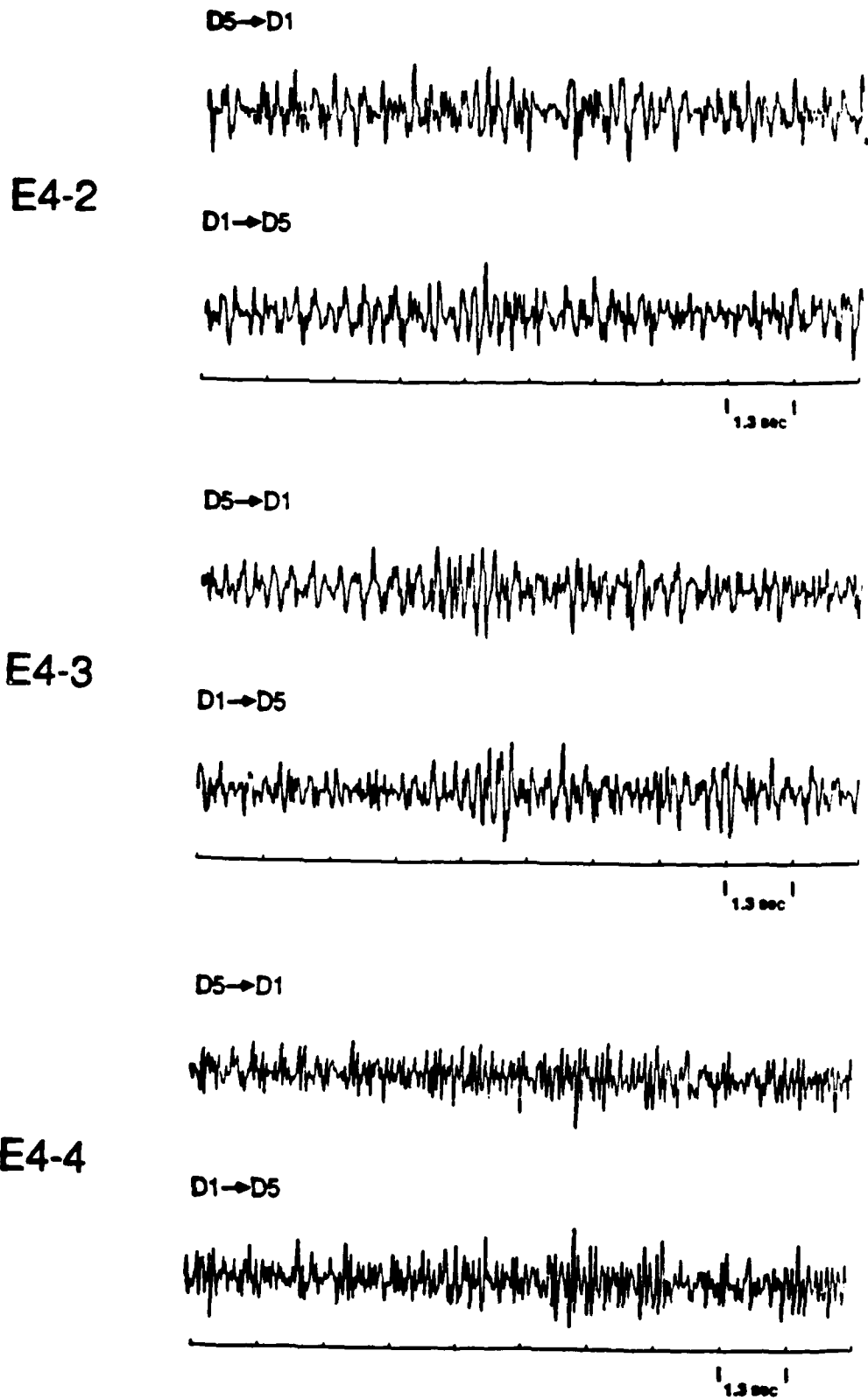


Figure 12. Site-equalized Lg traces for selected events at the Estonia mines E1 and E4.

JOINT DECONVOLUTION OR TELESEISMIC AND REGIONAL DATA

Given the complex nature of regional arrivals, it would be very fortuitous if, similar to teleseismic data, we would be able to see simple P , pP or sP arrivals after deconvolution. Unlike teleseismic arrivals which can be described in terms of a direct P wave and several distinct surface reflections, regional arrivals are made up of numerous generalized rays with various slownesses. It is indeed not possible to see anything similar to P , pP and sP sequences in multi-channel deconvolutions of regional arrivals. A logical modification of the teleseismic multi-channel deconvolution procedure for incorporating regional data could consist of using only the teleseismic data for constructing the source function estimate, thus defining a regional site function which, after dividing it out, would yield the usual simple sequence. In order to test this idea, we have identified two Kazakh events for which EKA, GBA and KAAO data were available. In this set the station KAAO contributed the regional data (P_n), and the two UK arrays the teleseismic data. Joint deconvolution of all these (using the scheme in Figure 13) showed, using the events listed in Table II, that the factorization worked; i.e., the reconstructions were of good quality at both at the teleseismic UK array and the regional KAAO sensors (Figure 14). This seems to indicate that schemes like this could work on larger data sets. Nevertheless, drawing major conclusions from data sets this small would be premature. It was also difficult to find data where we had both teleseismic and regional data of good quality, i.e., where neither clipping occurred or the teleseisms were not swamped by background noise. Widescale testing and possible applications for such schemes may have to wait until systems with very large dynamic ranges and 32 bit digitizers will become common.

**TABLE II - KAZAKH EVENTS USED FOR JOINT DECONVOLUTION
OF REGIONAL AND TELESEISMIC DATA**

Event	Origin Time	Lat (N)	Lon (E)
1978241	04:26:75.9	49.82	78.14
1978162	02:56:57.6	49.90	78.80

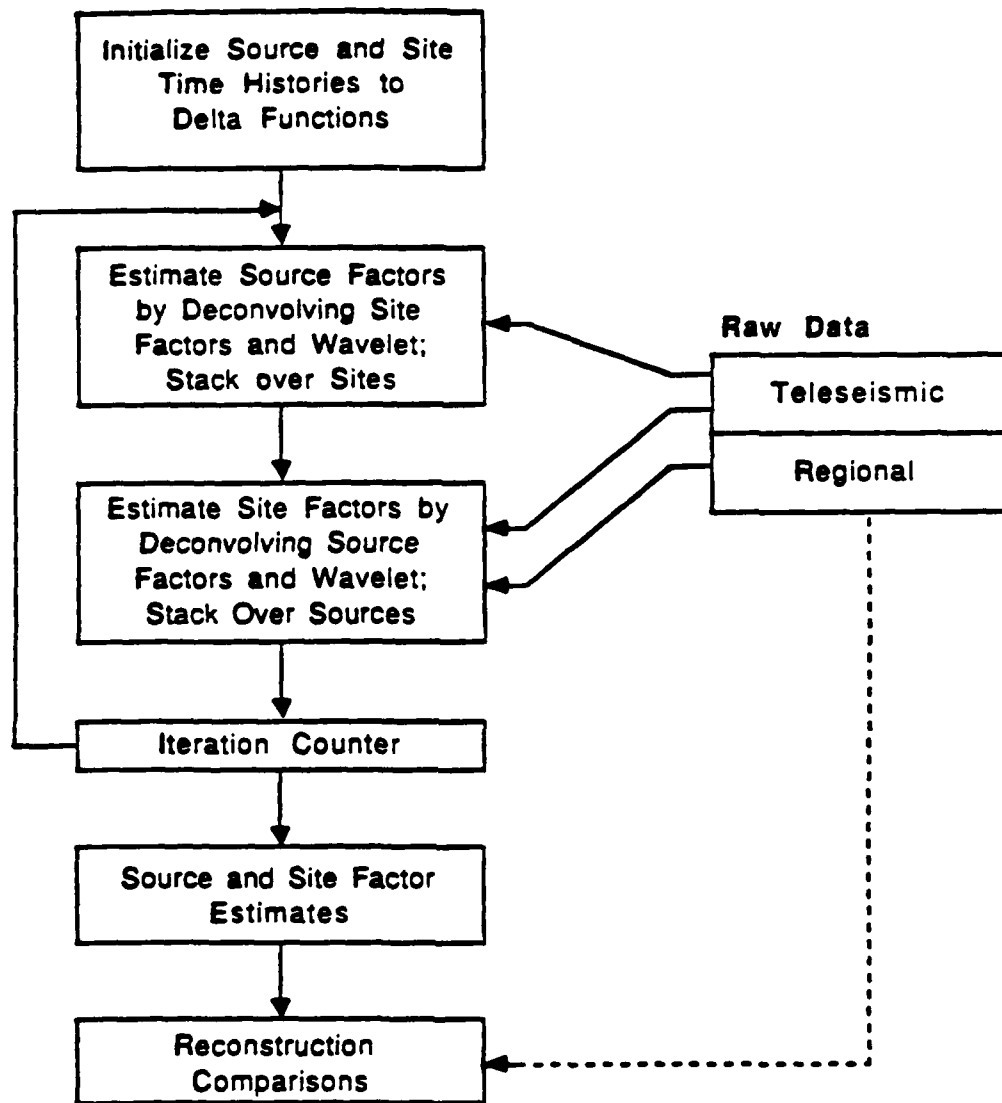


Figure 13. An iterating scheme to jointly deconvolve teleseismic and regional P waves. Only the teleseismic data are used for estimation of source factors, but all traces are utilized for deriving the site responses.

Multichannel Deconvolution Display

press right button for more

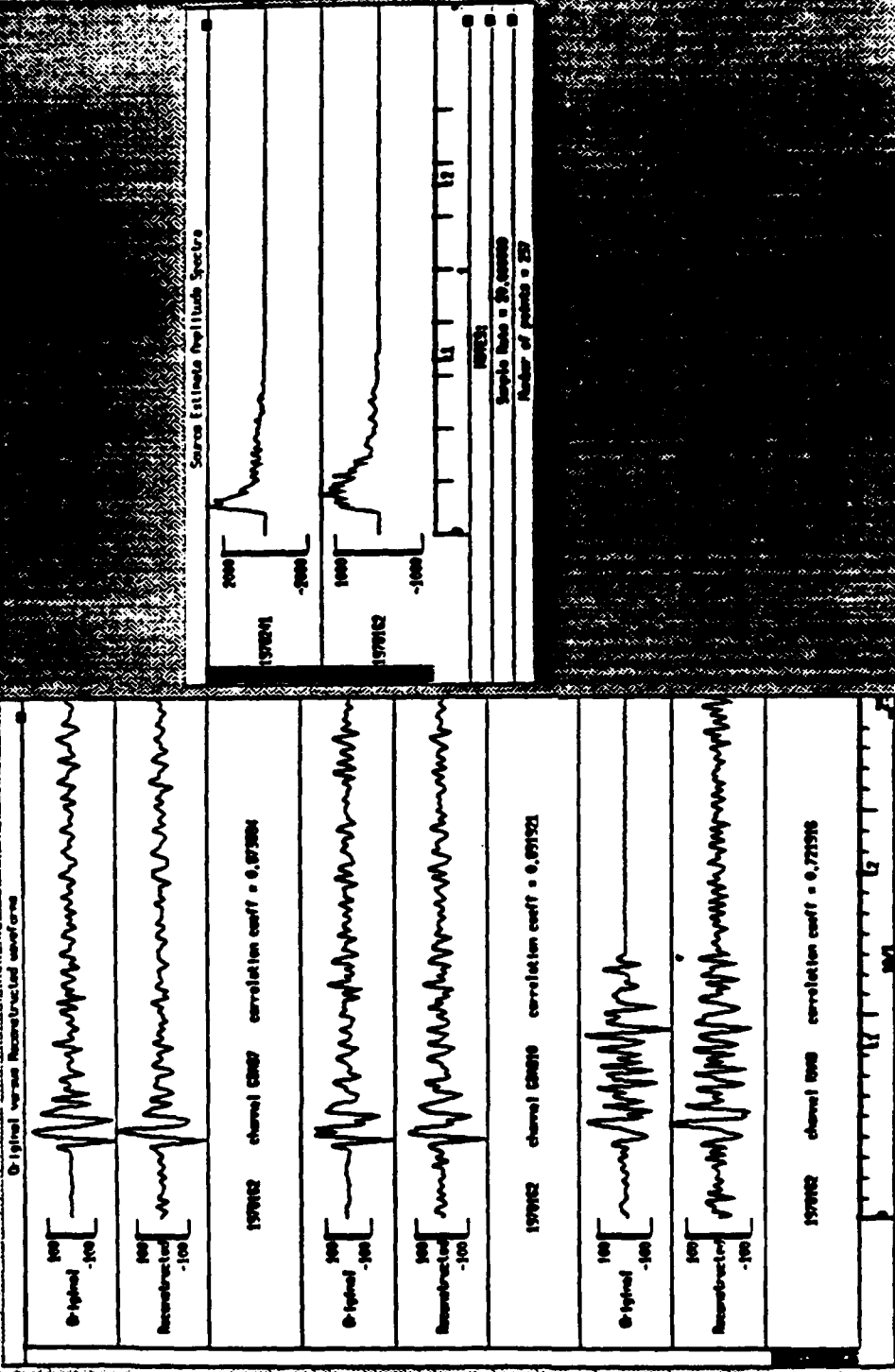


Figure 14. Reconstructions of some of the data at EKA and GBA (teleaseismic), and at KAAO (Pn-regional) from the spectral factors estimated by the scheme in Figure 13.

BROADBAND IMAGING OF SEISMIC SOURCES AND SOURCE INVERSION

GENERAL REMARKS

This part of the report presents a new, general, statistics-based, broadband frequency domain approach to source inversion that avoids much of the subjective bias that is prevalent in time domain direct modeling and source inversion methods. This method is also very suitable for automation of the source inversion and seismic discrimination process.

MOTIVATION FOR FREQUENCY DOMAIN INVERSION

A popular and widely used method for the derivation of source and path parameters from teleseismic recordings is the direct modeling of the observed seismic waveforms. The objective of the procedure is to obtain some fits between the observed waveforms and the synthetic seismograms optimized in some sense. At this point it is assumed that the parameters used in computing the synthetic seismograms are the best estimates for those of the source and path. One can make some interesting observations reading such papers. The most obvious is that the synthetic and real seismograms do not match perfectly and that the differences are usually in the finer, high frequency details of the waveforms. Moreover, the synthetic seismograms usually contain less high frequency than the data even if we allow for the presence of background noise. The inverted source time functions generally contain fine details that depend on the same high frequencies that were mismatched in the waveform modeling process. Numerous publications, using long period waveforms as data claim to have determined source depth to an accuracy of a few kilometers and have seen indications of source finiteness. Such claims in many cases seem

almost too good to be true, considering the wavelengths of the seismic waves at the frequencies where the waveforms seem to fit. Most studies use unmodified data for fitting that were obtained from systems with narrowband characteristics, such as those of the WWSSN network. The qualifiers "generally" and "most" are used above to signify that these observations are not valid for all time domain work of this type and the quality of fits and the claims made also vary considerably. Nevertheless, because of the widespread use of such techniques such apparent discrepancies should be of concern.

While it is easy to make these observations visually, we need some measures of the misfits between synthetic seismograms and data. Let us quantify first the general standards for time domain fitting of long period data. To obtain some quantitative measure of the generally accepted standards of waveform fits we have taken 22 synthetic and data waveforms pairs randomly selected from the literature, enlarged and digitized them on a digitizing table. The differences between the data and the synthetic traces are clearly visible in the original publications, and are not products of the digitizing, i.e., these differences are much larger than any plausible digitizing errors.

In order to obtain a measure of goodness-of-fit in the time domain we computed the correlation coefficients between data and synthetic waveforms

$$C = \frac{\int_0^T d(t) \cdot s(t) dt}{\sqrt{\int_0^T d^2(t) dt}}$$

This is also the most common measure for judging the quality of fit in time domain waveform inversion studies (if any quantitative measures of waveform similarity are applied at all). For our selected sample a histogram of correlation coefficients, shown in

Figure 15, illustrates that the average time domain fits we have chosen have correlation coefficients averaging near 0.9 with a few over 0.95. Several of the waveform pairs are also shown in Figure 16. These figures should convince the reader that we have not purposely chosen poor waveform fits to make our point, but that these are better than the average fits in the literature. The synthetic seismograms also contain less high frequency than the data in accordance with visual observations that anyone can make by reading such studies (Figure 17). Moreover, the spectra are sharply peaked, giving the data a narrowband character. We would like to establish some relationship between the quality of time domain fits and the resolution in the spatio-temporal configuration of sources derived from the data.

Let us evaluate now the data vs synthetic fits *in the frequency domain*, using FFT's of the data and synthetic traces, and using an alternative similarity measure for the same data set. This measure is an ensemble-averaged coherence

$$C(\omega) = \frac{\sum_i \overline{d_i(\omega) s_i^*(\omega)}}{\sqrt{\sum_i \overline{d_i(\omega) d_i^*(\omega)} \sum_i \overline{s_i(\omega) s_i^*(\omega)}}$$

summing (ensemble averaging) over waveform pairs i and applying spectral smoothing as denoted by the overbar. By plotting this as a function of frequency (Figure 18), the problem with time domain waveform fitting with narrowband data becomes obvious. While the fit near the peaks of the spectra are good (but by no means perfect) with a coherence a little over 0.9, this fit rapidly decreases in quality with increasing frequency. Although we are confident that our digitization is good at least to 0.3 Hz, the coherence at this frequency and below it is essentially indistinguishable from zero for this data set. Note

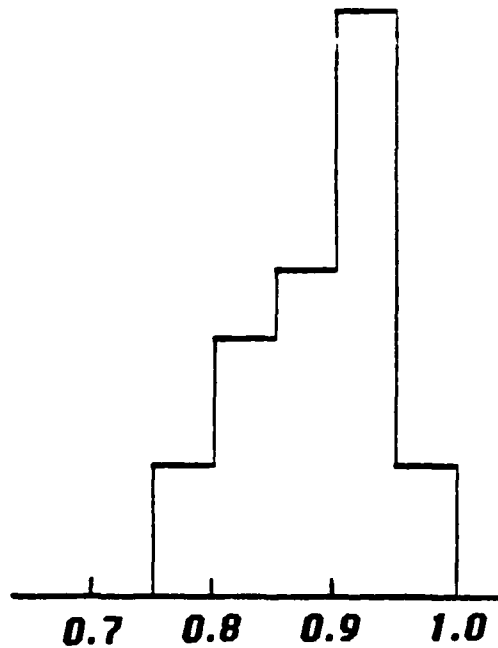


Figure 15. Histogram of time domain correlation coefficients between synthetic seismograms and data randomly selected from the literature.

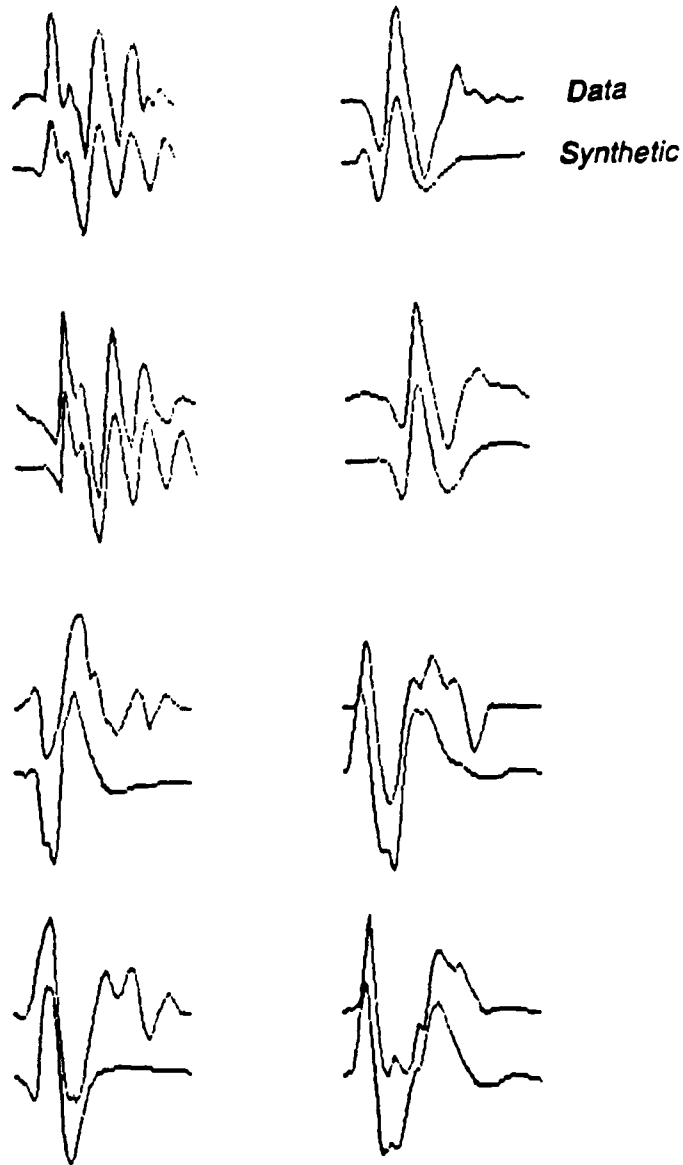


Figure 16. Examples of selected data and synthetic seismogram traces.

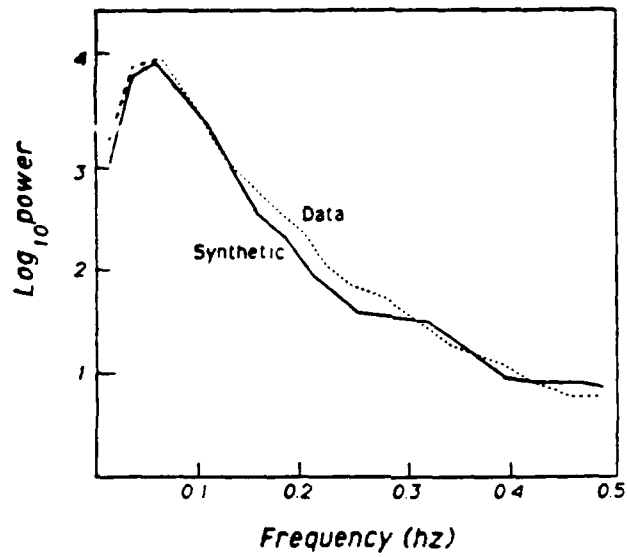


Figure 17. Comparison of averaged spectra of selected data and synthetic seismograms.

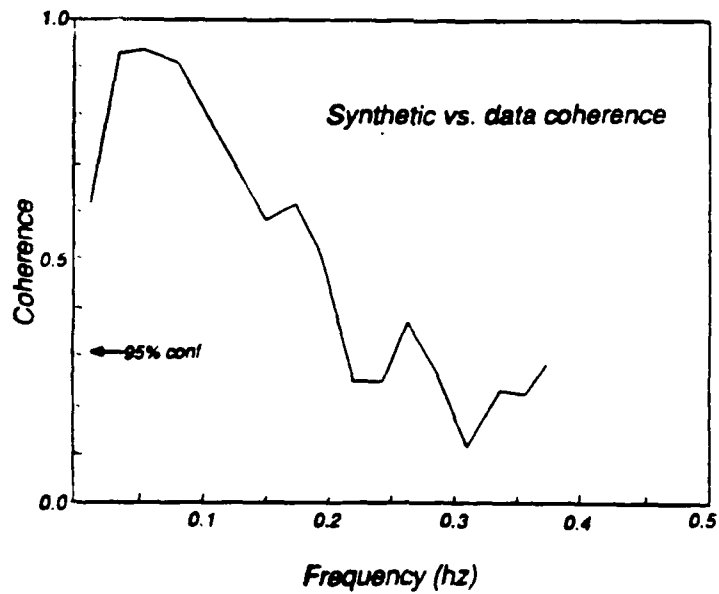


Figure 18. Ensemble-averaged coherences of our sample of data-synthetic pairs defining the "average fit."

that this test could not even be performed with data from any single study since practically none of them use as many as 22 stations. We shall designate this coherence plot as representing the quality of a "standard fit" in time domain modeling of long period data. Clearly this standard will have a profound effect on the resolution of the time-space details of sources.

With regard to the source time function it should be obvious, when looking at the inverse source problem formulated in the frequency domain, that it is simply not possible to say anything about the higher frequency details of the source function at all if the corresponding frequency components are not matched in the data as indicated by Figure 16. This is because the problem becomes completely frequency-separable in the frequency domain as seen by transcribing the well known equations from *Aki and Richards (1980)*

$$u_n(x, t) = M_{pq}(t) * G_{np,q}(t) + N_n(t)$$

into the frequency domain

$$u_n(x, \omega) = M_{pq}(\omega) \cdot G_{np,q}(\omega) + N_n(\omega)$$

The problem in the frequency domain also becomes much simpler and easier to solve (*Olson and Anderson, 1988*) and instead of taking the time domain trace amplitudes as data, we could fit the amplitudes and phases of the various frequency components at the various recording stations. It also follows by simply inspecting the formulation above that descriptions of fine details found in the space-time structure of seismic sources are not credible unless the quality of time domain fits is improved at higher frequencies. This is a very obvious and trivial point that is frequently overlooked.

The points made above give a basic reason for our search for alternative methods and some quantitative tests for source inversion, and we return to these arguments after the next section. We shall show that the average quality of time domain fits as described by the coherences in Figure 18 are barely, or not at all, sufficient for deriving source depth and other source parameters to any useful accuracy. In fact, most work of this type seems to operate on the border of non-resolvability and marginal significance. In the next section we describe a new, promising alternative approach to source inversion. We do not claim that our approach is the best possible one; other methods, just as good or better, could probably be found.

METHODS FOR SEISMIC IMAGING

Looking at the mathematical problem of using a set of seismic signals from a number of seismic stations and trying to estimate the energy coming from a given location of the source region, it can be shown to be identical in mathematical form to F-K analysis where the vectors of beam steer operators (phasors) f are replaced by some more general operators (Green's functions). Instead of having components with absolute value unity, as in the array beam-steer case, now we may have to normalize the "beam" results by dividing with $f f^*$. Nevertheless, we have as before a number of F-K algorithms available to us in this application. The first one is the generalized beam, robust and plagued by side lobes:

$$\frac{f S f^*}{f f^*}$$

the second is the *Capon (1969)* estimator, a high resolution operator with poor stability

$$C = [f S^{-1} f^*]^{-1}$$

And finally, the Shumway estimator a good compromise between the first two:

$$F = \frac{\frac{f S f^*}{f f^*}}{tr S - \frac{f S f^*}{f f^*}}$$

where S is the spectral matrix of the input data (typically an outer product of the Fourier transforms with a small proportion of unit matrix added, see Appendix A). Using various appropriate f vectors, we can now examine the source radiation in space (horizontal coordinates and depth). We shall discuss the properties of these statistics in some detail in Appendix A.

Ideas similar to these were advanced by *Goldstein and Archuleta (1987)* in seismology and *Baggeroer et al (1988)* in underwater acoustics using the MUSIC algorithm and the Capon algorithm respectively (*Capon, 1969*). The third algorithm we prefer does not have some of the undesirable properties of Capon's method in this application. The statistic has an approximate noncentral F distribution at individual frequencies under the null hypothesis (no signal) with 2 and $2(N-1)$ degrees of freedom for N input waveforms. If we stack the results for the same source coordinates obtained at various frequencies, the probability density function of the result is approximately normal with mean Mm and variance $M\sigma^2$ with M the number of frequencies used in the stack, and m and σ being the mean and the standard deviation of the individual F distributions.

APPLICATIONS OF THE FORMALISMS TO VARIOUS SEISMOLOGICAL PROBLEMS

Let us assume now that we have observed seismic body waves from a seismic source at numerous stations at various distances and azimuths from the source. In this case, we know the wavenumbers at each station for each particular wave type may construct an image of the source. Assuming that we know the source mechanism of an elementary source (slip on an element of a fault plane at a given depth) and that the source region is horizontally homogeneous (flat layered), we may write the components of vector f as

$$f_i(\omega) = C_i(\omega) \exp(j \omega s_i \hat{k}_i \cdot x)$$

where the first factor $C_i(\omega)$ is a frequency domain radiation pattern appropriate to the crust and to the azimuth-slowness for P waves seen at station i , i.e., the sequence of P waves following the various types of rays possible for a source of that type at the given depth; the exponential factor corresponds to horizontal translation with respect to the source position vector x , and the unit wavenumber vector appropriate to a given station i is denoted by \hat{k}_i . In laterally heterogeneous structures the translation must be described by more complicated functions, but the general principles are the same.

Alternatively, we may wish to analyze surface waves observed at a set of stations in a similar way. Then the components of the f vector become

$$f_i(\omega) = P_i(\omega) \exp[j \omega \hat{k}_i \cdot x / c_i(\omega)]$$

In this case, the waves are dispersive and the phase velocity depends on frequency, and $P_i(\omega)$ is the source radiation pattern in the direction of the station i . The exponential again describes horizontal translation in laterally homogeneous models.

It is easy to see that this approach can be generalized to source region structures of any complexity and any combinations of observations. For laterally heterogeneous structures no simple exponential factors could be used for effecting horizontal translation, of course, but the essential mathematical forms shown above would still be valid.

The formalism also provides an objective way, as opposed to visual fits in the time domain, to compare, over a chosen frequency band, synthetic seismograms to data. In this application the S can be an outer product of observation vectors (FFT's of data) and the f 's could be the vectors of FFT's of synthetic seismograms using various parameterizations. The parameterizations that maximize any of the statistics defined above will be the best fits. This way many of the problems with time domain fitting discussed below can be avoided.

We present three figures to illustrate that these concepts work and that the statistics indeed have maxima at coordinates (and other parameters as well) which coincide with the actual positions of sources. In Figure 19 we show a source image, in the form of depth slices of a point source located at 6 km depth at the center of the 2 dimensional grid. This image was constructed using Shumway's formula. In Figure 20 we show some synthetic Rayleigh waves which were used for constructing the image in Figure 21. The corresponding image, constructed with Capon's formula, is shown in Figure 21.

$0.05 \text{ Hz} < f < 0.333 \text{ Hz}$

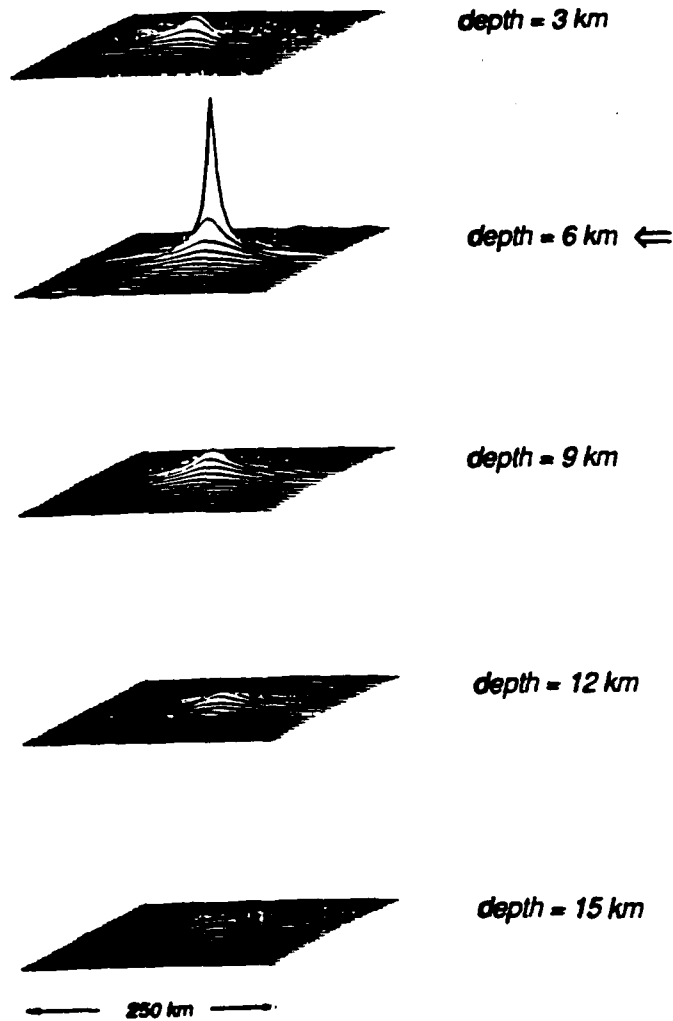


Figure 19. Images of a double-couple point source at various assumed source depths with 5% white noise constructed from synthetic P wave seismograms at 10 teleseismic stations well distributed in azimuth and slowness. This S/N ratio corresponds to a fit with a correlation coefficient near 0.99. Shumway's algorithm was used in this example.

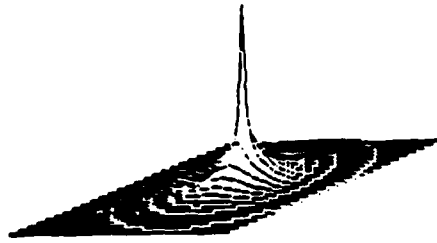


Figure 20. Image of a double-couple point source with 5% white noise constructed from synthetic Rayleigh wave seismograms at 8 teleseismic stations well distributed in azimuth, Capon's algorithm was used in this example.

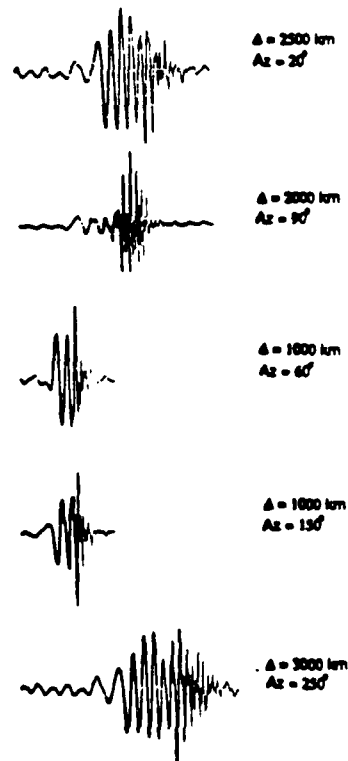


Figure 21. Synthetic surface waves used for constructing the image in Figure 20.

SIMULATION RESULTS

The Capon and Shumway algorithms have been implemented in FORTRAN and tested for correctness. These computer programs, besides their uses in data analyses, are also suitable for investigating the sensitivity of these methods to perturbations in the data and for the testing of the resolution obtainable from such methods for various source parameters, most notably in the spatial details of the sources. In the following we present the results of some simulations.

Testing the Consequences of "Average Fit" in the Time Domain

Having defined the statistics providing source image, let us examine how misfitting waveforms in the fashion described in Figure 18 will distort a source image, and affect the results. For simplicity we shall assume the source crust to be a halfspace so that the generalized beamsteer vector becomes

$$f_i(\omega) = \left\{ \sum_{j=1}^3 a_{ij}(\omega) \exp(-i\omega t_{ij}) \right\} \exp\left(-i\frac{\omega}{c_i} \hat{k}_i \cdot \mathbf{x}\right)$$

where the subscript i refers to the particular station, and the subscripts $j=1,2,3$ refer to the phases P , pP and sP , respectively.

Where \mathbf{k} is a unit vector appropriate to a station i , \mathbf{x} is a position vector in the source region, the c_i are phase velocities at a given station, the t_{ij} are the travel times of the P , pP and sP phases. The source image is a mapping of F over the source region in depth and horizontal coordinates. Depth dependence enters into this formulation by the delay

times of the depth phases and the exponential factor will be determined by the horizontal coordinates of the source. We thus assume, for the sake of convenience, that the Green's functions are perfectly known, which is generally not the case. The common problem of poorly defined Green's functions, which makes the inverse problem even less tractable, is not addressed here.

The statistic, F , becomes infinite for the case of perfect fit, i.e., in the noiseless case. Having developed a statistically tractable representation of the source, we apply this algorithm now to a typical inversion problem, one with ten azimuthally well distributed stations (30 degrees apart) and having three associated P wave slownesses (0.05, 0.06 and 0.08 sec/km). The simulated data consisted of teleseismic P waves from a double couple source (strike=245°, dip=30° and rake=120°) situated at 6 km depth. In Figure 19 we have shown images of this source, located at the center of the search grid, at different depths. In this figure we have increased the trace term in Shumway's formula by 5% in order to keep the statistic finite and used the frequencies between .05 and .333 Hz with equal weight.

To investigate how this clear image degrades as we perturb the signals, we decrease the coherent part of the inputs by some factor and add some uncorrelated random contributions to them such that the average power at each frequency remains roughly the same; but the average coherence at that frequency achieves the desired value. Using these corrupted inputs in the imaging process, we can assess whether the misfitted synthetic waveforms are still defining the same source image as the data, which is assumed to be correct. Alternatively, we may consider these images as the true source entirely consistent with the perturbed inputs and the original clear images as alternatives to them that fit the data within some tolerances.

In the first simulation we have added about 10% uncorrelated noise (in amplitude ratio) evenly throughout the frequency band quoted above. This corresponds to about a 0.99 correlation coefficient between the original and perturbed waveforms having flat, broadband characteristics in the band indicated. These waveforms still give a somewhat rugged-looking, but clear, well-defined image of our source (Figure 22). We must note, however, that correlation coefficients between the synthetic and original waveforms associated with this problem are far better than those commonly seen in waveform studies.

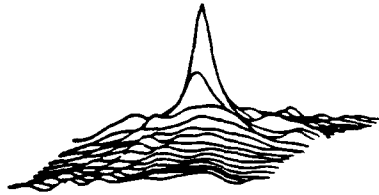
Next the standard for the "average fit", defined by the coherences in Figure 18, is applied to the problem. Again, we add a proportion of random uncorrelated noise to reproduce the coherences for "average fit" and construct an image. We would expect that for acceptable misfits (perturbations) the main features of the solution would remain intact. This expectation is not met, however, since it can be seen in Figure 23 that the image disappeared totally. Repeating the same procedure in a narrower frequency band of 0.05-0.15 Hz, in order to utilize only the frequency components which are correlated with the highest coherences in Figure 18 (near 0.9) in Figure 24, we still have some very poorly defined peaks. The maximum is at the wrong depth and is off center and there are maxima of roughly the same size at greater depth near the edges of the grid.

As a final test, we decided to reverse the trend to progressively poorer fits and increase the S/N (coherent and random noise ratio) in the narrower, 0.05-0.15 Hz, frequency band to correspond to a correlation coefficient of about 0.97. With this value we are starting to see the image emerging again, but the maxima at 3 and 6 km of depth are the same to four decimals (we marked them both in the associated Figure 25). On the positive side, the maxima at greater depth are considerably smaller; thus it can be claimed that the depth was resolved to an accuracy of ~6 km. Nevertheless, to achieve this, it was

$0.05 \text{ Hz} < f < 0.333 \text{ Hz}$



depth = 3 km



depth = 6 km ←



depth = 9 km



depth = 12 km



depth = 15 km

← 250 km →

Figure 22. Image with 10% random noise added, otherwise the synthetic data used were the same as in Figure 19.

$0.05 \text{ Hz} < f < 0.333 \text{ Hz}$



depth = 3 km



depth = 6 km ←



depth = 9 km



depth = 12 km



depth = 15 km

← 250 km →

Figure 23. Image of the same point source by adding noise such that the coherences correspond to the "average fit" in the 0.05-0.333 band.

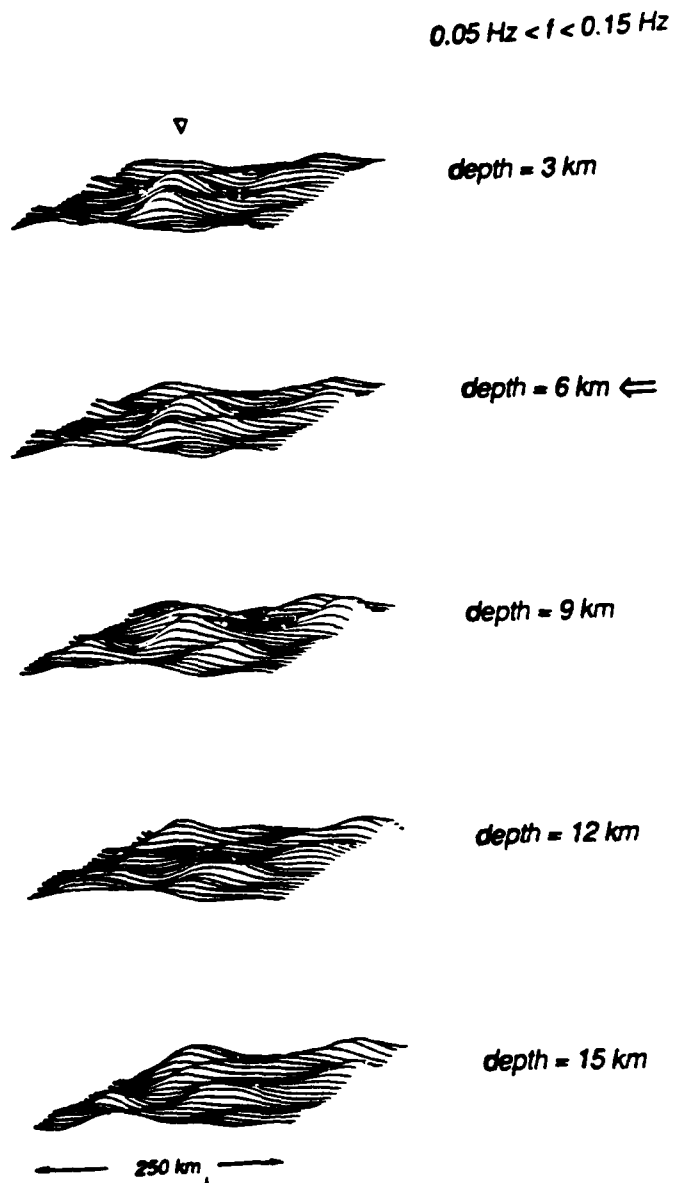


Figure 24. Image of the same point source by adding noise such that the coherences correspond to the "average fit" in the 0.05–0.15 band.

$0.05 \text{ Hz} < f < 0.15 \text{ Hz}$

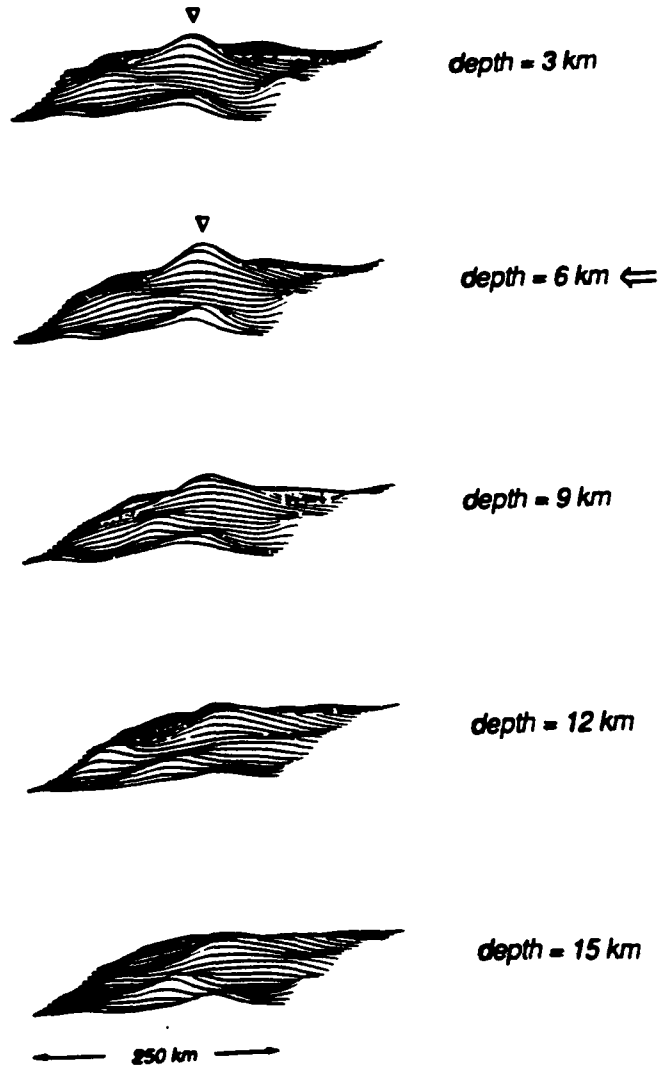


Figure 25. Image of the same point source by adding noise such that the coherences correspond to the time domain correlation coefficient of .97 in the 0.05-0.15 band.

necessary to increase the degree of correlation to a level not commonly attained in data-synthetic comparisons. It is disturbing to find that the imaging procedure breaks down at precisely the correlation level deemed "acceptable" by most time domain studies.

The above findings do not imply, of course, that the conclusions drawn from all direct waveform modeling studies are invalid. Many studies do not make excessive claims with regard to fine details of source time functions, source depth, and faulting history. Many are no more than point source solutions where some surface reflections were utilized to refine the source parameters. The qualities of waveform fits and the number of stations utilized also vary considerably, although generally most fits are no better, and many are much worse, than the ones we picked for analysis. Nevertheless, the instability of the results with respect to small perturbations in the fits of the various frequency components of the signals indicate that many published conclusions in such studies must be marginal at best and probably could not be substantiated even by some simple elementary statistical tests. It appears that although comparisons of synthetic and data waveforms may appear to be impressive, they do not seem to be sufficient to ensure stable or even valid results and that good visual waveform fits and high synthetic-data correlation coefficients of narrow-band raw seismograms mean much less than it is generally assumed.

Simulating a Fault

The examples shown above illustrate that the method works, i.e., images have maxima where the actual sources are located. Instead of imaging point sources, it is more interesting, from a practical point of view, to examine how cases with multiple sources can be handled. In Figure 26 we show an image of a fault, made up of a row of point sources diagonally arranged in the x-y plane at the same depth. This image was formed by using

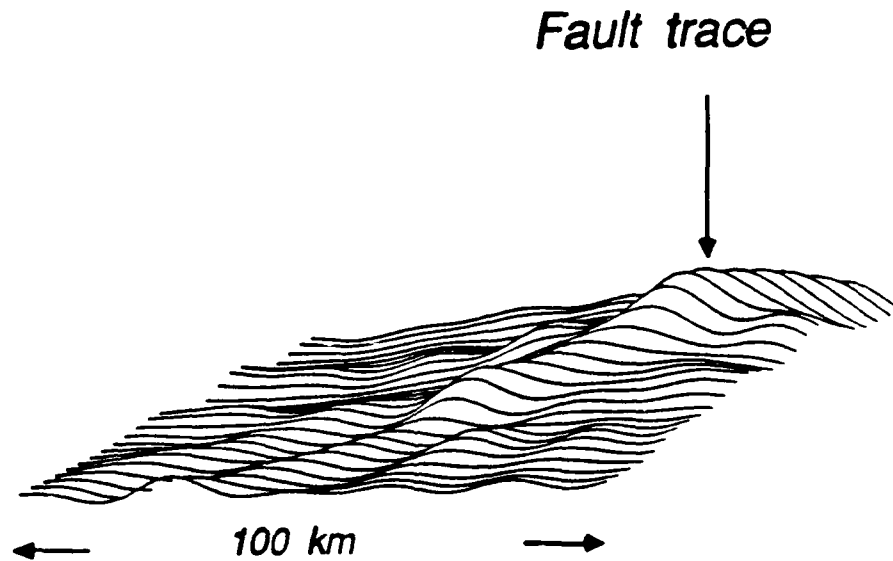


Figure 26. A fuzzy image, indicative of the resolution that may be achieved with good quality real data for large events, of a simulated fault obtained using Shumway's algorithm. The fault runs at a 45° angle with the sides starting from the center of the plot.

Shumway's method and using the f vectors appropriate to a single point source. In imaging we have increased the trace of the matrix in the equation for Shumway's statistic by a factor of 2. This improves the image by reducing a large maximum generated by the low frequency components of the signal that otherwise would dominate the image. This image is intermediate between a generalized beam and the one that we would get from the exact Shumway formulation. Simulations like these are ideal for assessing the resolution of the method and its dependence on the number of stations, their azimuthal and distance distribution, and the frequency range utilized. The poor resolution in Figure 26 is the result of the fact that only eight simulated stations were used. Although it may not be obvious, such limitations are equally valid for other types of source inversion studies.

Separating the Compressional and Double Couple Contribution From Surface Waves

Another interesting problem is that of the separation of explosion and double couple contributions in a set of seismic surface waves. An obvious application is yield estimation from surface waves when tectonic strain release is present. We want to reduce the effects of the double couple component and estimate the energy in the compressional source contribution. For this application the Capon's algorithm seems to be the most suitable, since it is essentially a formulation for the energy in an output of a constrained optimum filter designed to reduce the noise (double couple component) and pass the signal (compressional component) undistorted. The original formulation of Capon's F-K algorithm has the inverse noise spectral matrix N instead of that of data S . In most imaging applications (*Baggeroer et al, 1988*) of this the total data spectral matrix containing contributions from both the desired signal and the undesirable noise (strain release in our case) is substituted. This may have serious consequences, however, in the case of mismatch (*Cox, 1973*). In our simulations of extracting the compressional contribution we

shall use the original formulation of *Capon (1969)* and will use the spectral matrix constructed only from *a priori* estimates of the average strain release sources assumed to be thrust events (typical for Kazakh). The resulting algorithm will be more stable and much less sensitive to mismatch. It must be possible, however, to obtain some estimate of the average strain release spectral matrix, although this estimate need not be very accurate.

Table III shows the results of such a simulation where a constant compressional source superimposed on variable levels of a strain release source (thrust fault) was processed by Capon's algorithm. The "noise" spectral matrix was constructed of a superposition of thrust fault contributions (that also included the simulated fault used in the input) the fault orientations of which were varied over a range of five degrees to account for the uncertainties and variations in the strain release components. The table shows that the power in the output (signal estimate) did not vary much, although the ratio of the compressional and "strain release" components did. Only at extremely large ratios can we see a breakdown of the process. This indicates that such a processor could work, despite the uncertainties and variations in the strain release components. In contrast to the presently used painstaking procedures of fitting radiation patterns to the data, estimating and subtracting the strain release components, this procedure can be automated, performed instantaneously after receiving the surface waves from the event.

**TABLE III - OUTPUT OF CAPON'S ALGORITHM
FOR SOURCE SEPARATION EXPERIMENTS**

Relative Earthquake Component	Output Amplitude
0.	1.0
0.17	1.0
0.333	0.99
0.5	0.99
1.	0.99
5.	1.1
10.	1.4

The only problem that needs to be solved is to obtain in practice good prior estimates of the compressional and strain release spectral matrices. These can be obtained empirically, either by finding events with low strain release (small Love waves) or manipulating several events with similar strain release mechanisms, but different degrees of strain release. Such a procedure involves translating the two events to the same location by phase shifting and differencing their spectra to obtain estimates of a pure compressional source. This process would totally eliminate the need for complex "path corrections." It is possible, however, that the method may not work over larger areas (exceeding 70 km in diameter) due to waveform distortions caused by scattering of Rayleigh waves (*Rivers and von Seggern, 1979*). This would not detract from the usefulness of such an approach, since other methods such as that of *Stevens (1986)* would be also affected by the same problem.

DATA ANALYSES

Imaging of Selected Nuclear Explosions at Kazakh.

In order to test our scheme of source imaging we have selected two Kazakh events for which we had deconvolutions at three UK arrays (*Der et al, 1987*). Taking the deconvolved traces at these three arrays, we have used the model of an explosion source in a halfspace to design the f vectors in the procedure. Since we have only three waveforms, complete imaging in the horizontal plane was not practical since it is not possible to make a good image with only three azimuths. Therefore, we have tried to match the depth only.

We must point out that while we are trying to match an ideal model, the actual deconvolutions may not contain a true pP in the sense of an elastic model. Moreover, even if the simple elastic model were applicable, the bandwidth limitations of the data may not allow us to resolve the true depth. These caveats notwithstanding, if we plot Shumway's statistics as functions of source depth they indicate shallow source depths (Figures 27 and 28). Thus, the deconvolved seismograms best resemble an elastic compressional source at shallow depths; this is more than we can deduce from location calculations at teleseismic distances.

It appears that our imaging procedure may be a good equivalent or substitute for the discrimination and depth estimation schemes devised by *Pearce (1980)* who also tried to match the various depth phases with amplitude limits obtained from measurements made on seismic records. Our approach differs from his in that we can use the whole seismograms automatically without manual measurements; we also utilize the polarities of phases, but without trying to determine them subjectively, and that we can, in addition, incorporate any

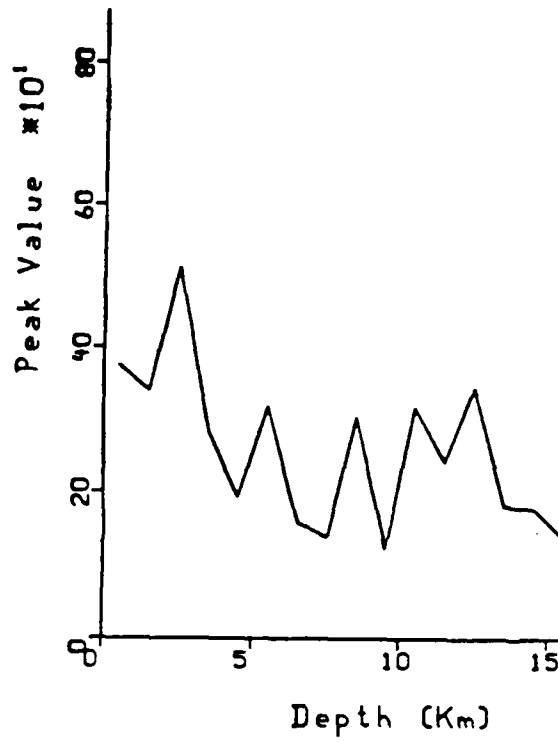


Figure 27. Shumway's statistic as a function of depth computed from deconvolved P wave seismograms of the December 25, 1975 Kazakh event.

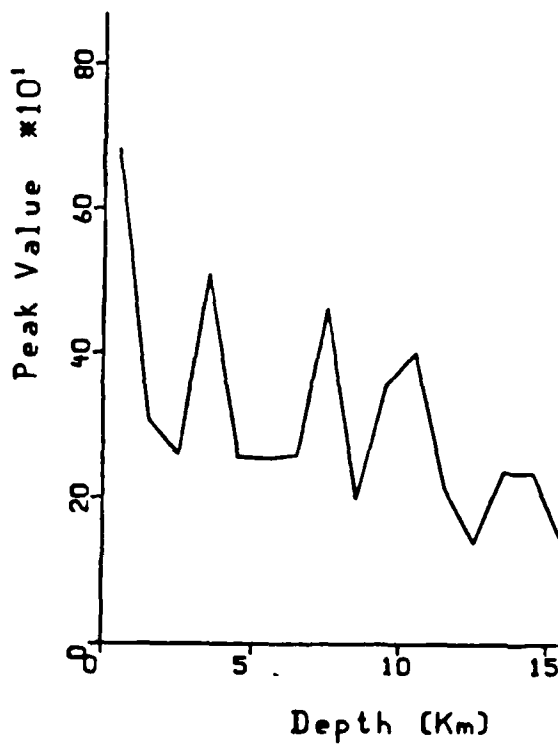


Figure 28. Shumway's statistic as a function of depth computed from deconvolved P wave seismograms of the June 29, 1977 Kazakh event.

available knowledge of crustal structures, no matter how complex, into the scheme by using them to compute the f vectors. The matching procedure will work in spite of any complexities in waveforms caused by non-impulsive source time functions. Our new standard method of discrimination will require that we line up the P waves on the first onset (the only manual step), invoke the best crustal response of the source region and match these against sets of f 's computed for explosion sources at various depths in that structure. In more general crustal structures, complexities not explainable to simple depth phases will also be present, and these can also be matched. Good matches (high F values) will designate explosions, poor matches, various crustal earthquakes (because the mismatches in the amplitudes and polarities of the various arrivals, mostly of the depth phases). Deconvolution is not needed for the success of the scheme, because common frequency factors cancel in the process; on the other hand, corrections for unequal path attenuation or instrument responses will be required. Reduction of site effects by array averaging is desirable prior to this process, but does not seem to be absolutely necessary if many stations are being used. Crustal structures have been the subject of studies over many decades and have been mapped all over the world. A data base of such structures could be a good accessory to intelligent monitoring systems.

Analysis of the August 7, 1966, El Golfo Earthquake

In order to apply our algorithm to real data, we tried to find some simple event that would be easy to model and match. To avoid computing and correcting for site effects, we decided to use long period data, where such effects can be neglected, at least in the first approximation. The El Golfo earthquake was reported to be a simple point source, a strike slip event found to be at 10 km depth by *Ebel et al (1978)*. The source time function was estimated to be a simple triangle of 4 sec duration in the same study, and the t^* along the

paths to the receiving stations recording on WWSSN 15-100 LP instruments was assumed to be 1.3 sec. We adopted fault orientation and the crustal model given in the same paper and used Shumway's formula in an attempt to verify the depth estimate using the P wave data.

The Green's functions (f vectors) were calculated by using an adaptation of the formulation of body wave radiation from a point source given by *Douglas et al (1971)* generalized to a flat-layered source crust model. The computer program in question, named PSV, was written by the first author of this report during the early seventies. The synthetic seismograms generated (Figure 29) are very close to the ones given in the paper by *Ebel et al (1978)*. We attribute some small, occasional differences to the fact that while our program automatically includes all rays in the source crust, the program used by *Ebel et al* needs the specification of all rays desired (*Langston, 1976*); thus, some less important rays may have been omitted in the calculations of *Ebel et al*. In any case, the synthetic waveforms we have generated are matching the data just as well as those of *Ebel et al*. We must note, however, that we do not consider these fits very good; they are worse than those used for computing the coherences in Figure 18.

The long period P waveforms to be processed were obtained by digitizing the enlarged seismograms from the paper on a high resolution digitizing tablet. Compared to the sizes of the mismatches between synthetics and data, the digitizing errors and trace distortions must be very small and inconsequential, and should not affect the conclusions of this test. In order to eliminate the absolute times as a factor in the matching procedure (if we had known the absolute times, properly corrected for mantle heterogeneity, we could have obtained the depth from those alone), we have lined up both the synthetics and the data on the first P arrival. We assumed, first, that the relative amplitudes are appropriate to

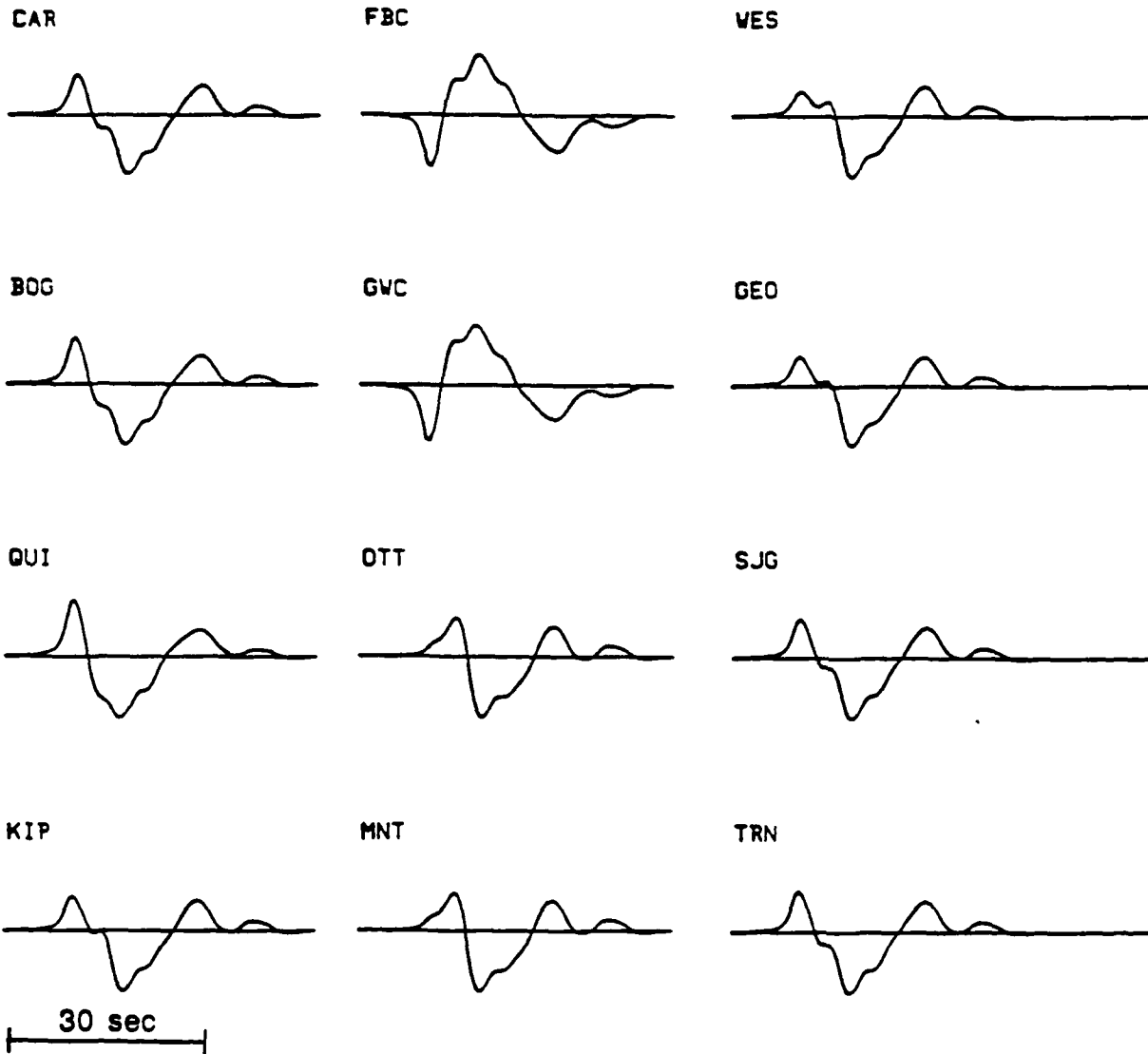


Figure 29. Synthetic seismograms appropriate to 10km depth for the El Golfo earthquake.

the radiation patterns in both the synthetics and the data in the paper. We have also made computations normalizing both the data and synthetics to unit maximum amplitudes. In the latter case we used all the data traces with equal weight, which is justifiable since the background noise is small and the traces with small amplitude carry just as much information about the source as the ones with larger amplitudes. In fact, some of these, recorded at the stations OTT and WES, were crucial in the original study in constraining the fault planes.

We have made two test runs while varying the source depth, fitting the spectral matrix structures in the .02 to .15 Hz band, using all frequencies with equal weight. In the first we matched the data with the source crustal responses to sources at different depths; in the second we matched the synthetic seismograms for 10 km depth with source crustal responses at other depths. As one would expect, the latter resulted in a maximum of the statistic at 10 km depth. The data, on the other hand, do not fit a source at 10 km depth when we apply the same procedure to them. The broadband fits, with and without normalization, seem to require a depth near 14 km (Figures 30 and 31). This is not much of a difference, but it is considerably outside of the 2 km accuracy limits claimed by *Ebel et al (1978)* for their solution. Despite the fact that the original El Golfo earthquake study also utilized some additional data, a limited amount of SH and surface wave data, we do not believe that the inclusion of these would have changed our results or conclusions. We prefer our own solution, because it is based on a broadband fit, and because it is based solely on the structure of the data spectral matrix, without tradeoffs against the source time functions and associated parameters that may occur in global waveform modeling, but which are factored out in our procedure. It is gratifying to find, however, that we were able to obtain a solution in the frequency domain for a mid-crustal event similar to those found by other, more detailed studies. Nevertheless, the task of testing the statistical

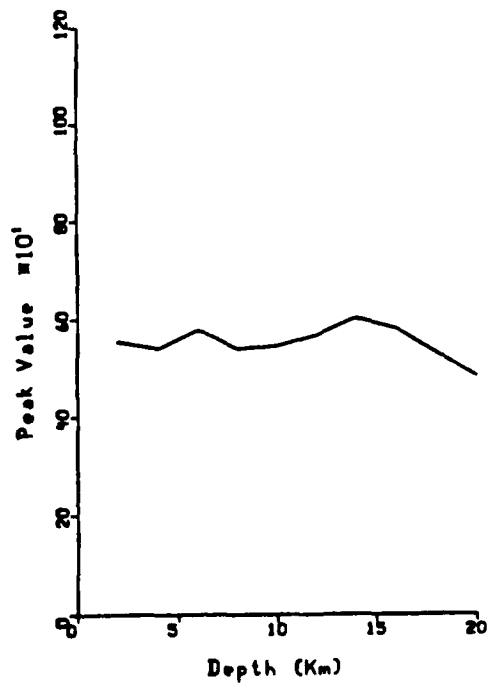
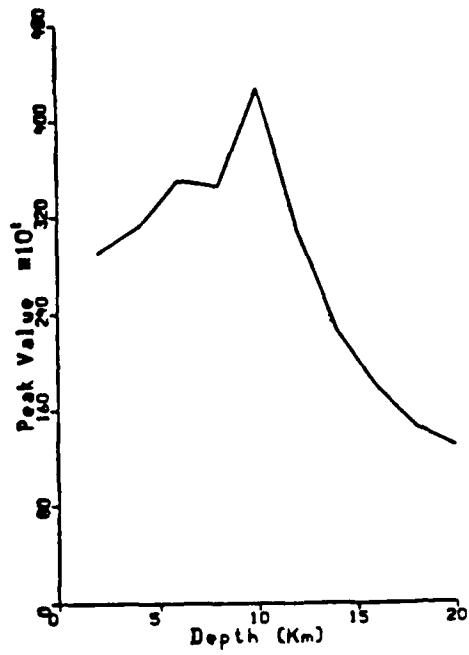


Figure 30. Shumway's statistic for the synthetic seismograms (top) and the long period P wave data for the El Golfo earthquake (bottom) as functions of depth. Trace amplitudes were not normalized.

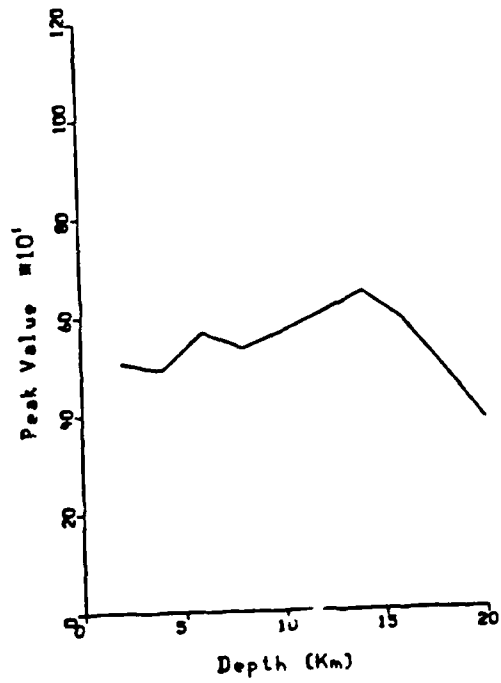
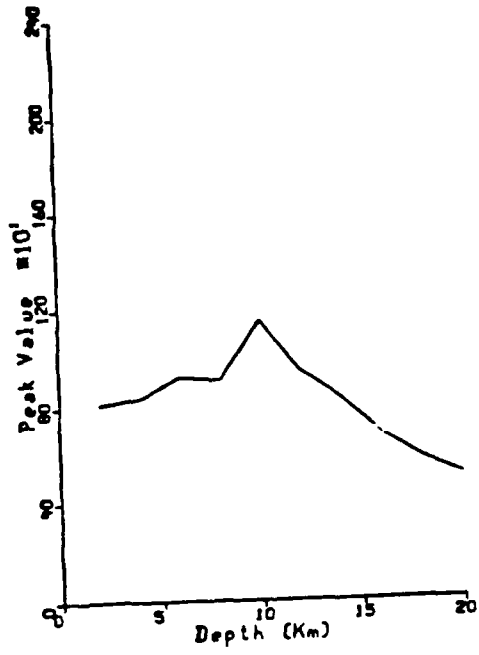


Figure 31. Shumway's statistic for the synthetic seismograms (top) and the long period P wave data for the El Golfo earthquake (bottom) as functions of depth. All trace amplitudes were normalized to unity.

significance of this difference still remains to be done. The sizes of differences between the depth estimates obtained by visual fitting of time domain waveforms and our broadband procedure are not surprisingly large in view of the simulations shown earlier in this report.

Analyses of Surface Waves From Kazakh Nuclear Explosions

During this phase of the work we have collected surface wave recordings of Kazakh nuclear explosions at common stations using the data bases at the Center for Seismic Studies. We have collected surface wave data for nine Kazakh explosions which were recorded at five common stations ANTO, GRFO, MAT, TATO and KONO. The first test was to verify that the events gave maxima near to their actual locations. This was found to be the case for several of them. In Figure 32 we show the maps of Capon's statistics obtained by using the event with the smallest tectonic release, lowest Love wave energy, as a master event defining the f vector. This seems to confirm the findings of *von Seggern (1972)*, who was able to locate events relative to each other with surface waves with about a 10 km accuracy. However, some other events did not locate well at all. Upon examining the data, we have found that the absolute times given in the data base were grossly in error for at least two of the traces. Further inquiries revealed that people who had used the data before (Richard Baumstark for instance) also experienced problems with the absolute times in some of the CSS data bases. While gross errors are easy to notice, smaller errors may go unnoticed and can make any results questionable. Therefore, we decided that we need to verify absolute times for all records we shall use in the future before we attempt anything like the separate estimation of compressional and deviatoric source energy.

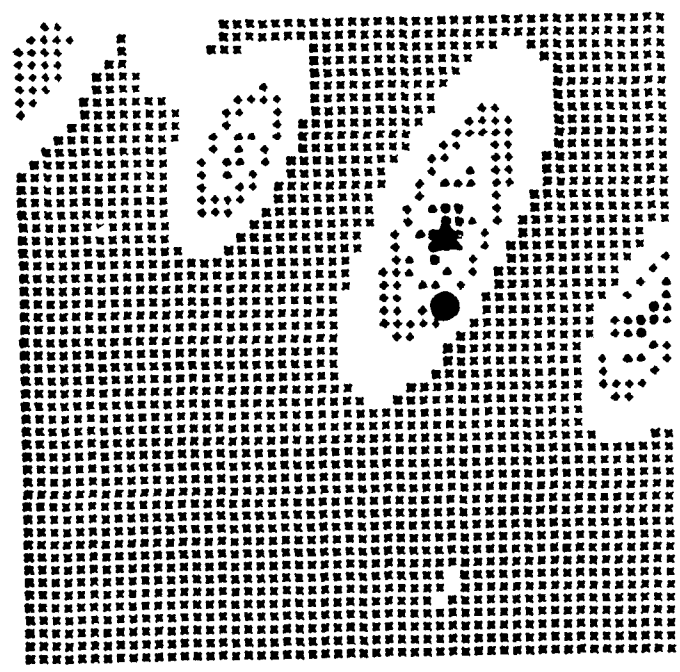
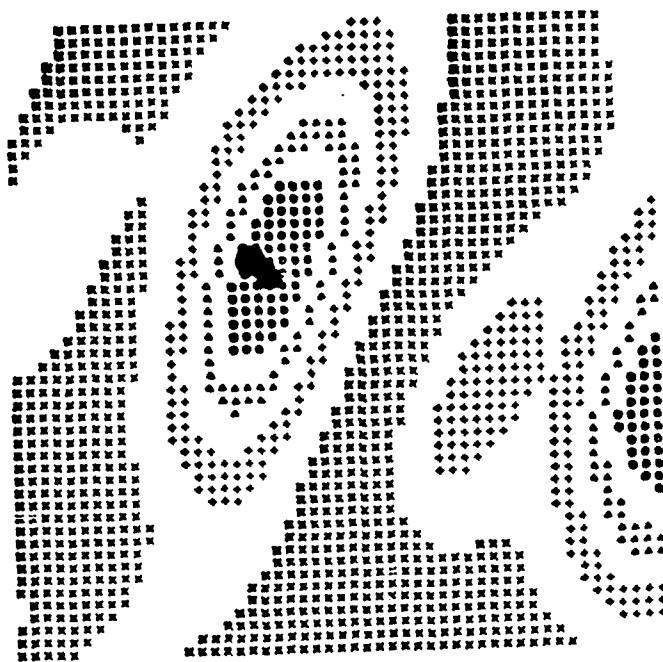


Figure 32. Location results obtained by imaging surface waves for two Kazakh explosions (October 12, 1980 on top and September 14, 1980 on the bottom) by the Capon algorithm. The geographical coordinates of the centers of the print plot grids are 50N-79E and the events are plotted relative to that. Filled circles denote the locations, obtained from body waves, as listed by unclassified files at the Center for Seismic Studies, triangles show the maxima of the Capon's statistics. The grids are 50 km on each side, and the tops are facing North.

ADAPTIVE FILTERING STUDIES

GENERAL REMARKS

In applying discrimination and yield estimation procedures to measurements made on various teleseismic and regional wave arrivals emitted by the sources, it is important to extend the ranges of detectability and measurability. Commonly, large events will excite body waves, Lg , and long period surface waves that can be seen teleseismically. Smaller events will not have long period surface waves that can be seen above the noise at teleseismic distances, but will still have detectable P waves. Events that are even smaller, t , can be detected only by regional stations and arrays. With decreasing magnitude, the quantity and quality of measurements used as discriminants and yield estimators will also decrease. Therefore, we need techniques that extend the ranges of detectability of various weak arrivals and that enable us to extract broadband information from the data. A family of such techniques can be loosely characterized as adaptive filtering methods. A common trait of many of these is that they were designed to suppress noise while passing coherent signals without distortion (*Booker and Ong, 1971; Shen, 1979*).

Adaptive filtering of array data was performed previously by *Shen (1979)*, who applied maximum-likelihood adaptive filters to short period teleseismic P waves at small arrays. He found that the noise reduction exceeded that of the conventional beamforming. The filters were designed on the basis of perfect similarity of seismic signals. This assumption is not correct for most arrays, as we have pointed out above. Therefore, we have investigated the effect of increasing the signal similarity by factoring out the site responses prior to applying the technique. The factoring out of site responses will, of course, change the noise coherence structure also, but we rely on the adaptation of the filter

to adjust to this changed structure. After removing the site responses, we can assume with more justification that the signals are perfectly coherent. This will reduce the "beam-loss" to much lower levels.

TELESEISMIC P WAVES FROM KAZAKH RECORDED AT EKA

For testing this approach, we have used recordings of a set of Kazakh (Shagan River) P waves recorded at EKA and estimated the site effects by applying our deconvolution procedure to the seismograms listed in Table IV. Subsequently, we factored out the site effects and applied Shen's algorithm to the result. In order to test the effect of the algorithm on the noise alone, we have applied the noise-adaptive filter to the noise preceding the signals. We performed this test on noise samples with and without the site

**TABLE IV - LIST OF KAZAKH EVENTS
RECORDED AT AWRE EKA ARRAY**

Event	Origin Time	Lat (N)	Lon (E)
1978241	04:26:75.9	49.82	78.14
1978162	02:56:57.6	49.90	78.80
1977334	04:06:57.4	49.96	78.89
1976342	04:56:57.4	49.96	78.85

effect correction. Figures 33 to 35 show that noise adaptation reduces the noise amplitudes relative to the conventional beam throughout the frequency range of 0-4 Hz, but the noise reduction is most effective below 1 Hz. The removal of site effects did not impair the effectiveness of noise-adaptation. The filter adapts quickly (as evidenced by a few large oscillations in the output after the noise amplitude falls off).

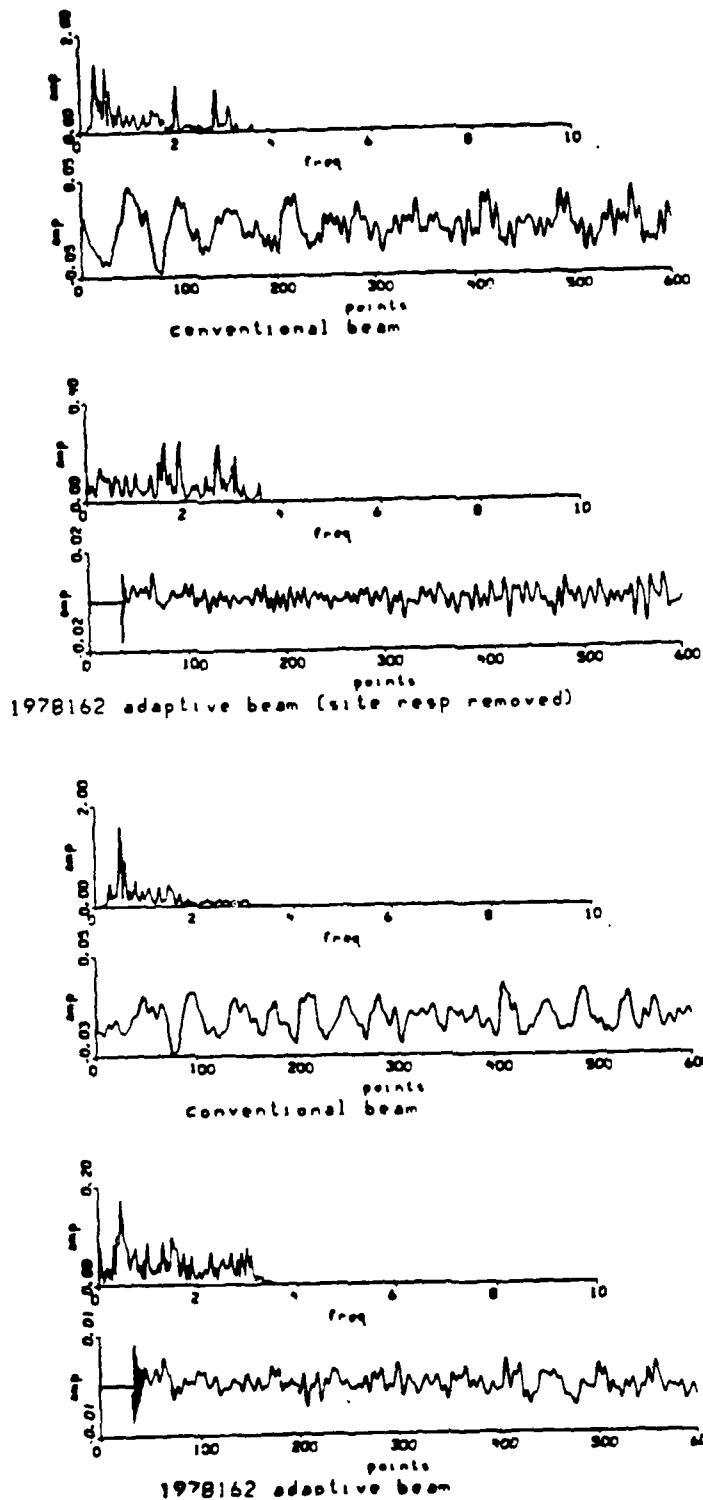


Figure 33. Comparisons of noise adaptation without (bottom) and with (top) the site response removed. Comparing the shapes and levels of spectra, it can be seen that the overall noise is significantly reduced by the adaptive beaming method relative to the beams, especially below 2 Hz. The adaptive beams quickly adapt to the noise, and after a few oscillations the overall noise levels are much reduced relative to the beam outputs.

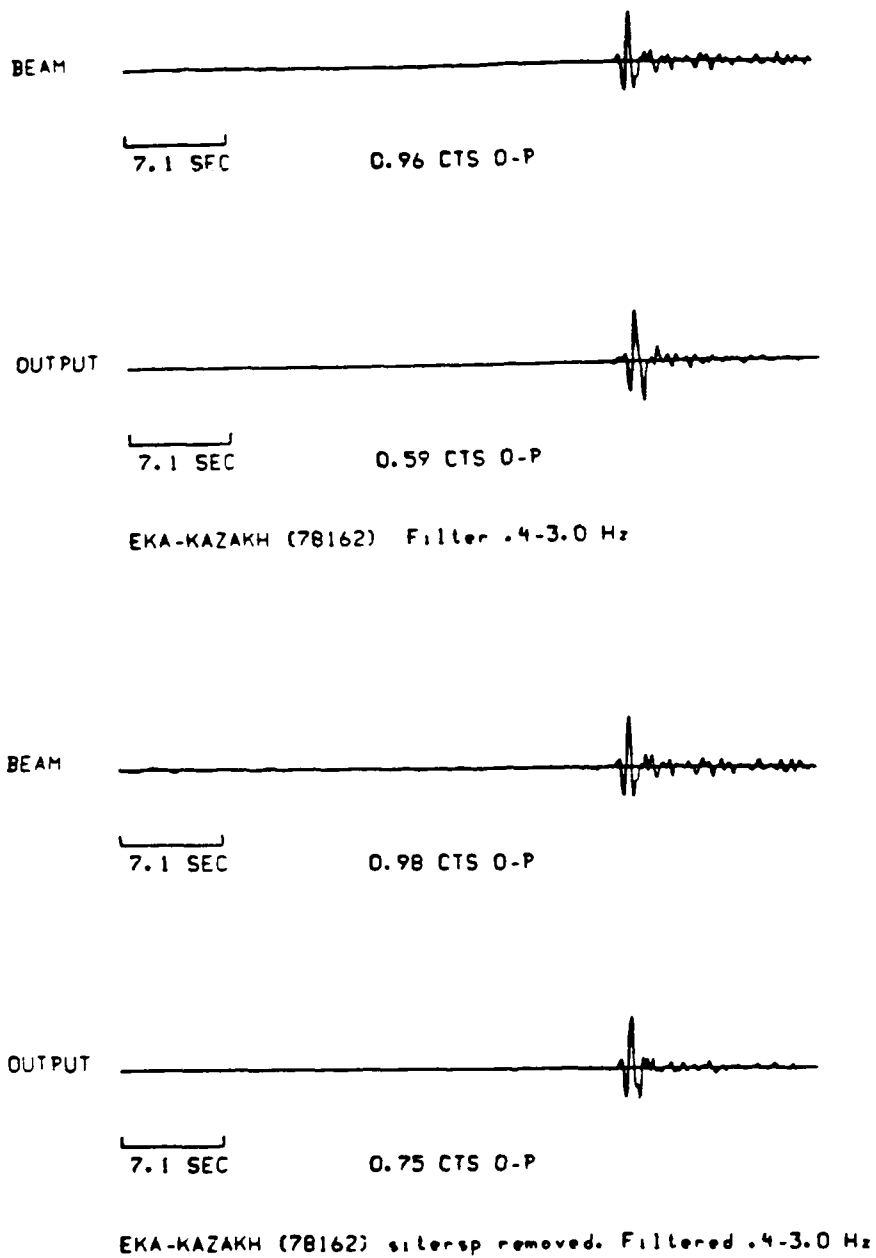


Figure 34. Teleseismic P waves processed by beaming and adaptive filtering with and without removal of site frequency responses.

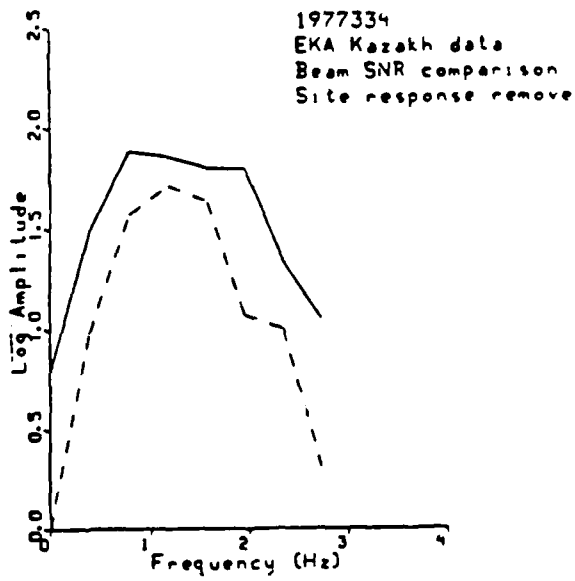
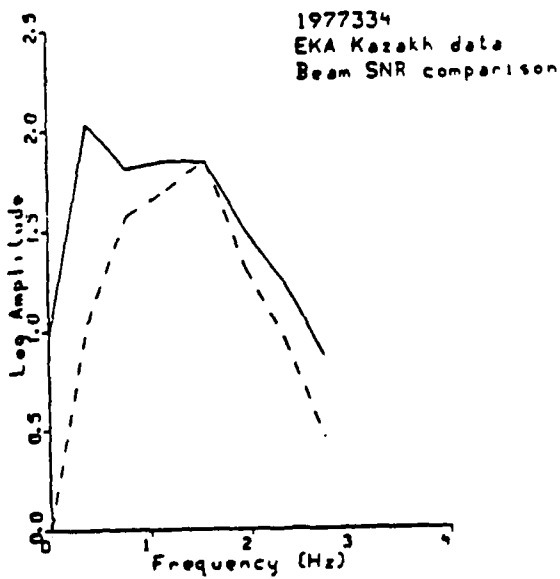
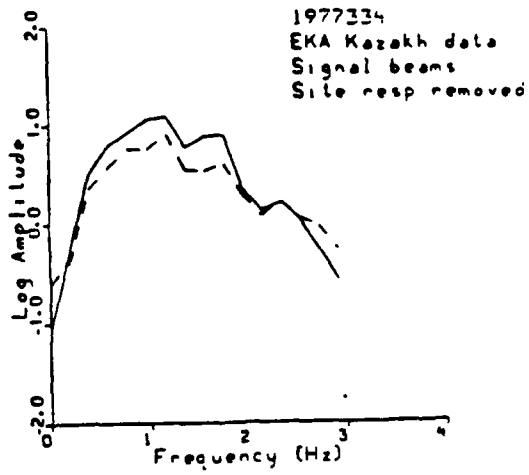
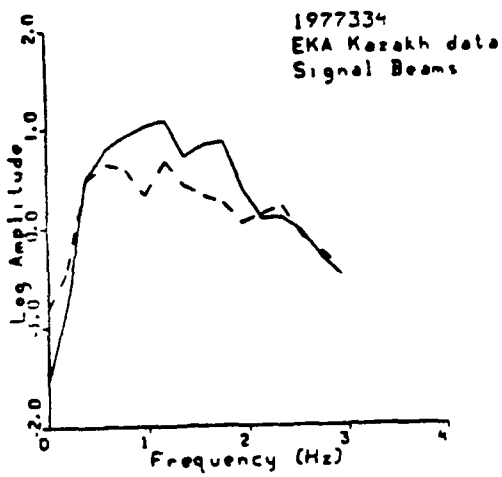


Figure 35. Spectra representative to the signal beam loss (top) and the S/N gain obtained for the two events by using the four modes of processing described in the text.

Applying the process to windows containing signals shows that the noise was reduced to a level below visibility in this high S/N sample by the adaptive process, while the noise is clearly visible on the beams (top traces in Figure 34). Obviously, this example has no practical use, since the signal is much larger than the noise in the case shown. It must be pointed out, however, that the relative noise reduction is the same regardless of the relative signal size (the site-equalized process will be unaffected by the presence of large coherent signals). Thus, a weaker signal would have stood out much better on the trace processed by the same procedure than on the beam and the result would be much better suited for any further analyses of the signal.

It is also interesting to look at these noise reduction results in the frequency domain. In Figure 34 we show the differences in the output on signal windows when the adaptive beam algorithm is applied with and without site effect correction. The figure shows that without the site effect correction the signal output is considerably less with adaptive beaming than with conventional beaming (a). This is not surprising, since the adaptive beam process will reduce the signal output if the signals are not matched. After site-equalization is performed, this signal loss is much less severe (b). Since the noise reduction of adaptive beaming remains more effective, even after applying site-equalization, than the conventional beam, the resulting overall S/N ratio improvement will be better for the adaptive beam combined with site-equalization (Figure 35). Thus, this combined process appears to be superior to the conventional beaming process. The gain is achieved at a considerable expense in processing complexity, but it may be justified in special cases when we want to learn more about smaller events at teleseismic distances. Such procedures may be part of a toolbox for more detailed investigations.

WESTERN NORWAY EARTHQUAKES RECORDED AT NORESS

Similarly to teleseismic signals, we have done a limited amount of work testing the suitability of adaptive beaming and site-equalization methods for enhancing regional P_n arrivals. P_n arrivals are generally emergent at regional distances and are much smaller in amplitude than Lg or S_n . Enhancing P_n arrivals may be quite useful in discrimination studies. The methodology followed is identical to that described for teleseismic P elsewhere in this report. The method was tested using a set of P_n arrivals from western Norway earthquakes. A list of these events is given in Table V. The site effects were estimated from applying the factorization procedure using the multi-channel deconvolution program (*Der et al, 1987*). Applying the adaptive beaming program to the noise alone (Figure 36) shows that the site response removal somewhat degrades the relative performance improvement due to the adaptive beaming process. On the other hand, the decrease in signal loss through the process appears to compensate approximately for this loss. The net result is that the best strategy seems to be to apply adaptive (not conventional) beaming either with or without site corrections. We must add that this test was done before we realized the extreme sensitivity of site factors to azimuth, and the western Norway earthquakes may be too scattered in azimuth to get stable and effective site correction factors. In any case, the adaptive beaming process appears to be better than conventional beaming for regional signals.

**TABLE V - LIST OF WESTERN NORWAY EVENTS
RECORDED AT NORESS**

Event	Origin Time	Lat (N)	Lon (E)
1985217	17:42:58.7	59.3	6.59
1985218	17:50:07.9	59.3	6.95
1985290	10:00:00.4	59.3	6.95

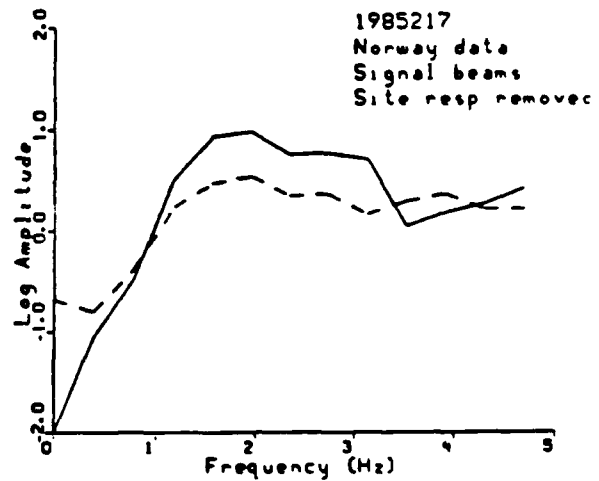
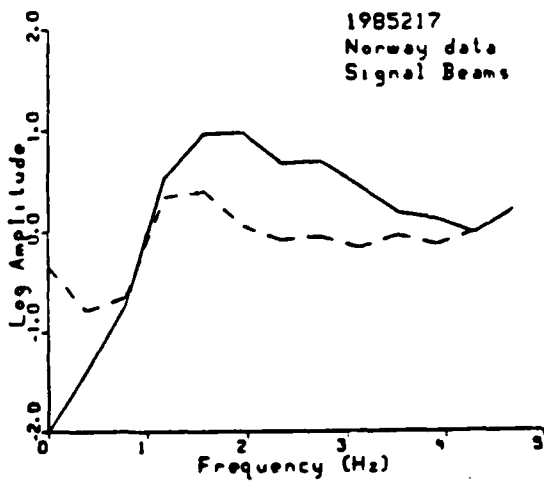
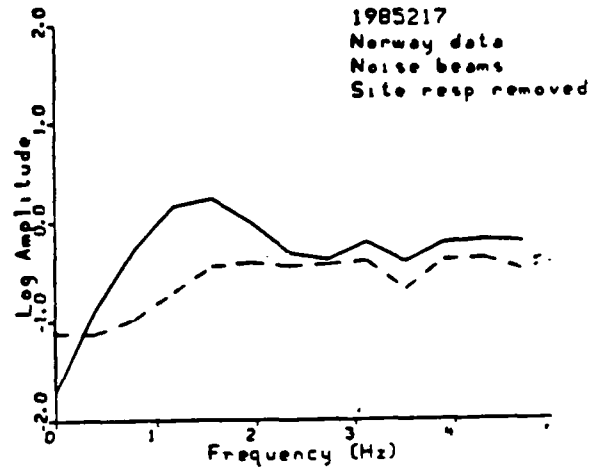
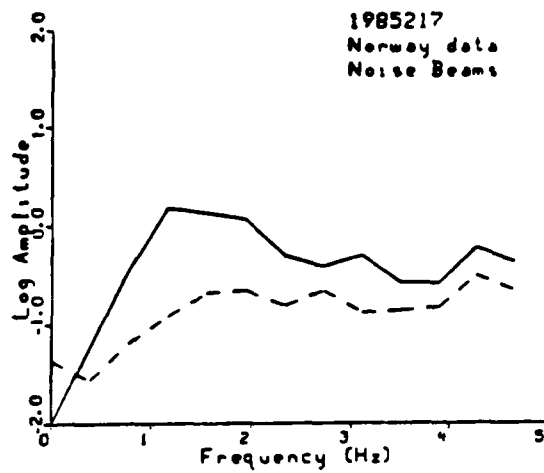


Figure 36. Figures illustrating the noise reduction gain and beam loss for western Norway earthquakes as processed by beaming and adaptive filtering with and without removing the site transfer functions.

FUTURE WORK

During the remaining part of this contract, we plan to apply the various techniques we developed to real data on a large scale; little, if any, theoretical or code development is planned. In particular:

Under the task of multi-channel analyses of regional data we plan to test our source analysis and azimuth finding approaches described in this report on a large number of quarry blast recordings depending on the data availability at NORESS, ARCESS, FINESA and GERESS. Since the acquisition of auxiliary information on quarry blasting practices has started by the NORSAR group, independent data will be available for verifying our results.

Under the task of seismic imaging we shall apply our techniques to body wave data of previously studied events, both earthquakes and explosions. We plan to apply the technique to progressively more difficult problems starting with events that have clear pP and sP arrivals. The images will be examined for signs of source finiteness and complexity. An automatized, interactive program package is being written that would enable us to apply our imaging technique for depth estimation and discrimination in a manner similar to the envisaged applications of Pearce's algorithm. This package can be a part of an operational discrimination system in the future.

We shall resume our work on surface wave imaging and investigating strain release phenomena. We concluded that our most recent efforts were severely degraded by the fact that numerous surface wave recordings in the CSS data bases had erroneous absolute times. We shall acquire more data for which we have accurate timing information.

CONCLUSIONS

Work during this reporting period revealed the great potential of various statistical-time series analysis methods for solving seismological problems relevant to nuclear monitoring.

In this exploratory study of regional seismic waveforms, extending the concept of spectral factorability of teleseismic body wave data (*Filson and Frasier, 1972*), we have demonstrated that spectra of regional phases can also be decomposed into source and recording site factors provided that the signals originated from a limited source region. Groups of events located close to each other can be identified by the fact that their waveforms can be reconstructed from their spectral source and site factors.

In addition, it was also found that events within such factorable groups could be further subdivided, according to relative interevent coherences between them. The events which show high inter-event coherence are probably both close to each other and have very similar source mechanisms, albeit different source time functions. The opposite must be true for events that do not show high coherence. Cross-event equalization filtering between coherent events using short time domain filters resulted in increases in waveform similarity, and no such increase seemed possible between events' pairs with low interevent coherence.

Site transfer functions between sensors located at the extreme ends of NORESS appear to be complex, describable only with transfer functions with impulse responses longer than a second. Assuming the same degree of crustal heterogeneity for a source region this may imply changes in waveforms similar in nature over small displacements of

source location. Further work needs to be done in exploring the nature of such transfer functions for

- a) Grouping events with respect to relative location;
- b) Identifying events with differing source mechanisms; and
- c) Finding differences in the source time functions between closely spaced events.

We have derived some new approaches for imaging seismic sources and seismic source inversion. The methods are based by finding the maxima of statistics that are closely related to those used in F-K analyses as functions of source parameters. The method is quite general, and can be used for analyzing both body and surface waves. These algorithms also provide a means for evaluation of the performance of time domain direct modeling and source inversion methods as currently practiced. Our analyses indicated that the time domain fits using long period data are generally not precise enough to resolve the source depth to a few km and other spatial details with the accuracies often claimed. This casts doubt on many results in the literature. Other simulations indicated that the same approaches can create reasonably resolved images of faults and can be used for the separate estimation of compressional and strain release components of energies from explosions.

Our source imaging-inversion methodology was applied to two deconvolved Kazakh nuclear explosions and the El Golfo Earthquake in order to obtain depth estimates. The method identified both explosions as shallow, with depths below 5 km, and the depth estimate for the El Golfo event turned out to be 14 km. These are reasonable results indicating that these methods can be applied for seismic discrimination. Imaging Kazakh

explosion sources using surface waves were hampered by demonstrably erroneous absolute timing information in the CSS data we retrieved.

Applications of combined adaptive filtering and site-effect compensation processing schemes to teleseismic (UK array) and regional (NORESS) data indicated that such methods can significantly enhance the signal-to-noise ratios for P (P_n) arrivals should such computer-intensive analyses prove to be desirable for an event.

REFERENCES

- Aki, K. and P.G. Richards (1980). *Quantitative Seismology*. W.H. Freeman & Co., San Francisco.
- Anderson, D.A. and B.W. Stump (1989). Seismic wave generation by quarry blasts. In "Quantification of explosion source characteristics fro near source, regional and teleseismic distances.", Southern Methodist University, GL=TR-89-0194, ADA216218.
- Baggeroer, A.B., Kuperman, W.A. and H. Schmidt (1988). Matched-field processing: Source localization in correlated noise as an optimum parameter estimation problem. *J. Acoust. Soc. Am.*, **83**, 571-587.
- Baumgardt, D.R. and K.A. Ziegler (1988). Spectral evidence for source multiplicity in explosions, application to regional discrimination of earthquakes and explosions *Bull. Seism. Soc. Am.* **78**, 1773-1795.
- Bendat, J.S. and A.G. Piersol (1966). *Measurement and Analysis of Random Data*. John Wiley & Sons.
- Booker, A. and C-Y. Ong (1971). Multiple constraint adaptive filtering. *Geophysics*, **36**, 498-509.
- Brillinger, D.R. (1985). Maximum likelihood approach to frequency-wavenumber analysis. *IEEE Trans. ASSP*, **33**, 1076-1085.
- Capon, J. (1969). High resolution frequency-wavenumber analysis. *Proc. IEEE*, **57**, 1408-1412.
- Cox, H. (1973). Resolving power and sensitivity to mismatch of optimum array processors. *J. Acoust. Soc. Am.*, **54**, 771-785.
- Der, Z.A., Lees, A.C., Chan, W.W., Shumway, R.H., McLaughlin, K.L., Smart, E., McElfresh, T.W. and M.E. Marshall (1987). Maximum-likelihood multichannel deconvolution of P waves at seismic arrays. *TGAL-87-3*, Teledyne-Geotech Alexandria Laboratories, Alexandria, VA.
- Der, Z.A., Shumway, R.H. and A.C. Lees (1987). Multi-channel deconvolution of P waves at seismic arrays. *Bull. Seism. Soc. Am.*, **77**, 195-211.
- Der, Z.A., Shumway, R.H. and A.C. Lees (1988). Frequency domain coherent processing of regional seismic signals at small arrays. *Bull. Seism. Soc. Am.*, **78**, 326-338.
- Douglas, A., Hudson, J.A. and V.K. Kembavi (1971). The relative excitation of seismic surface and body waves by point sources. *Geophys. J. R. Astr. Soc.*, **23**, 451-460.
- Ebel, J.E., Burdick, L.J. and G.S. Stewart (1978). The source mechanism of the August 7, 1966 El Golfo earthquake. *Bull. Seism. Soc. Am.*, **68**, 1281-1292.

- Wilson, J. and C.W. Frasier (1972). Multi-site estimation of explosive source parameters. *J. Geophys. Res.*, **77**, 2045-2061.
- Goldstein, P. and R.J. Archuleta (1987). Array analysis of seismic sources using Green's functions (Abstract). *EOS*, **68**, 13458.
- Hogg, R.V. and A.T. Craig (1978). *Introduction to Mathematical Statistics*. MacMillan Publishing Company.
- Ingate, S.F., Husebye, E.S. and A. Christofferson (1985). Regional arrays and optimum data processing schemes. *Bull. Seism. Soc. Am.*, **75**, 1155-1177.
- Kvaerna, R. and S. Mykkeltveit (1986). Optimum beam deployment for NORESS P-wave detection. In *NORSAR Semiannual Technical Summary*, L.B. Loughran Editor, 1 April-30 September 1985, No. I-86/87, 61-76.
- Langston, C.A. (1976). Body wave synthesis for shallow earthquake source: Inversion for source and earth structure parameters. *Ph. D. Thesis. California Institute of Technology*.
- Marple, S.L. (1987). *Digital Spectral Analysis and Applications*. Prentice Hall Series on Digital Signal Processing.
- Marshall, P.D., Stewart, R.C. and R.C. Lilwall (1989). The seismic disturbance of 1986 August 1 near Novaya Zemlya: a source of concern? *Geophysical Journal*, **98**, 565-573.
- McLaughlin, K.L., Rivers, D.W. and M.A. Brennan (1983). Pearce focal sphere analysis of explosion and earthquake mechanisms. *TGAL-TR-83-4*, Teledyne-Geotech, Alexandria, VA.
- Mudholkar, G.S. and Y.P. Chaubey (1976). Approximations for the noncentral-F distribution. *Commun. Statis. Theor. Meth.*, *A(5)1*, 49-63.
- Mykkeltveit, S., Astebol, K., Doornbos, D.J. and E.S. Husebye (1983). Seismic array configuration optimization. *Bull. Seism. Soc. Am.* **73**, 173-186.
- Olson, A.H. and J.G. Anderson (1988). Implications of frequency-domain inversion of earthquake ground motions for resolving the space-time dependence of slip on an extended fault. *Geophysical Journal*, **94**, 443-455.
- Pearce, R.G. (1977). Fault plane solutions using relative amplitudes of pP and P. *Geophys. J. R. Astr. Soc.*, **50**, 381-394.
- Pearce, R.G. (1980). Fault plane solutions using the relative amplitudes of P and surface reflections: further studies. *Geophys. J. R. Astr. Soc.*, **60**, 459-487.
- Pearce, R.G. and R.C. Stewart (1989). Interpretation of seismic pulse duration in terms of a propagating rupture: a method and case histories. *Tectonophysics*, **166**, 115-132.
- Rivers, D.W. and D.H. vonSeggern (1979). Random scattering effects on Rayleigh wave amplitudes and phases. *SDAC-TR-78-3*, Teledyne-Geotech, Alexandria, VA.

Shen, W.W. (1979). A constrained minimum power adaptive beamformer with time varying adaptation rate. *Geophysics*, **44**, 1088-1096.

Shumway, R.H. (1988). *Applied Statistical Time Series Analysis*. Prentice Hall.

Shumway, R.H. and Z.A. Der (1985). Deconvolution of multiple time series. *Technometrics*, **27**, 385-393.

Stevens, J.L. (1986). Estimation of scalar moments from explosion-generated surface waves. *Bull. Seism. Soc. Am.*, **76**, 123-151.

von Seggern, D.H. (1972). Relative location of seismic events using surface waves. *Geophys. J. Astr. Soc.*, **26**, 499-513.

Wallace, T.C., Helmberger, D.V. and G.R. Mellman (1981). A technique for the inversion of regional data in source parameter studies. *J. Geophys. Res.*, **86**, 1679-1685.

Widrow, B. (1966). Adaptive filters I: Fundamentals. Stanford Center for Systems Research. Systems Theory Laboratory, Stanford, CA.

Willis, D.E. (1963). A note on the effect of ripple firing on the spectra of quarry shots. *Bull. Seism. Soc. Am.*, **53**, 79-85.

APPENDIX A

SOURCE IMAGING: STATISTICAL THEORY

As we stated in the introduction of this report, one of the main goals of analysis of seismic data is to derive some properties of the source. In nuclear monitoring we desire to discriminate between events of various types, such as earthquakes and explosions, either through the direct discrimination of source mechanisms or indirectly through determination of the source depth. It would be desirable to do this by some visual identification of sources after some preprocessing. In conventional processing of P wave data such identification can be performed through lining up the short period P waves and observing the pP "moveout", i.e., the changes in pP time with the values of slowness. Alternatively, one may apply some criteria using amplitude measurements in some time windows covering possible times of depth phases to ascertain that an event belongs to either the earthquake or explosion category (*Pearce, 1980*). Although such methods are clearly useful, they are somewhat tedious, and some future automation of such approaches is clearly desirable. In a broader sense, going beyond the concept of point sources, detailed mapping of the sources of seismic radiation is also very important in studies of the mechanisms of earthquakes. In order to understand the faulting processes we need to know how the fault dislocation developed in time and space.

The discussion below establishes a proposed definition of the "source image", i.e., the estimated power of seismic sources as functions of space coordinates in the source region and derives confidence intervals for this image. We consider, as usual, the observed time vector $y(t)$ observed over N array elements or stations. The discrete Fourier transform of this can be written as

$$y = f s + n \quad (1)$$

where $s = s(x, \nu)$ is the Fourier transform of the theoretical signal at frequency ν and at source position vector x , usually specified as a combination of location and depth. The vector $f = f(x, \nu)$ is the transform of the function that combines with s to produce the data y . We can think of f as some combination of Green's functions. The vector f is assumed to be known, whereas the signal s is deterministic and unknown. The noise vector n is assumed to be spatially white (uncorrelated among stations) with power spectral matrix

$$E(n n^*) = P_n(\nu) I \quad (2)$$

at frequency ν , where $P_n(\nu)$ is the noise power spectrum of each channel and I is the identity matrix information carried by the observed vector y . One can simply plot the power in the generalized transform $f^* y$ as the beampower

$$B(x, \nu) = \frac{|f^* y|^2}{|f|^2} \quad (3)$$

An alternative measure with higher resolution is Capon's C , defined as

$$C(x, \nu) = \left[f^* (y y^* + c^2 I)^{-1} f \right]^{-1} \quad (4)$$

which can also be written in the form

$$C(x, \nu) = \frac{c^4}{|f|^2} \left(1 + \frac{B(x, \nu)}{(c^2 + |y|^2 - B(x, \nu))} \right) \quad (5)$$

which shows its relation to the generalized beam. It is convenient to define the residual power as

$$R(x, v) = |y|^2 - B(x, v) \quad (6)$$

so that

$$C(x, v) = \frac{c^4}{|v|^2} \left(1 + \frac{B(x, v)}{(c^2 + R(x, v))} \right) \quad (7)$$

the constant c is an arbitrary number chosen to make the matrix $(y y^* + c^2 I)$ non-singular.

A second alternative estimator is Shumway's F , defined as the likelihood ratio test statistic resulting from testing the model (1). This leads to

$$F(x, v) = (N - 1) \frac{B(x, v)}{R(x, v)} \quad (8)$$

which is closely related to the other two.

Capon's C and Shumway's F have similar resolving capabilities since they are both functions of B and R . They are both better than the generalized beampower from this point of view since Equation (3) does not incorporate the residual noise power R . We shall show below that the F is superior statistically to the other two, both for detecting the predefined signal and for providing an estimator for the signal image.

If the noise is Gaussian, it is easy to show that

$$\frac{2 B(x, \nu)}{P_n(\nu)} \sim \chi^2_2(\delta^2) \quad (9)$$

where χ^2_2 denotes the chi-squared distribution with non-centrality parameter

$$\delta^2 = \frac{2 |S(x, \nu)|^2}{P_n(\nu)} \quad (10)$$

and \sim is a notation for "approximately distributed as." Note that δ^2 is twice the "signal-to-noise" ratio

$$\xi^2(x, \nu) = \frac{|S(x, \nu)|^2}{P_n(\nu)} \quad (11)$$

It is this signal-to-noise ratio that we propose to define as the image. It is also easy to show that

$$\frac{2 R(x, \nu)}{P_n(\nu)} \sim \chi^2_{2N-2}(0) \quad (12)$$

and is independent of $B(x, \nu)$. It follows that

$$F_{2, 2N-2}(\delta^2) = \frac{\chi^2_2(\delta^2) / 2}{\chi^2_{2N-2} / (2N-2)} \quad (13)$$

so that

$$F(x, \nu) = (N - 1) \frac{B(x, \nu)}{R(x, \nu)} \quad (14)$$

has the non-central F distribution with the non-centrality parameter δ^2 given by Equation (11). Hence the distribution of F depends only on the signal-to-noise ratio $\xi^2(x, \nu)$ for a given number of sensors N .

We may examine this further by noting that for an F with n_1 and n_2 degrees of freedom

$$E(F_{n_1, n_2}(\delta^2)) = \frac{n_1}{n_2} \cdot \frac{1}{n_2 - 2} \cdot (n_1 + \delta^2) \quad (15)$$

so that

$$E(F(x, \nu)) = \frac{(N - 1)}{(N - 2)} (1 + \xi^2(x, \nu)) \quad (16)$$

and the mean value is essentially the signal-to-noise ratio.

$$E(F_{n_1, n_2}^2(\delta^2)) = \frac{n_2}{n_1} \frac{1}{(n_2 - 2)(n_2 - 4)} [2n_1 + 4\delta^2 + (n_1 + \delta^2)^2] \quad (17)$$

can be used to compute the variance with

$$\text{var}(F) = E(F^2) - E^2(F) \quad (18)$$

and $n_1 = 2$, $n_2 = 2N - 2$. The variance depends on the signal-to-noise ratio that we are trying to estimate in a rather complicated way and the normal approximation will not be very good for obtaining an approximate confidence interval.

For any x and v , however, we can obtain an exact confidence interval for $E(F(x,v))$, δ^2 or ξ^2 in the following way. We know from (16) that

$$\hat{\xi}^2(x,v) = \frac{(N-2)}{(N-1)} F(x,v) - 1 \quad (19)$$

is an unbiased estimator of the signal to noise ratio (11), which we are defining as the image. Let $F(x,v)$ be some observed sample value of Equation (14). Let δ^2_1 and δ^2_2 be two values of δ^2 such that

$$Pr \{ F_{2, 2N-2}(\delta^2_1) \leq F(x,v) \} = \alpha/2 \quad (20)$$

and

$$Pr \{ F_{2, 2N-2}(\delta^2_2) \leq F(x,v) \} = \alpha/2 \quad (21)$$

The resulting $1-\alpha$ confidence interval for δ^2 will be (δ^2_1, δ^2_2) . The interval for this signal-to-noise ratio is $(1/2 \delta^2_1, 1/2 \delta^2_2)$. This interval can also be connected into a $(1-\alpha)$ confidence interval for $E(F(x,v))$, using Equation (16).

The above procedure can be used to get a $(1-\alpha)$ percent confidence interval for each x and v . Since the intervals are dependent, for n of them one can only assign an overall confidence of $1-n\alpha$. Therefore, in order to assign small confidence to the upper and lower surfaces of, say, .90, with 100 points on the surface, each separate point should have $\alpha=.001$ or 99.9% confidence.

APPENDIX B

IMPLEMENTATION OF MULTI-CHANNEL DECONVOLUTION IN THE X-WINDOWS ENVIRONMENT

In order to facilitate the use and the testing of the multi-channel deconvolution method, we have written a version that makes use of the X-window environment. The program is menu-driven with the following options for viewing in the Multi-channel Deconvolution Display (MDD):

- 1) Source estimate waveforms and resolution kernels;
- 2) Site transfer function (time domain) displays;
- 3) Source spectral estimates;
- 4) Site response spectra; and
- 5) Original vs. reconstructed waveforms with associated correlation coefficients.

Examples of these various kinds of displays are shown in Figures B1 to B4. For further explanations we refer to the figure captions. When MDD is activated it creates a window and waits for user input. All input is entered by using a mouse. The right mouse button produces a menu of the options. The option is chosen by moving the mouse so that the desired option is highlighted and the left mouse button is pressed.

Once the option is chosen, a window displaying the desired data appears. If all the data will not fit the window, the first few waveforms will be displayed and the rest can be viewed by scrolling. A scrollbar appears at the left edge of each window. It can be used to scroll the data within that window by standard X11 scrollbar manipulations. Each new

window will be created on top of those currently displayed. All windows can be resized, moved and overlaid using standard X facilities.

Multichannel Deconvolution Display

press right button for menu

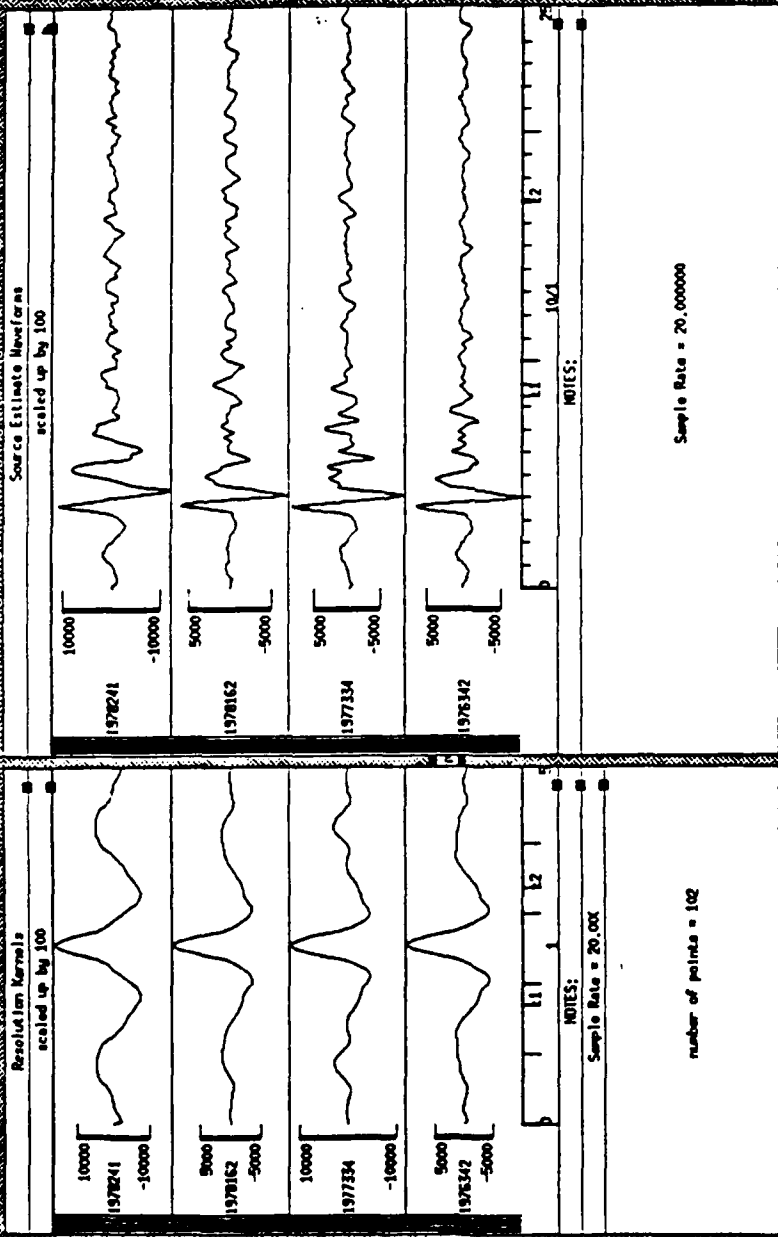


Figure B1. Display of source time function estimates with the estimated resolution kernels.

Multichannel Deconvolution Display

Press right button for menu

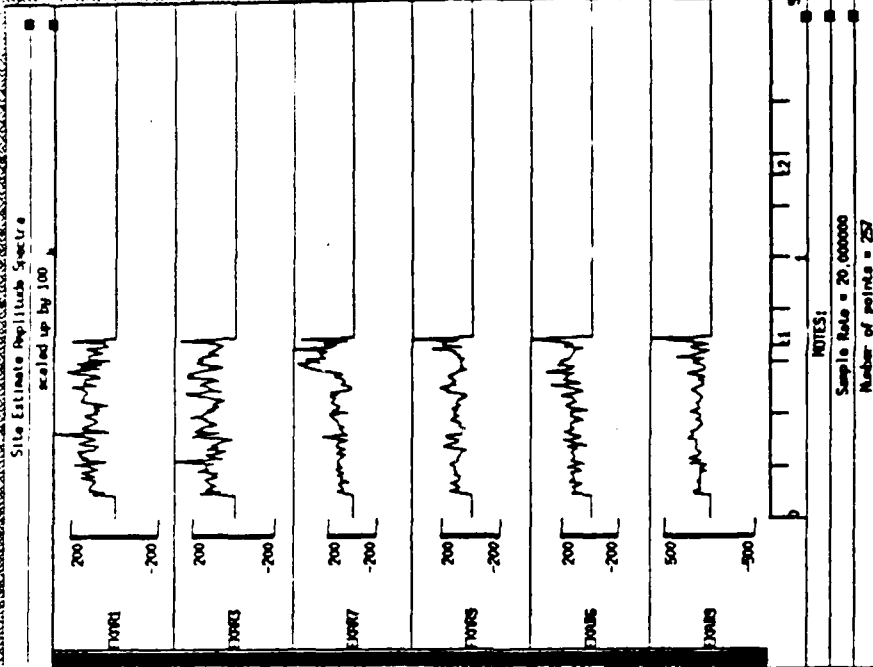
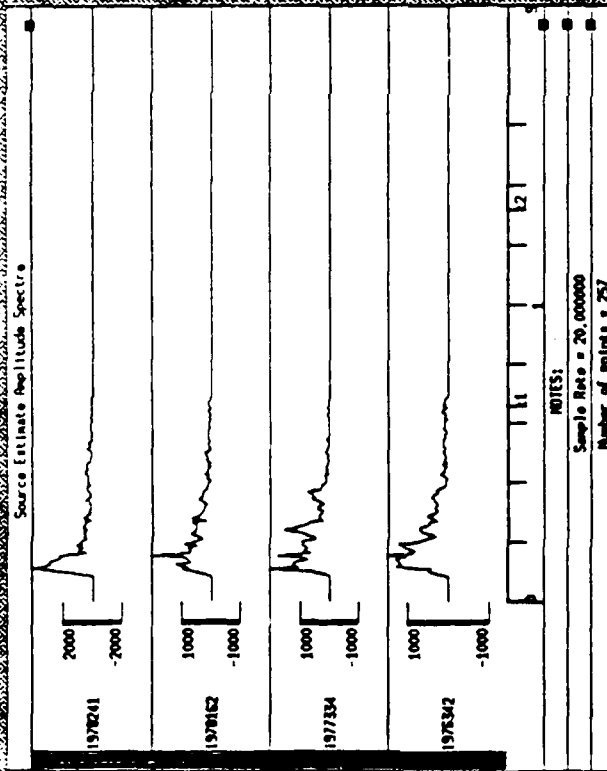


Figure B3. Joint display of source time function estimates and their spectra.

Multichannel Deconvolution Display

press right button for menu

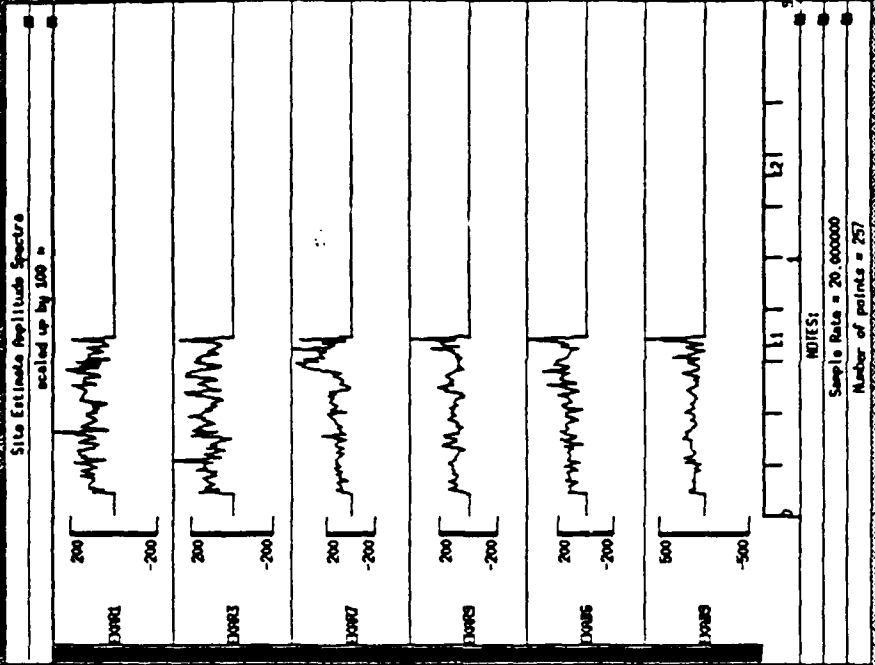
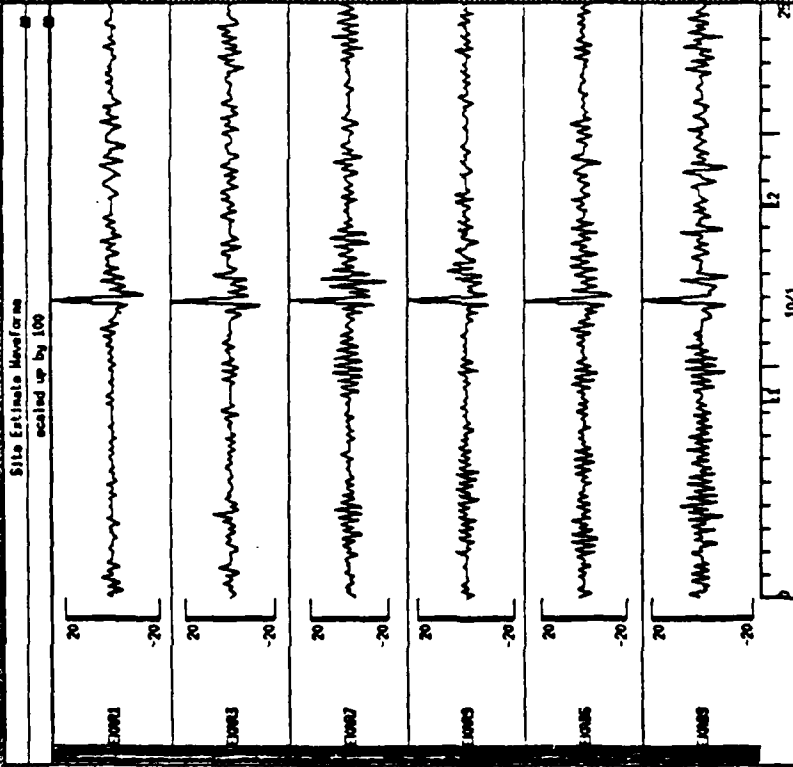


Figure B2. Display of time domain site transfer function estimates with their spectra.

Multichannel Deconvolution Display

press right button for menu

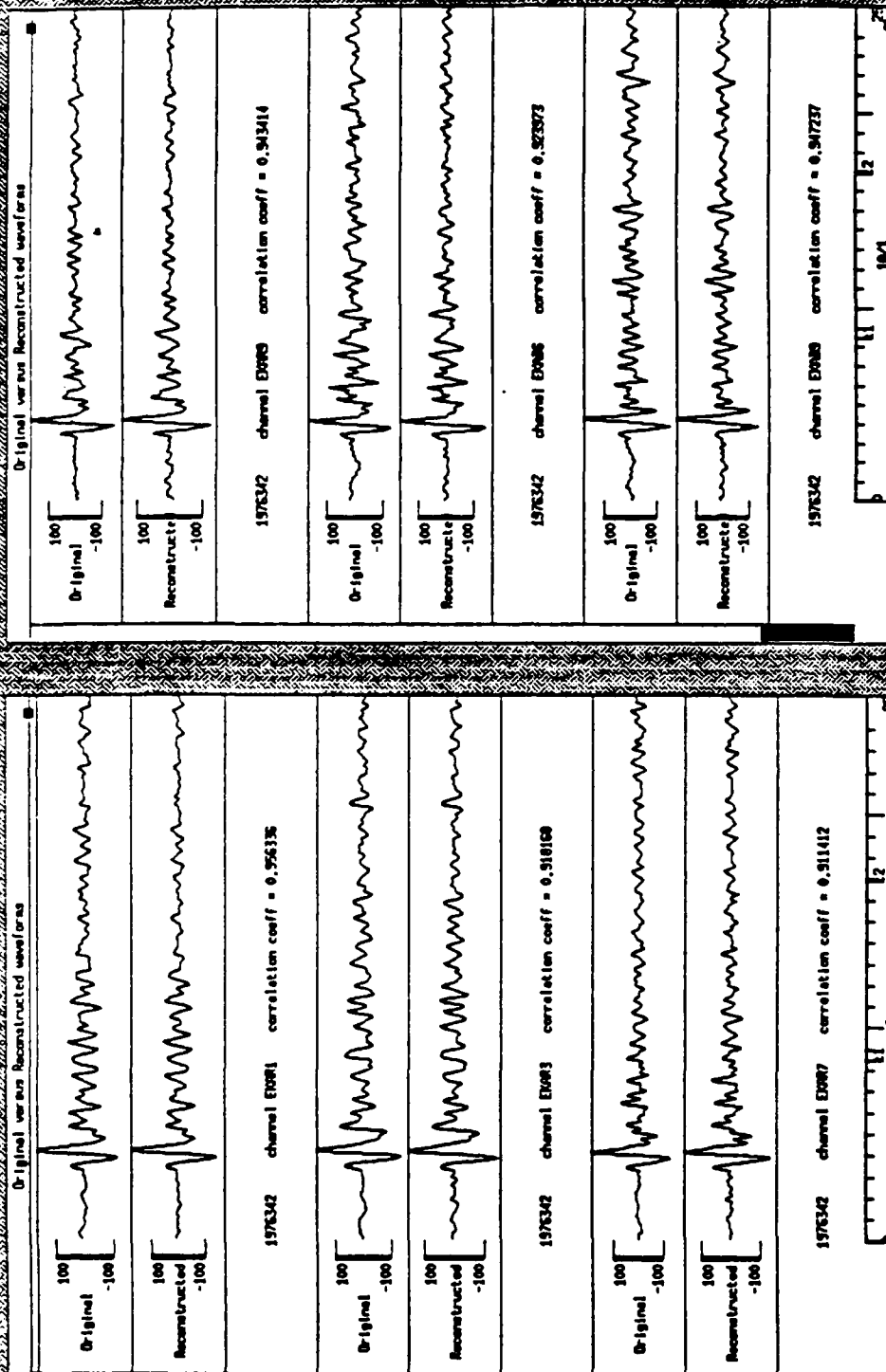


Figure B4. Displays comparing the data with their reconstructions from source and site spectral factors. The value of the time domain correlation coefficient is given for each pair of traces.

Contractors (United States)

Prof. Thomas Ahrens
Seismological Lab, 252-21
Division of Geological & Planetary Sciences
California Institute of Technology
Pasadena, CA 91125

Dr. Zoltan A. Der
ENSCO, Inc.
5400 Port Royal Road
Springfield, VA 22151-2388

Prof. Charles B. Archambeau
CIRES
University of Colorado
Boulder, CO 80309

Prof. John Ferguson
Center for Lithospheric Studies
The University of Texas at Dallas
P.O. Box 830688
Richardson, TX 75083-0688

Prof. Muawia Barazangi
Institute for the Study of the Continent
Cornell University
Ithaca, NY 14853

Prof. Stanley Flatte
Applied Sciences Building
University of California
Santa Cruz, CA 95064

Dr. Douglas R. Baumgardt
ENSCO, Inc
5400 Port Royal Road
Springfield, VA 22151-2388

Dr. Alexander Florence
SRI International
333 Ravenswood Avenue
Menlo Park, CA 94025-3493

Prof. Jonathan Berger
IGPP, A-025
Scripps Institution of Oceanography
University of California, San Diego
La Jolla, CA 92093

Prof. Henry L. Gray
Vice Provost and Dean
Department of Statistical Sciences
Southern Methodist University
Dallas, TX 75275

Dr. Lawrence J. Burdick
Woodward-Clyde Consultants
566 El Dorado Street
Pasadena, CA 91109-3245

Dr. Indra Gupta
Teledyne Geotech
314 Montgomery Street
Alexandria, VA 22314

Dr. Karl Coyner
New England Research, Inc.
76 Olcott Drive
White River Junction, VT 05001

Prof. David G. Harkrider
Seismological Laboratory
Division of Geological & Planetary Sciences
California Institute of Technology
Pasadena, CA 91125

Prof. Vernon F. Cormier
Department of Geology & Geophysics
U-45, Room 207
The University of Connecticut
Storrs, CT 06268

Prof. Donald V. Helmberger
Seismological Laboratory
Division of Geological & Planetary Sciences
California Institute of Technology
Pasadena, CA 91125

Professor Anton W. Dainty
Earth Resources Laboratory
Massachusetts Institute of Technology
42 Carleton Street
Cambridge, MA 02142

Prof. Eugene Herrin
Institute for the Study of Earth and Man
Geophysical Laboratory
Southern Methodist University
Dallas, TX 75275

Prof. Steven Day
Department of Geological Sciences
San Diego State University
San Diego, CA 92182

Prof. Robert B. Herrmann
Department of Earth & Atmospheric Sciences
St. Louis University
St. Louis, MO 63156

Prof. Bryan Isacks
Cornell University
Department of Geological Sciences
SNEE Hall
Ithaca, NY 14850

Dr. Rong-Song Jih
Teledyne Geotech
314 Montgomery Street
Alexandria, VA 22314

Prof. Lane R. Johnson
Seismographic Station
University of California
Berkeley, CA 94720

Prof. Alan Kafka
Department of Geology & Geophysics
Boston College
Chestnut Hill, MA 02167

Dr. Richard LaCoss
MIT-Lincoln Laboratory
M-200B
P. O. Box 73
Lexington, MA 02173-0073 (3 copies)

Prof Fred K. Lamb
University of Illinois at Urbana-Champaign
Department of Physics
1110 West Green Street
Urbana, IL 61801

Prof. Charles A. Langston
Geosciences Department
403 Deike Building
The Pennsylvania State University
University Park, PA 16802

Prof. Thorne Lay
Institute of Tectonics
Earth Science Board
University of California, Santa Cruz
Santa Cruz, CA 95064

Prof. Arthur Lerner-Lam
Lamont-Doherty Geological Observatory
of Columbia University
Palisades, NY 10964

Dr. Christopher Lynnes
Teledyne Geotech
314 Montgomery Street
Alexandria, VA 22314

Prof. Peter Malin
University of California at Santa Barbara
Institute for Crustal Studies
Santa Barbara, CA 93106

Dr. Randolph Martin, III
New England Research, Inc.
76 Olcott Drive
White River Junction, VT 05001

Dr. Gary McCartor
Mission Research Corporation
735 State Street
P.O. Drawer 719
Santa Barbara, CA 93102 (2 copies)

Prof. Thomas V. McEvelly
Seismographic Station
University of California
Berkeley, CA 94720

Dr. Keith L. McLaughlin
S-CUBED
A Division of Maxwell Laboratory
P.O. Box 1620
La Jolla, CA 92038-1620

Prof. William Menke
Lamont-Doherty Geological Observatory
of Columbia University
Palisades, NY 10964

Stephen Miller
SRI International
333 Ravenswood Avenue
Box AF 116
Menlo Park, CA 94025-3493

Prof. Bernard Minster
IGPP, A-025
Scripps Institute of Oceanography
University of California, San Diego
La Jolla, CA 92093

Prof. Brian J. Mitchell
Department of Earth & Atmospheric Sciences
St. Louis University
St. Louis, MO 63156

Mr. Jack Murphy
S-CUBED, A Division of Maxwell Laboratory
11800 Sunrise Valley Drive
Suite 1212
Reston, VA 22091 (2 copies)

Dr. Bao Nguyen
GL/LWH
Hanscom AFB, MA 01731-5000

Prof. John A. Orcutt
IGPP, A-025
Scripps Institute of Oceanography
University of California, San Diego
La Jolla, CA 92093

Prof. Keith Priestley
University of Cambridge
Bullard Labs, Dept. of Earth Sciences
Madingley Rise, Madingley Rd.
Cambridge CB3 0EZ, ENGLAND

Prof. Paul G. Richards
L-210
Lawrence Livermore National Laboratory
Livermore, CA 94550

Dr. Wilmer Rivers
Teledyne Geotech
314 Montgomery Street
Alexandria, VA 22314

Prof. Charles G. Sammis
Center for Earth Sciences
University of Southern California
University Park
Los Angeles, CA 90089-0741

Prof. Christopher H. Scholz
Lamont-Doherty Geological Observatory
of Columbia University
Palisades, NY 10964

Prof. David G. Simpson
Lamont-Doherty Geological Observatory
of Columbia University
Palisades, NY 10964

Dr. Jeffrey Stevens
S-CUBED
A Division of Maxwell Laboratory
P.O. Box 1620
La Jolla, CA 92038-1620

Prof. Brian Stump
Institute for the Study of Earth & Man
Geophysical Laboratory
Southern Methodist University
Dallas, TX 75275

Prof. Jeremiah Sullivan
University of Illinois at Urbana-Champaign
Department of Physics
1110 West Green Street
Urbana, IL 61801

Prof. Clifford Thurber
University of Wisconsin-Madison
Department of Geology & Geophysics
1215 West Dayton Street
Madison, WI 53706

Prof. M. Nafi Toksoz
Earth Resources Lab
Massachusetts Institute of Technology
42 Carleton Street
Cambridge, MA 02142

Prof. John E. Vidale
University of California at Santa Cruz
Seismological Laboratory
Santa Cruz, CA 95064

Prof. Terry C. Wallace
Department of Geosciences
Building #77
University of Arizona
Tucson, AZ 85721

Dr. Raymond Willeman
GL/LWH
Hanscom AFB, MA 01731-5000

Dr. Lorraine Wolf
GL/LWH
Hanscom AFB, MA 01731-5000

Prof. Francis T. Wu
Department of Geological Sciences
State University of New York
at Binghamton
Vestal, NY 13901

OTHERS (United States)

Dr. Monem Abdel-Gawad
Rockwell International Science Center
1049 Camino Dos Rios
Thousand Oaks, CA 91360

Prof. Keiiti Aki
Center for Earth Sciences
University of Southern California
University Park
Los Angeles, CA 90089-0741

Prof. Shelton S. Alexander
Geosciences Department
403 Deike Building
The Pennsylvania State University
University Park, PA 16802

Dr. Kenneth Anderson
BBNSTC
Mail Stop 14/1B
Cambridge, MA 02238

Dr. Ralph Archuleta
Department of Geological Sciences
University of California at Santa Barbara
Santa Barbara, CA 93102

Dr. Thomas C. Bache, Jr.
Science Applications Int'l Corp.
10210 Campus Point Drive
San Diego, CA 92121 (2 copies)

J. Barker
Department of Geological Sciences
State University of New York
at Binghamton
Vestal, NY 13901

Dr. T.J. Bennett
S-CUBED
A Division of Maxwell Laboratory
11800 Sunrise Valley Drive, Suite 1212
Reston, VA 22091

Mr. William J. Best
907 Westwood Drive
Vienna, VA 22180

Dr. N. Biswas
Geophysical Institute
University of Alaska
Fairbanks, AK 99701

Dr. G.A. Bollinger
Department of Geological Sciences
Virginia Polytechnical Institute
21044 Derring Hall
Blacksburg, VA 24061

Dr. Stephen Bratt
Science Applications Int'l Corp.
10210 Campus Point Drive
San Diego, CA 92121

Michael Browne
Teledyne Geotech
3401 Shiloh Road
Garland, TX 75041

Mr. Roy Burger
1221 Serry Road
Schenectady, NY 12309

Dr. Robert Burrige
Schlumberger-Doll Research Center
Old Quarry Road
Ridgefield, CT 06877

Dr. Jerry Carter
Rondout Associates
P.O. Box 224
Stone Ridge, NY 12484

Dr. W. Winston Chan
Teledyne Geotech
314 Montgomery Street
Alexandria, VA 22314-1581

Dr. Theodore Cherry
Science Horizons, Inc.
710 Encinitas Blvd., Suite 200
Encinitas, CA 92024 (2 copies)

Prof. Jon F. Claerbout
Department of Geophysics
Stanford University
Stanford, CA 94305

Prof. Robert W. Clayton
Seismological Laboratory
Division of Geological & Planetary Sciences
California Institute of Technology
Pasadena, CA 91125

Prof. F. A. Dahlen
Geological and Geophysical Sciences
Princeton University
Princeton, NJ 08544-0636

Prof. Adam Dziewonski
Hoffman Laboratory
Harvard University
20 Oxford St
Cambridge, MA 02138

Prof. John Ebel
Department of Geology & Geophysics
Boston College
Chestnut Hill, MA 02167

Eric Fielding
SNEE Hall
INSTOC
Cornell University
Ithaca, NY 14853

Prof. Donald Forsyth
Department of Geological Sciences
Brown University
Providence, RI 02912

Dr. Cliff Frolich
Institute of Geophysics
8701 North Mopac
Austin, TX 78759

Prof. Art Frankel
Mail Stop 922
Geological Survey
790 National Center
Reston, VA 22092

Dr. Anthony Gangi
Texas A&M University
Department of Geophysics
College Station, TX 77843

Dr. Freeman Gilbert
Inst. of Geophysics & Planetary Physics
University of California, San Diego
P.O. Box 109
La Jolla, CA 92037

Mr. Edward Giller
Pacific Sierra Research Corp.
1401 Wilson Boulevard
Arlington, VA 22209

Dr. Jeffrey W. Given
Sierra Geophysics
11255 Kirkland Way
Kirkland, WA 98033

Prof. Stephen Grand
University of Texas at Austin
Department of Geological Sciences
Austin, TX 78713-7909

Prof. Roy Greenfield
Geosciences Department
403 Deike Building
The Pennsylvania State University
University Park, PA 16802

Dan N. Hagedorn
Battelle
Pacific Northwest Laboratories
Battelle Boulevard
Richland, WA 99352

Kevin Hutchenson
Department of Earth Sciences
St. Louis University
3507 Laclede
St. Louis, MO 63103

Prof. Thomas H. Jordan
Department of Earth, Atmospheric
and Planetary Sciences
Massachusetts Institute of Technology
Cambridge, MA 02139

Robert C. Kemerait
ENSCO, Inc.
445 Pineda Court
Melbourne, FL 32940

William Kikendall
Teledyne Geotech
3401 Shiloh Road
Garland, TX 75041

Prof. Leon Knopoff
University of California
Institute of Geophysics & Planetary Physics
Los Angeles, CA 90024

Prof. L. Timothy Long
School of Geophysical Sciences
Georgia Institute of Technology
Atlanta, GA 30332

Prof. Art McGarr
Mail Stop 977
Geological Survey
345 Middlefield Rd.
Menlo Park, CA 94025

Dr. George Mellman
Sierra Geophysics
11255 Kirkland Way
Kirkland, WA 98033

Prof. John Nabelek
College of Oceanography
Oregon State University
Corvallis, OR 97331

Prof. Geza Nagy
University of California, San Diego
Department of Ames, M.S. B-010
La Jolla, CA 92093

Prof. Amos Nur
Department of Geophysics
Stanford University
Stanford, CA 94305

Prof. Jack Oliver
Department of Geology
Cornell University
Ithaca, NY 14850

Prof. Robert Phinney
Geological & Geophysical Sciences
Princeton University
Princeton, NJ 08544-0636

Dr. Paul Pomeroy
Rondout Associates
P.O. Box 224
Stone Ridge, NY 12484

Dr. Jay Pulli
RADIX System, Inc.
2 Taft Court, Suite 203
Rockville, MD 20850

Dr. Norton Rimer
S-CUBED
A Division of Maxwell Laboratory
P.O. Box 1620
La Jolla, CA 92038-1620

Prof. Larry J. Ruff
Department of Geological Sciences
1006 C.C. Little Building
University of Michigan
Ann Arbor, MI 48109-1063

Dr. Richard Sailor
TASC Inc.
55 Walkers Brook Drive
Reading, MA 01867

Thomas J. Sereno, Jr.
Science Application Int'l Corp.
10210 Campus Point Drive
San Diego, CA 92121

John Sherwin
Teledyne Geotech
3401 Shiloh Road
Garland, TX 75041

Prof. Robert Smith
Department of Geophysics
University of Utah
1400 East 2nd South
Salt Lake City, UT 84112

Prof. S. W. Smith
Geophysics Program
University of Washington
Seattle, WA 98195

Dr. Stewart Smith
IRIS Inc.
1616 North Fort Myer Drive
Suite 1440
Arlington, VA 22209

Dr. George Sutton
Rondout Associates
P.O. Box 224
Stone Ridge, NY 12484

Prof. L. Sykes
Lamont-Doherty Geological Observatory
of Columbia University
Palisades, NY 10964

Prof. Pradeep Talwani
Department of Geological Sciences
University of South Carolina
Columbia, SC 29208

Prof. Ta-liang Teng
Center for Earth Sciences
University of Southern California
University Park
Los Angeles, CA 90089-0741

Dr. R.B. Tittmann
Rockwell International Science Center
1049 Camino Dos Rios
P.O. Box 1085
Thousand Oaks, CA 91360

Dr. Gregory van der Vink
IRIS, Inc.
1616 North Fort Myer Drive
Suite 1440
Arlington, VA 22209

Professor Daniel Walker
University of Hawaii
Institute of Geophysics
Honolulu, HI 96822

William R. Walter
Seismological Laboratory
University of Nevada
Reno, NV 89557

Dr. Gregory Wojcik
Weidlinger Associates
4410 El Camino Real
Suite 110
Los Altos, CA 94022

Prof. John H. Woodhouse
Hoffman Laboratory
Harvard University
20 Oxford St.
Cambridge, MA 02138

Dr. Gregory B. Young
ENSCO, Inc.
5400 Port Royal Road
Springfield, VA 22151-2388

GOVERNMENT

Dr. Ralph Alewine III
DARPA/NMRO
1400 Wilson Boulevard
Arlington, VA 22209-2308

Mr. James C. Battis
GL/LWH
Hanscom AFB, MA 01731-5000

Dr. Robert Blandford
DARPA/NMRO
1400 Wilson Boulevard
Arlington, VA 22209-2308

Eric Chael
Division 9241
Sandia Laboratory
Albuquerque, NM 87185

Dr. John J. Cipar
GL/LWH
Hanscom AFB, MA 01731-5000

Mr. Jeff Duncan
Office of Congressman Markey
2133 Rayburn House Bldg.
Washington, DC 20515

Dr. Jack Evernden
USGS - Earthquake Studies
345 Middlefield Road
Menlo Park, CA 94025

Art Frankel
USGS
922 National Center
Reston, VA 22092

Dr. T. Hanks
USGS
Nat'l Earthquake Research Center
345 Middlefield Road
Menlo Park, CA 94025

Dr. James Hannon
Lawrence Livermore Nat'l Laboratory
P.O. Box 808
Livermore, CA 94550

Paul Johnson
ESS-4, Mail Stop J979
Los Alamos National Laboratory
Los Alamos, NM 87545

Janet Johnston
GL/LWH
Hanscom AFB, MA 01731-5000

Dr. Katharine Kadinsky-Cade
GL/LWH
Hanscom AFB, MA 01731-5000

Ms. Ann Kerr
IGPP, A-025
Scripps Institute of Oceanography
University of California, San Diego
La Jolla, CA 92093

Dr. Max Koontz
US Dept of Energy/DP 5
Forrestal Building
1000 Independence Avenue
Washington, DC 20585

Dr. W.H.K. Lee
Office of Earthquakes, Volcanoes,
& Engineering
345 Middlefield Road
Menlo Park, CA 94025

Dr. William Leith
U.S. Geological Survey
Mail Stop 928
Reston, VA 22092

Dr. Richard Lewis
Director, Earthquake Engineering & Geophysics
U.S. Army Corps of Engineers
Box 631
Vicksburg, MS 39180

James F. Lewkowicz
GL/LWH
Hanscom AFB, MA 01731-5000

Mr. Alfred Lieberman
ACDA/VI-OA State Department Bldg
Room 5726
320 - 21st Street, NW
Washington, DC 20451

Stephen Mangino
GL/LWH
Hanscom AFB, MA 01731-5000

Dr. Frank F. Pilotte
HQ AFTAC/TT
Patrick AFB, FL 32925-6001

Dr. Robert Masse
Box 25046, Mail Stop 967
Denver Federal Center
Denver, CO 80225

Katie Poley
CIA-OSWR/NED
Washington, DC 20505

Art McGarr
U.S. Geological Survey, MS-977
345 Middlefield Road
Menlo Park, CA 94025

Mr. Jack Rachlin
U.S. Geological Survey
Geology, Rm 3 C136
Mail Stop 928 National Center
Reston, VA 22092

Richard Morrow
ACDA/VI, Room 5741
320 21st Street N.W.
Washington, DC 20451

Dr. Robert Reinke
WL/NTESG
Kirtland AFB, NM 87117-6008

Dr. Keith K. Nakanishi
Lawrence Livermore National Laboratory
P.O. Box 808, L-205
Livermore, CA 94550

Dr. Byron Ristvet
HQ DNA, Nevada Operations Office
Attn: NVCG
P.O. Box 98539
Las Vegas, NV 89193

Dr. Carl Newton
Los Alamos National Laboratory
P.O. Box 1663
Mail Stop C335, Group ESS-3
Los Alamos, NM 87545

Dr. George Rothe
HQ AFTAC/TGR
Patrick AFB, FL 32925-6001

Dr. Kenneth H. Olsen
Los Alamos Scientific Laboratory
P.O. Box 1663
Mail Stop C335, Group ESS-3
Los Alamos, NM 87545

Dr. Alan S. Ryall, Jr.
DARPA/NMRO
1400 Wilson Boulevard
Arlington, VA 22209-2308

Howard J. Patton
Lawrence Livermore National Laboratory
P.O. Box 808, L-205
Livermore, CA 94550

Dr. Michael Shore
Defense Nuclear Agency/SPSS
6801 Telegraph Road
Alexandria, VA 22310

Mr. Chris Paine
Office of Senator Kennedy
SR 315
United States Senate
Washington, DC 20510

Donald L. Springer
Lawrence Livermore National Laboratory
P.O. Box 808, L-205
Livermore, CA 94550

Colonel Jerry J. Perrizo
AFOSR/NP, Building 410
Bolling AFB
Washington, DC 20332-6448

Mr. Charles L. Taylor
GL/LWG
Hanscom AFB, MA 01731-5000

Dr. Thomas Weaver
Los Alamos National Laboratory
P.O. Box 1663, Mail Stop C335
Los Alamos, NM 87545

DARPA/PM
1400 Wilson Boulevard
Arlington, VA 22209

J.J. Zucca
Lawrence Livermore National Laboratory
Box 808
Livermore, CA 94550

Defense Technical Information Center
Cameron Station
Alexandria, VA 22314 (5 copies)

GL/SULL
Research Library
Hanscom AFB, MA 01731-5000 (2 copies)

Defense Intelligence Agency
Directorate for Scientific &
Technical Intelligence
Washington, DC 20301

Secretary of the Air Force
(SAFRD)

AFTAC/CA
(STINFO)
Patrick AFB, FL 32925-6001

Washington, DC 20330

Office of the Secretary Defense
DDR & E
Washington, DC 20330

TACTEC
Battelle Memorial Institute
505 King Avenue
Columbus, OH 43201 (Final Report Only)

HQ DNA
Attn: Technical Library
Washington, DC 20305

DARPA/RMO/RETRIEVAL
1400 Wilson Boulevard
Arlington, VA 22209

DARPA/RMO/Security Office
1400 Wilson Boulevard
Arlington, VA 22209

Geophysics Laboratory
Attn: XO
Hanscom AFB, MA 01731-5000

Geophysics Laboratory
Attn: LW
Hanscom AFB, MA 01731-5000

CONTRACTORS (Foreign)

Dr. Ramon Cabre, S.J.
Observatorio San Calixto
Casilla 5939
La Paz, Bolivia

Prof. Hans-Peter Harjes
Institute for Geophysik
Ruhr University/Bochum
P.O. Box 102148
4630 Bochum 1, FRG

Prof. Eystein Husebye
NTNF/NORSAR
P.O. Box 51
N-2007 Kjeller, NORWAY

Prof. Brian L.N. Kennett
Research School of Earth Sciences
Institute of Advanced Studies
G.P.O. Box 4
Canberra 2601, AUSTRALIA

Dr. Bernard Massinon
Societe Radiomana
27 rue Claude Bernard
75005 Paris, FRANCE (2 Copies)

Dr. Pierre Mecheler
Societe Radiomana
27 rue Claude Bernard
75005 Paris, FRANCE

Dr. Svein Mykkeltveit
NTNF/NORSAR
P.O. Box 51
N-2007 Kjeller, NORWAY

FOREIGN (Others)

Dr. Peter Basham
Earth Physics Branch
Geological Survey of Canada
1 Observatory Crescent
Ottawa, Ontario, CANADA K1A 0Y3

Dr. Eduard Berg
Institute of Geophysics
University of Hawaii
Honolulu, HI 96822

Dr. Michel Bouchon
I.R.I.G.M.-B.P. 68
38402 St. Martin D'Herès
Cedex, FRANCE

Dr. Hilmar Bungum
NTNF/NORSAR
P.O. Box 51
N-2007 Kjeller, NORWAY

Dr. Michel Campillo
Observatoire de Grenoble
I.R.I.G.M.-B.P. 53
38041 Grenoble, FRANCE

Dr. Kin Yip Chun
Geophysics Division
Physics Department
University of Toronto
Ontario, CANADA M5S 1A7

Dr. Alan Douglas
Ministry of Defense
Blacknest, Brimpton
Reading RG7-4RS, UNITED KINGDOM

Dr. Roger Hansen
NTNF/NORSAR
P.O. Box 51
N-2007 Kjeller, NORWAY

Dr. Manfred Henger
Federal Institute for Geosciences & Nat'l Res.
Postfach 510153
D-3000 Hanover 51, FRG

Ms. Eva Johannisson
Senior Research Officer
National Defense Research Inst
P.O. Box 27322
S-102 54 Stockholm, SWEDEN

Dr. Fekadu Kebede
Seismological Section
Box 12019
S-750 Uppsala, SWEDEN

Dr. Tormod Kvaerna
NTNF/NORSAR
P.O. Box 51
N-2007 Kjeller, NORWAY

Dr. Peter Marshal
Procurement Executive
Ministry of Defense
Blacknest, Brimpton
Reading FG7-4RS, UNITED KINGDOM

Prof. Ari Ben-Menahem
Department of Applied Mathematics
Weizman Institute of Science
Rehovot, ISRAEL 951729

Dr. Robert North
Geophysics Division
Geological Survey of Canada
1 Observatory Crescent
Ottawa, Ontario, CANADA K1A 0Y3

Dr. Frode Ringdal
NTNF/NORSAR
P.O. Box 51
N-2007 Kjeller, NORWAY

Dr. Jorg Schlittenhardt
Federal Institute for Geosciences & Nat'l Res.
Postfach 510153
D-3000 Hannover 51, FEDERAL REPUBLIC OF
GERMANY